Full Scale Experimental Transonic Fan Interaction with a Boundary Layer Ingesting Total Pressure Distortion

Justin Mark Bailey

Dissertation submitted to the faculty of the
Virginia Polytechnic Institute and State University
in partial fulfillment of the requirements for the degree of

Doctor of Philosophy

In

Mechanical Engineering

Walter F. O'Brien, Chair
Clinton L. Dancey
Wing F. Ng
Kevin T. Lowe
Alfred L. Wicks

November 7, 2016
Blacksburg, Virginia

Keywords: Experimental Engine Testing, Distortion, Interaction, Total Pressure, Boundary Layer Ingesting

Full Scale Transonic Fan Interaction with a Boundary Layer Ingesting Total Pressure Distortion

Justin Mark Bailey

ABSTRACT

Future commercial transport aircraft will present more aerodynamic architectures to accommodate stringent design goals for higher fuel efficiency, reduced cruise and taxi NOx emissions, and reduced noise. Airframe designs most likely to satisfy the first goal feature architectures that lead to the formation of non-uniform flow introduced to the engine through boundary layer ingesting (BLI) inlets, creating a different operational environment from which the engines were originally designed. The goal of this study was to explore the effects such non-uniform flow would have on the behavior and performance of a transonic fan in a full scale engine test environment.

This dissertation presents an experimental study of the interaction between a full scale transonic fan and a total pressure distortion representative of a boundary layer ingesting serpentine inlet. A five-hole pneumatic probe was traversed directly in front of and behind a fan rotor to fully characterize the inlet and outlet fan profile. The distortion profile was also measured at the aerodynamic interface plane (AIP) with an SAE standard total pressure rake, which has historically been accepted as the inlet profile to the fan. This provided a comparison between the present work and current practice.

Accurate calculation of local fan performance metrics such as blade loading, pressure rise, and efficiency were obtained. The fan inlet measurement profile greatly enhanced the understanding of the fan interaction to the flow distortion and provided a more complete explanation of the fan behavior. Secondary flowfield formation due to the accelerated flow redistribution directly upstream of the fan created localized bulk co- and counter- rotating swirl regions that were found to be correlated with localized fan performance phenomena. It was observed that the effects of the distortion on fan performance were exaggerated if the assumed fan inlet profiles were data taken only at the AIP.

The reduction in fan performance with respect to undistorted inlet conditions is also explored, providing insight into how such distortions can be compared to baseline conditions. The dissertation closes with several recommendations for improving distortion tolerant fan design in the context of experimental research and development.

Full Scale Transonic Fan Interaction with a Boundary Layer Ingesting Total Pressure Distortion

Justin Mark Bailey

GENERAL AUDIENCE ABSTRACT

Future commercial transport aircraft will present more aerodynamic architectures to accommodate stringent design goals for higher fuel efficiency, reduced cruise and taxi NOx emissions, and reduced noise. Airframe designs most likely to satisfy the first goal feature architectures that lead to the formation of non-uniform flow introduced to the engine through boundary layer ingesting (BLI) inlets, creating a different operational environment from which the engines were originally designed. The goal of this study was to explore the effects such non-uniform flow would have on the behavior and performance of a transonic fan in a full scale engine test environment.

This dissertation presents an experimental study of the interaction between a full scale transonic fan and a total pressure distortion representative of a boundary layer ingesting serpentine inlet. A five-hole pneumatic probe was traversed directly in front of and behind a fan rotor to fully characterize the inlet and outlet fan profile. The distortion profile was also measured at the aerodynamic interface plane (AIP), which has historically been accepted as the inlet profile to the fan. This provided a comparison between the present work and current practice.

Accurate calculation of local fan performance metrics were obtained. The fan inlet measurement profile greatly enhanced the understanding of the fan interaction to the flow distortion and provided a more complete explanation of the fan behavior. It was observed that the effects of the distortion on fan performance were exaggerated if the assumed fan inlet profiles were data taken only at the AIP.

The reduction in fan performance with respect to undistorted inlet conditions is also explored, providing insight into how such distortions can be compared to baseline conditions. The dissertation closes with several recommendations for improving distortion tolerant fan design in the context of experimental research and development.

Acknowledgements

This body of work was completed over a 3-year span, but the design and construction of the research rig began 2 years before then and involved the work of many smart, generous, and dedicated individuals. I would like to acknowledge their contributions here.

Professor Walter O'Brien: Thank you for giving me the opportunity to contribute to the incredible research environment you have at the TurboLab. I count myself fortunate that I was able to do exactly what I wanted for my graduate work – get my hands dirty working with real jet engines. I may not get any recognition from the University for accumulating over 200 engine operating hours, but I should. I enjoyed working with you over the years and would enjoy doing so again.

My committee – Professor Todd Lowe, Professor Wing Ng, Professor Clinton Dancey, and Professor Alfred Wicks: Thank you for your support over the course of my research. Your insights and recommendations for improving this dissertation have been greatly appreciated and I included them in the document as best I could. Your assistance has helped me create a more well-rounded body of work that I could not have completed otherwise.

Dr. Tony Ferrar: We were never given an instruction manual on how to build a distortion tolerant fan research rig but you and I did alright figuring it out ourselves. Thank you for your dedication, focus, and commitment to quality that created a new standard for experimental research at the TurboLab. I would not have been able to complete my research without your efforts in overcoming the difficulties of starting this research. I enjoyed my time working with you over the years and I hope you carry a sense of pride knowing the legacy you pioneered at the TurboLab, and the foundation you created that every generation afterwards benefits from.

Dr. Bill Schneck: Your contributions to my research are incalculable. You were with Tony and I from day one, always willing to help in the extensive debugging procedures associated with an experiment of his magnitude: instrumentation, motion control, hardware, software, etc. Even if you weren't already in the thick of it with us, you were only a phone call away. Thank you for your efforts and suggestions over the years that helped make this research possible. I would not have collected a single data point without you.

Chris Collins: Thank you for your efforts involving the construction of my research rig. You and I worked together on building the majority of the rotator and tunnel sections, sequestered in the lab day after day. Thank you for stepping in as our lab technician when we were in need of one. We made some great parts despite our inexperience, and those parts survived hundreds of engine hours between Tony and myself. I am proud of the work we accomplished and I hope you are as well.

Gregg Perley: Your expertise and innovative solutions have been instrumental in improving my experiment when I took over as the lead researcher on distortion tolerant fan design. I enjoyed our technical discussions over the years, but more so the off topic debates on life, film, and literature. Thank you so much for your input and contributions in helping me complete my research. Working at the lab was more fun with you around and I want to thank you for being an awesome person.

Dustin Frohnapfel: Thank your hard work and assistance over the years in helping me complete my research. It takes at least two people to see our work come to fruition and you were with me anytime I needed. Thank you for your help in: experimental design, component assembly, probe calibration, instrumentation install, alignment, data processing, engine runs, and everything else associated with our respective works. There are so many facets to consider when making quality measurements in the environment we work in but we tackled each one of them together and finished with one of the most unique and capable research facilities in the world.

Katey Smith: I don't think you can understand the contribution you made to my research unless you were there with Tony and I, forced to move our probe by hand. It was a nightmare and took weeks to get all the data we needed. Your improvements to the probe motion control allowed me to expand my test matrix and complete far more tests than would have been possible otherwise. Your work on the probe calibration rig also allowed Dustin and I to calibrate the probe quickly and accurately. I would probably still be collecting data without your contribution. Thank you.

Diana Israel: You're the best program support technician ever! Thank you for working with me for six years and making sure I had everything I needed to complete my research. I wouldn't have had any toys to play with if you had not purchased them for me. I enjoyed our talks getting to know you during my time at VT.

Everyone else who contributed to my research in some way: Dr. William Copenhaver, Dr. William Cousins, Todd Pickering, Steven Steele, Kevin Hoopes, James Lucas, Bill Hook, Bill Bradley, Bill Bryant, Joe Hall, Ali Alhamaly, Ahmed Aly, Jesse Dollberg, Dr. Chaitanya Halbe. Thank you for your contributions and collaborations.

My Mother and Father: Thank you for providing me with the foundation I needed to accomplish this work. You were only a phone call or short drive away and I always had your love and support to fall back on if I needed. None of this would have been possible without your guidance. I love both of you will all my heart.

My Sisters: Thank you for your support over my longer than expected stay in Virginia. I love you and hope my work instills you with confidence, to know that you can accomplish what you thought impossible if you're willing to work for it.

Table of Contents

List of Tables

Table Page

List of Figures

Figure Page

Nomenclature

Symbol/Acronym	Description	Units
a	Speed of sound	m/s
A	Cross sectional area	in^2
α	Absolute flow angle, Probe relative radial angle	deg (°)
AIP	Aerodynamic Interface Plane	
AWOS	Automated Weather Observing System	
β	Blade relative flow angle Probe relative tangential angle	deg (°)
BDC	Bottom Dead Center	
BPF	Blade Passing Frequency	Hz
c	Blade chord	in
C	Absolute velocity	m/s
CFS	Corrected Fan Speed	%
CMF	Corrected Mass flow Rate	lbs/s
CP	Pressure Coefficient	
Ø	Diameter	
EO	Engine Order	
FAA	Federal Aviation Administration	
FI	Fan Inlet	
FO	Fan Outlet	
h_{alt}	Altitude	m
LDF	Lieblein Diffusion Factor	
M	Mach Number	
M_{air}	Molecular Weight of air	g/mol
$\dot{m}$	Mass flow rate	lbs/sec
μ	Dynamic viscosity	kg/(m·s)
NIST	National Institute of Standards and Technology	
NWS	National Weather Service	
Ω	Rotational velocity	rad/s
P_{stn}	Local station pressure at altitude	in-Hg
P_{sl}	Sea level pressure	in-Hg
P_T	Total pressure	psi
P_S	Static pressure	psi
Ψ, ψ	Parameter	
R	Specific gas constant for air	J/(kg·K)
RDFA	Relative Difference From Average	%
RDFT	Relative Difference From Target	%
RDFU	Relative Difference From Undistorted	%

RMS	Root Mean Square	%
RMSD	Root Mean Square Difference	%
s	Blade spacing	in
TDC	Top Dead Center	
θ	Tangential flow direction Circumferential Position	deg (°)
U	Blade speed	m/s
W	Relative velocity	m/s
x	x-coordinate direction	in
y	y-coordinate direction	in
z	Axial flow direction	in

Chapter 1 Introduction

In order to meet stringent requirements for next generation commercial aviation, aircraft will need to employ more aerodynamic designs to 1) reduce noise, 2) improve landing, takeoff, and cruise emissions, and 3) improve fuel consumption [1,2]. These designs are expected to take the aviation industry away from traditional 'tube-and-wing' architectures into a more hybrid or blended wing body (HWB, BWB) design that will satisfy aircraft operation improvement goals. A comparison between modern and proposed airframe architectures is shown in Figure 1.1.

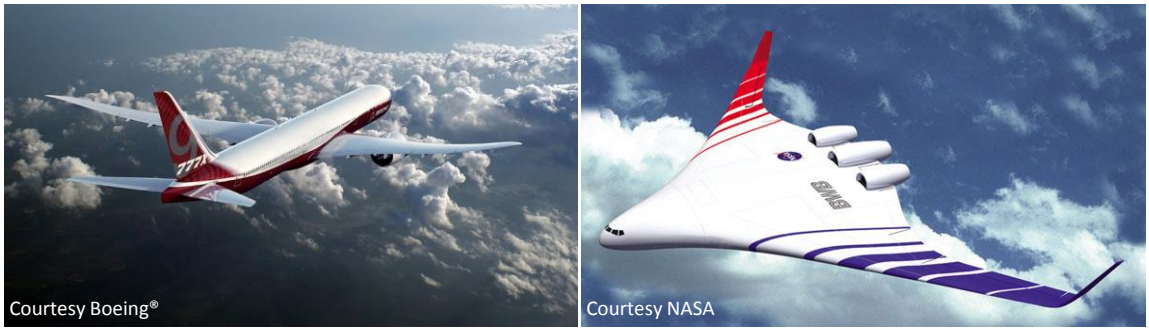

Figure 1.1. Modern aircraft 'tube-and-wing' design (Left) and future blended wing design (Right).

A common feature of these HWB airframes is the integration of the engines with the aircraft fuselage. This relocation changes the inlet flow environment as the engines are no longer mounted below the wings where uniform inlet flow is ingested for the majority of the flight envelope. Mounting the engines in close proximity to the airframe, or embedding them within the airframe, results in non-uniform (distorted) inlet flow caused by the airframe body or inlet ducts. In the interest of performance and efficiency, modern commercial transport engines are designed to tolerate only small levels of distortion, such as during takeoff or strong crosswind conditions. Integrated propulsion systems will experience distorted inflow over the entire flight envelope and their interaction with such conditions will need to be studied to determine how engine performance is affected, and to support the design of distortion-tolerant engines.

To determine how well engines can withstand such an environment, three criteria will need to be evaluated in great detail; aeromechanics, stability, and performance. Although studies have shown that engine operation penalties are found in each one of these, the overall benefit of highly integrated airframe and propulsion systems can justify the operational challenges introduced to the engines [4].

1.1 Literature Review

Studies have been performed on the evaluation of engines subject to non-uniform inlet flows produced by highly integrated engine-airframe systems. The three metrics that must be most considered are; aeromechanics, stability, and performance. Researchers can find background into aeromechanical fatigue caused by distorted inflow through earlier publications [5, 6]. As this work focuses on the impact of stability and performance, the literature review will investigate previous work on these subjects in detail. An important component of the integrated engine-airframe problem is the issue of fan-distortion interaction, in which a coupling effect between the distortion or distortion producing device and the fan exists. As will be shown later, these components act together as a single system that must be considered when designing distortion-producing devices within the context of distortion tolerant fan research.

1.1.1 Stability

Stability is a qualitative measure of how well an engine can handle off-design conditions. It is measured quantitatively via surge margin which represents how much the compressor is allowed to be aerodynamically loaded in off-design conditions before compression breakdown and flow reversal (surging). Higher surge margin represents greater stability at lower performance while lower surge margin allows for higher performance at the cost of reduced stability. An example of how distorted inflow affects stability is shown in Figure 1.2. The reduction in performance for equivalent engine speeds is accompanied by a reduced operation range for off-design conditions. Further background can be found in previous publications [8-12].

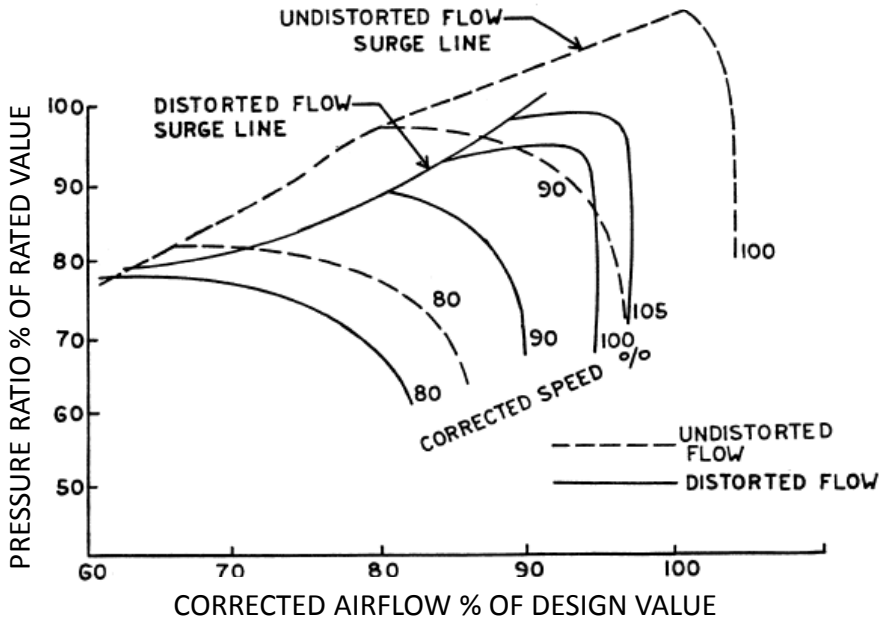

Figure 1.2. Example of distortion impact on compressor surge margin [7].

1.1.2 Performance

At constant speed a compressor will produce a greater pressure rise in lower mass flow regions but only so long as the flow over the blades remains attached [3]. Once the aerodynamic loading on the blade is too great, premature separation will occur and can lead to stall and eventually surge. Fans are typically designed to input constant work to the inlet flow to obtain uniform outlet conditions, maximizing thrust. Distorted inflow creates regions of high and low blade loading resulting in non-uniform work input to the flow and non-uniform outlet flow that reduces efficiency and thrust output. Thus, to achieve the same required thrust as uniform inlet flow the fan must input more work to the flow [3,13]. This forces the fan to operate at a higher speed and reduced efficiency, requiring more fuel. Although the overall aircraft system will be more aerodynamic and require less engine thrust, the non-uniform fan outlet conditions must be studied to optimize flow conditions and maximize fan operating efficiency and performance while minimizing fuel consumption.

1.1.3 Fan-Distortion Interaction

Since the fan is moving its operating point along a constant speed line when subjected to distortion, the pressure rise varies for the flowfield. In the case of total pressure distortion profiles there exist areas of high and low total pressure. The regions of low total pressure contain lower mass flow and move the local operating point of the fan to a higher pressure rise. This resultant higher pressure rise reduces the static pressure in that region upstream of the fan and drives a mass flow redistribution from the AIP to the fan face. Regions of higher mass flow will migrate towards regions of lower mass flow and trend toward uniformity [14, 17].

The mass flow redistribution results in secondary flow development of considerable magnitude [15, 16]. These secondary flow characteristics interact with the fan in a different manner than just the reduced mass flow, resulting in a more complex inlet profile. This redistribution is found to be dependent on the slope of the compressor characteristic [18]. The secondary flowfield can be separated into radial and tangential components, where the tangential flow strongly affects the blade turning, blade loading, and efficiency of the fan. Although the total pressure distortion will not vary significantly between the distortion measurement plane and the fan face, the static pressure distortion will increase exponentially. The distortions in static and total pressure, as well as the radial and tangential flow angles, have been found to be attenuated through the fan [16,19].

1.1.4 Summary

Distortion tolerant fan design has been an ongoing area of research since the introduction of jet propulsion. As the complexity of propulsion systems increase to meet the demands of improved fuel economy, durability, operation range, and performance, the accuracy and research capability must also improve to better design and validate

components in experimental settings. Readers can find further information on distortion tolerant research and its evolution through previous publications [4, 13, 20].

1.2 Research Objectives

The previous research discussed has provided engine designers with valuable expertise in developing more distortion-tolerant fans. However, many of the studies limit the complexity of the profiles to simple geometries. While this is fundamental in developing an understanding of fan response to non-uniform inlet flow, BWB and HWB airframes produce specific distortion patterns that are more complicated and research is required to understand how these specific profiles affect fan performance.

The work presented here studies a total pressure distortion profile representative of a boundary layer ingesting serpentine inlet. The inlet of interest that produces a combined total pressure and flow angularity distortion, but the components must be studied separately to determine their contribution to the overall fan operation. What is unique about this work is the usage of a full size turbofan engine operating at 60%, 70%, and 80% design speed, where 80% corresponds to transonic tip velocities. Both fan inlet and fan outlet flowfields were measured using a calibrated five-hole pressure probe within 0.5 blade chords of the fan leading and trailing edges to obtain all the flow parameters necessary to characterize fan performance.

This work will study the fan interaction to this distortion profile in detail and will provide researchers and engine designers with a greater understanding of fan operation in the presence of total pressure distortion. In addition, the advanced measurement capabilities and techniques developed in this study can aid experimental researchers in obtaining accurate and relevant results. Finally, testing on a full scale engine also provides insight into how the fan responds to distortion on a system level, as isolated electric driven fan designs lack the low pressure turbine operation matching that exists in full-scale engine experiments.

The overall goal in making next generation aircraft architecture flight worthy is to design engines that are capable of handling the constant distortion produced by BWB and HWB airframes. This can be done via two ways; 1) increasing the operability of the engines to such an extent that the distortion can be tolerated but at the cost of severely reduced performance and efficiency, or 2) creating tailor-designed engines that are built to operate at maximum efficiency and performance at the distorted cruise conditions with a large enough margin to tolerate off-design conditions. The final product will likely be a compromise of the two.

Chapter 2 Experimental Methodology

Obtaining accurate measurements on a full scale turbofan engine requires many custom, tailor-fit components to be designed, built, calibrated, and installed. A basic overview of the equipment and measurement protocol utilized will be discussed here. Interested readers are referred to related work that examines these components in further detail [20].

2.1 Experimental Investigation

Full-scale experimental total pressure distortion ground tests were conducted on a modified Pratt & Whitney Canada JT15D-1 turbofan engine at the Virginia Tech Turbomachinery and Propulsion Laboratory in Blacksburg, Virginia. A schematic of the experimental setup is shown in Figure 2.1.

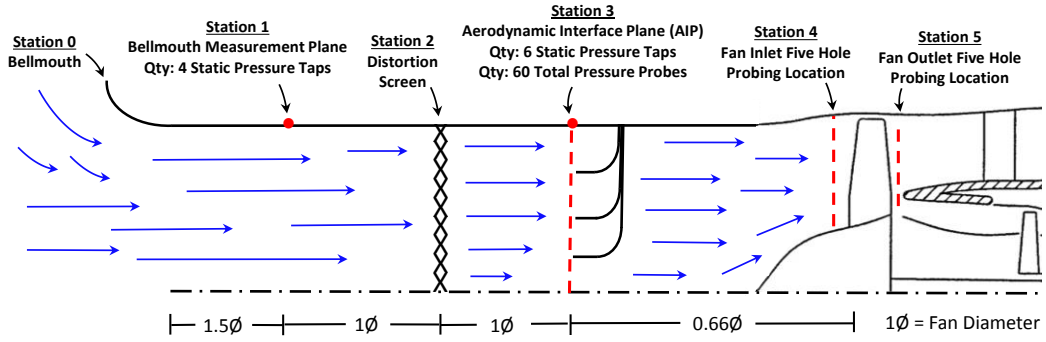

Figure 2.1. Schematic of experimental components and configuration.

The areas of interest are divided into six stations:

Station 0 - Calibrated bellmouth inlet that funnels airflow from outside the test cell and into the experimental rig.

Station 1 - Bellmouth measurement plane with four static pressure taps equally spaced circumferentially around the tunnel.

Station 2 - Distortion screen that produces a total pressure distortion representative of a boundary layer ingesting (BLI) serpentine inlet.

Station 3 - AIP rake case with 60 local total pressure probes and six equally spaced circumferential wall static pressure taps.

Station 4 - Fan inlet measurement plane located approximately 1 inch upstream of the fan leading edge (~40% chord).

Station 5 - Fan outlet measurement plane located approximately 0.375” downstream of the fan trailing edge (~23% chord).

2.1.1 Experiment Stations

Each of the stations identified in Figure 2.1 will be discussed in further detail in the following subsections. For further specifications on the installation procedures, the reader is referred to [20] and [25].

2.1.1.1 Station 0 and 1

The bellmouth inlet is composed of spun 3003 Aluminum to obtain an ASME standard curve profile. The bellmouth was calibrated at the TurboLab to obtain the bellmouth discharge coefficient as a function of Reynold's number. Utilizing the four static pressures obtained at Station 1 along with the discharge coefficient, the mass flow through the tunnel can be calculated. Station 1 is located approximately 1.5Ø (1.5 fan diameters) downstream of the bellmouth throat [21]. The bellmouth inlet section is comprised of the bellmouth inlet and a 2Ø straight section immediately downstream. Once assembled these sections were never disassembled, thus the calibration curve applies to the assembly and not just the bellmouth. The bellmouth and accompanying downstream sections were treated as a single assembly. A schematic of the bellmouth and accompanying experiment photograph is shown in Figure 2.2

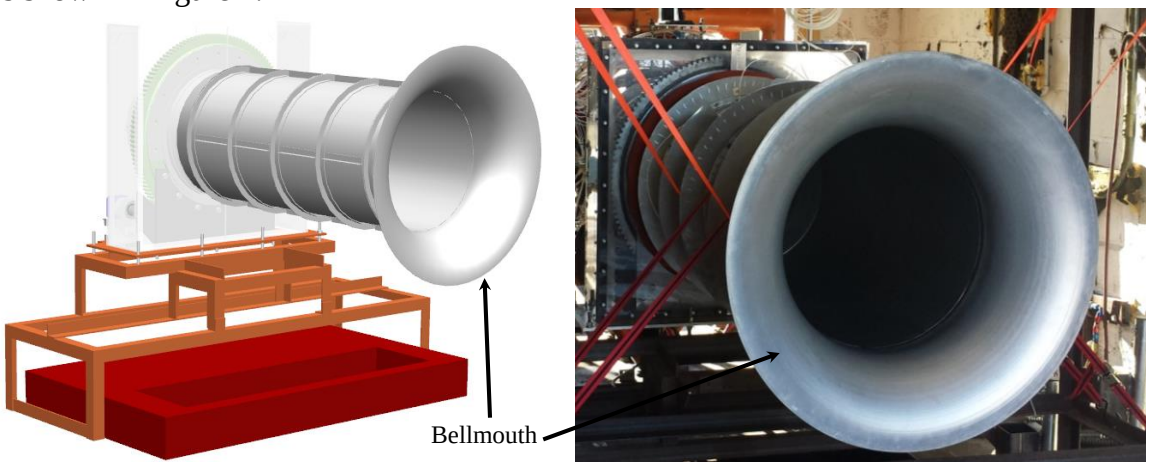

Figure 2.2. Bellmouth schematic (left) and experiment photograph (right).

2.1.1.2 Station 2

The distortion screen used in this experiment was designed to produce a total pressure distortion representative of a boundary layer ingesting (BLI) serpentine inlet. The profile was modeled after the NASA Inlet-A duct, from which the data can be referenced in [33]. The losses for this profile are considered severe in the aerospace committee [23] and provided sufficient non-uniformities to significantly alter fan performance. A schematic and photograph of the distortion screen is shown in Figure 2.3. The distortion screen is located approximately 2.5Ø downstream of the bellmouth throat.

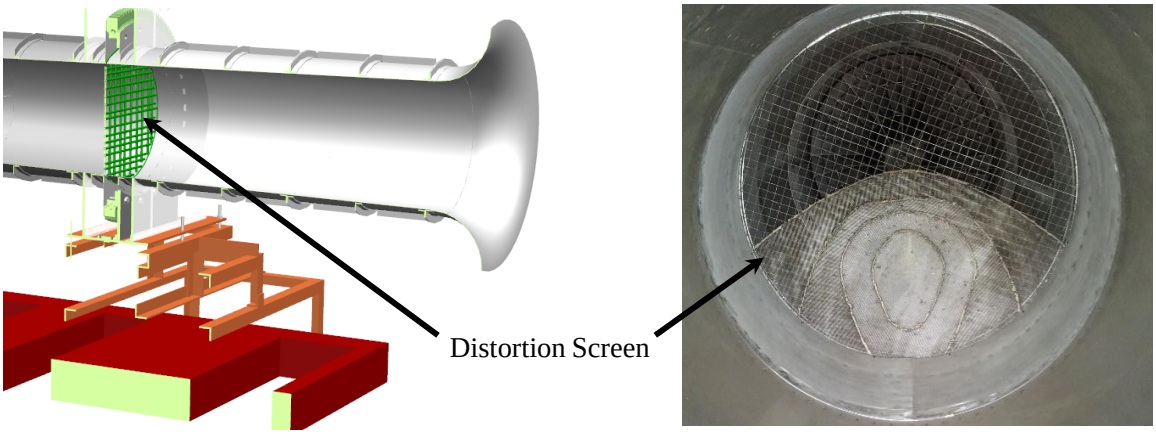

Figure 2.3. Schematic (left) and photograph (right) of the distortion screen used in the experiment.

Figure 2.4 provides the profile shapes for both the distorted and undistorted cases. The distorted profile has a significant total pressure reduction on the bottom half of the profile while the undistorted profile is uniform. The distorted profile under investigation has a high circumferential distortion and a mild radial distortion. The distortion intensity (maximum pressure deficit) for these tests is high and considered an extreme case [33], [23].

The distortion screen is bolted to the back of slew-ring bearing that allows 360-degree rotation such that the flowfield can be mapped with circumferentially stationary instrumentation. Details regarding screen construction and implementation for both distorted and undistorted configurations can be found in previous publications [23].

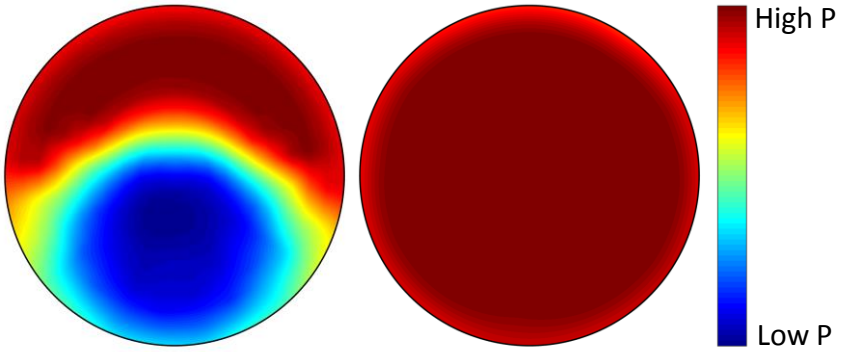

Figure 2.4. Distorted (left) and undistorted (right) total pressure profiles.

2.1.1.3 Station 3

The AIP is classically defined as the interface between the inlet and engine. This measurement station characterizes the distortion profile as established by the Aerospace Recommended Practices albeit with a 50% increase (60 measurements as opposed to 40) in total pressure measurement circumferential density [24]. In addition to the 60 probe total pressure measurements there are six static pressure ports taps equally spaced circumferentially around the inner wall. All measurements are assembled together within

the AIP rake case and represent the AIP measurement plane. Schematics and photographs of the AIP rake are shown in Figure 2.5.

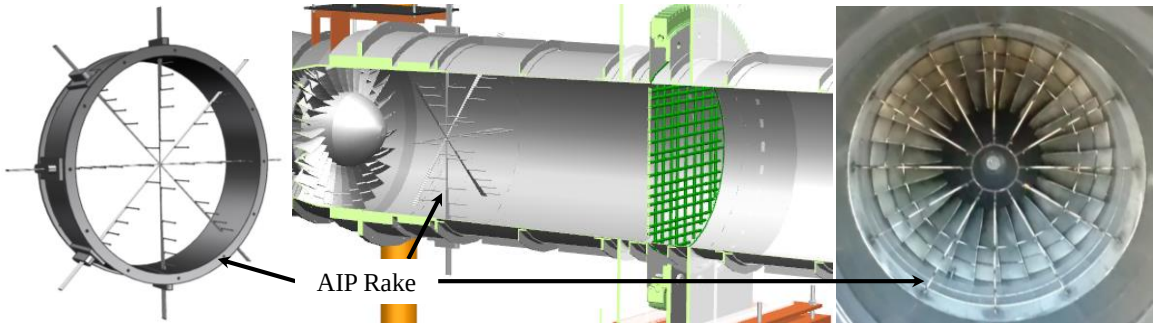

Figure 2.5. Schematics (left and center) and photograph (right) of the AIP rake.

2.1.1.4 Station 4

The fan inlet measurement plane was located approximately 1 inch upstream of the fan leading edge, approximately 0.05Ø and 40% chord. Since the fan blade employs a backward lean and varying span-wise chord length, a uniform measurement plane with respect to the blade was not obtained. The variation in axial measurement location with respect to the fan blade is 0.02Ø and deemed negligible for the purposes of this study.

A pneumatic five-hole probe was radially traversed in this location by means of an electronically controlled traversing probe mount. The fan case insertion point was sealed with a compression fitting that utilized a Teflon ferrule, allowing linear motion while providing a pressure seal and damping. The probe mount was designed to ensure a normal traversing plane with respect to the fan case.

The five-hole probe measures five pressures and one total temperature simultaneously. The five pressure measurements were later post processed to obtain total pressure, static pressure, and flow angularity.

2.1.1.5 Station 5

The fan outlet measurement plane was located approximately 0.375” downstream of the fan trailing edge, approximately 0.02Ø and 23% chord. Again, the variable span-wise measurement distance from the tapered fan blade trailing edge was considered negligible.

The five-hole probe was traversed in this location as was done at Station 4, although constraints between the probe and engine geometry prevented near blade root measurements as the reinforcement tube of the probe interfered with the splitter (fixed engine geometry that ‘splits’ the flow between the bypass and core). The fan bypass was fully traversed and approximately 20% of the core outer flow path was obtained. A custom insertion mount was created for the outlet plane due to the axial-wise variation in fan case geometry (fan case featured a nozzle structure – larger diameter at inlet, smaller diameter at the outlet) and planar traversing was verified during installation.

2.1.1.6 Summary

An overall schematic of the experiment is shown in Figure 2.6. Stations 4 and 5 were accessed via a radial traverse that allowed motion during the experiment such that several

radial locations could be measured at each rotation of the distortion screen. The traverse and its components will be shown in greater detail in succeeding sections.

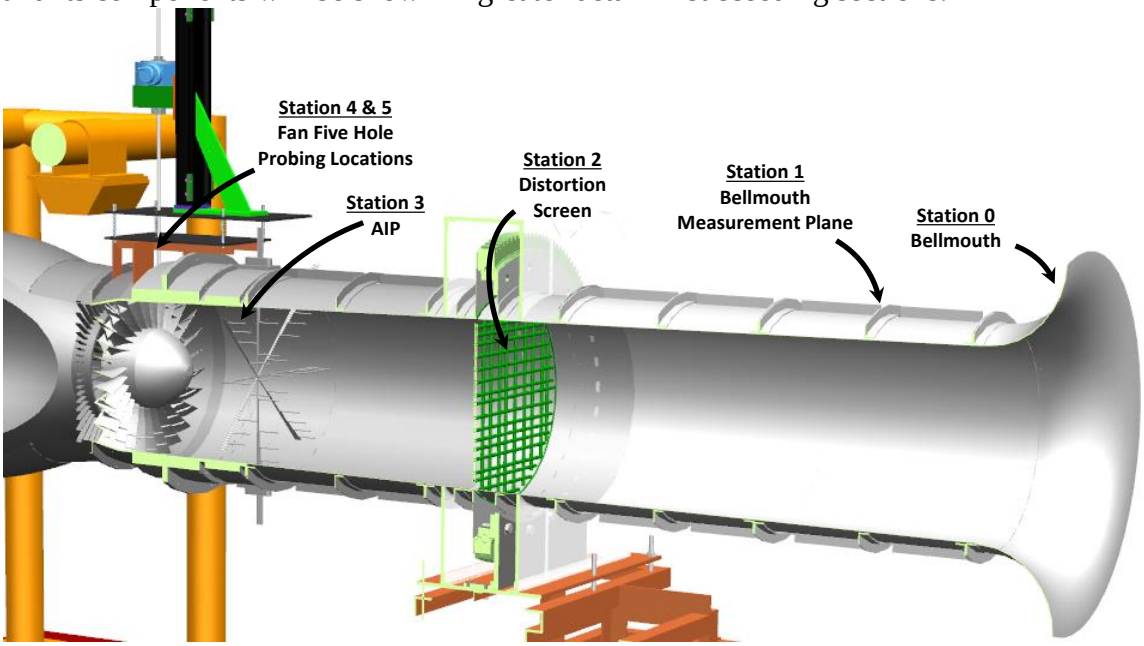

Figure 2.6. Schematic overview of the experiment.

2.1.2 Inlet Conditions

Three separate inlet conditions were investigated for the distorted profile cases: 60, 70, and 80% CFS (Corrected Fan Speed), with transonic tip conditions obtained at 80% CFS. The distortion screen losses followed a second order relationship with fan speed such that losses were relatively more severe at higher fan speeds. These three CFS's corresponded to three CMF's (Corrected Mass Flows) based on the engine operation line for the distorted screen configuration as shown in Figure 2.7. These three CFS's along with their corresponding CMF's were duplicated for the undistorted cases and provided details on how the distorted profiles interact with the fan in comparison to equivalent undistorted CFS and CMF conditions. Notice how higher fan speeds must be reached to obtain equivalent mass flows: at 60% CFS only 3 lbs/s separate the distorted case from the undistorted equivalent mass flow case, while at 80% CFS the discrepancy has grown to 7 lbs/s, a consequence of the increased relative losses through the screen for increasing fan speed.

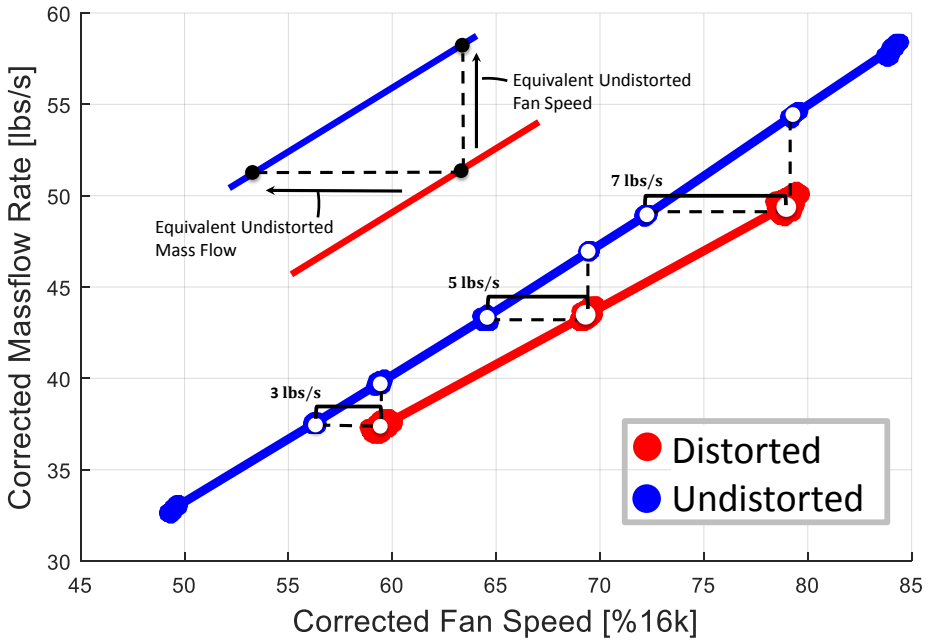

Figure 2.7. Experimental operation line for distorted and undistorted cases.

2.1.3 Atmospheric Conditions

Atmospheric conditions were an important consideration as the duration and complexity of data collection, experiment construction and assembly, and engine run scheduling forced tests to be completed over a span of eight months. This required the data to be normalized by atmospheric conditions at the time of collection such that standard conditions could be calculated and between-test comparisons could be made.

Local atmospheric conditions were obtained from the weather station located at the Virginia Tech Montgomery Executive Airport. The station was located less than one quarter mile from the test cell and contained NIST traceable instrumentation monitored by the FAA. The atmospheric data was recorded every 20 minutes and available online from the NWS (National Weather Service) in the form of lookup tables that were interpolated to the time of collection. The data provided had been corrected to sea level conditions, which was uncorrected during post-processing to obtain the local atmospheric pressure at altitude using Equation (2.1), where P_{atm} is the local atmospheric station pressure at altitude in in-Hg, P_{sl} is the local atmospheric station pressure corrected to sea level in in-Hg, and h_{alt} is the station altitude in meters (649.7).

$$P_{atm} = P_{sl} * \left(\frac{288 - 0.0065 * h_{alt}}{288}\right)^{5.2561} \tag{2.1}$$

Pressure and temperature data was standardized using Equation (2.2) where Y represents a pressure or temperature measurement. Atmospheric pressure (P_{atm}) and temperature (T_{atm}) are the local station conditions at altitude at the time of the data

collection. Standard pressure (P_{std}) and temperature (T_{std}) are 14.696 psi and 59°F, respectively. The resultant parameter, Y_{cor}, represents the corrected pressure or temperature accounting for local atmospheric conditions at the time the measurement was recorded.

$$Y_{cor} = \frac{Y}{Y_{atm}} * Y_{std} \tag{2.2}$$

2.2 Five Hole Probe

The pneumatic five-hole probe utilized was a United Sensor™ DAT design, featuring five pressure ports housed within a prism head architecture with a K-type thermocouple installed below the ports. A schematic of the probe geometry as well as installation photographs is shown in Figure 2.8. A reinforcement tube is brazed to the sensing head to provide structural support.

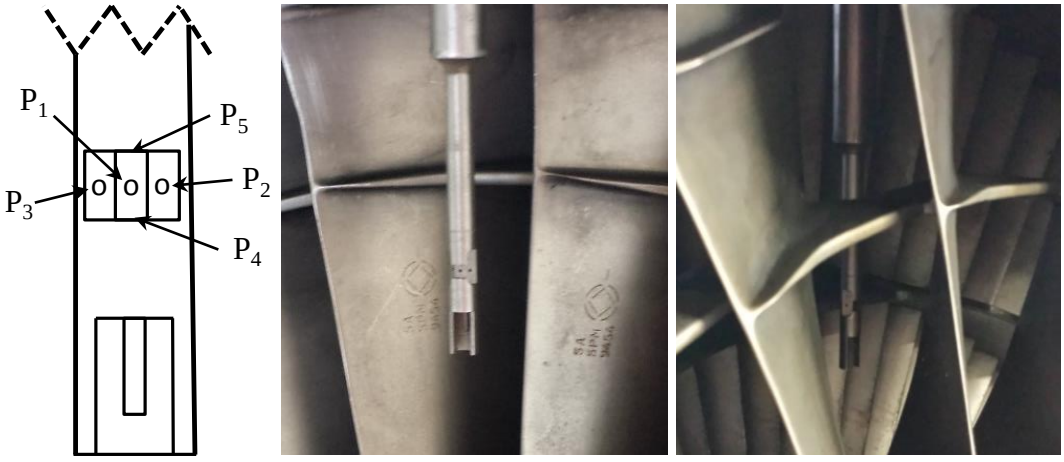

Figure 2.8. Five-hole probe schematic (left), fan inlet (Station 4) installation (center), and fan outlet (Station 5) installation (right).

2.2.1 Design

The probe was constructed of 316 stainless steel, with the overall geometry parametrized to minimize deflection and deformation during engine operation. The resultant analysis, outlined in Appendix C, found that a sensing head diameter of 3/16" and a reinforcement tube diameter of 3/8" to be sufficiently rigid while minimizing the intrusiveness of the measurement. A modal analysis of the geometry following the methods outlined in Appendix C provided the blade passing frequencies to avoid during testing. Appendix C also includes an analysis of the time response of the probe.

2.2.2 Calibration

Calibration of the probe was performed utilizing a custom-built system designed at Virginia Tech specifically for multi-hole probes. Figure 2.9-right shows a schematic of the rig where air from a blowdown compressor is passed over the probe while it is rotated in both pitch and yaw to obtain pressure coefficient maps (Figure 2.9-left) for varying flow parameters. The probe was calibrated on a (-40°) – (+40°) grid in 2.5° increments, with 1° increments within a 10° x 10° window. Three inlet Mach numbers were evaluated (0.4, 0.5, 0.6) with 2-5 replications completed depending on the grid and Mach number tested. It was found that the Mach number had negligible effect on the calibration maps and was not used in the calibration map construction, details of which can be found in Appendix A. All speeds were averaged to obtain the final calibration map. A more detailed analysis of the calibration matrix and final interpolation map used can be found in Appendix A. Further details on the setup and completion of the calibration can be found in previous publications [25].

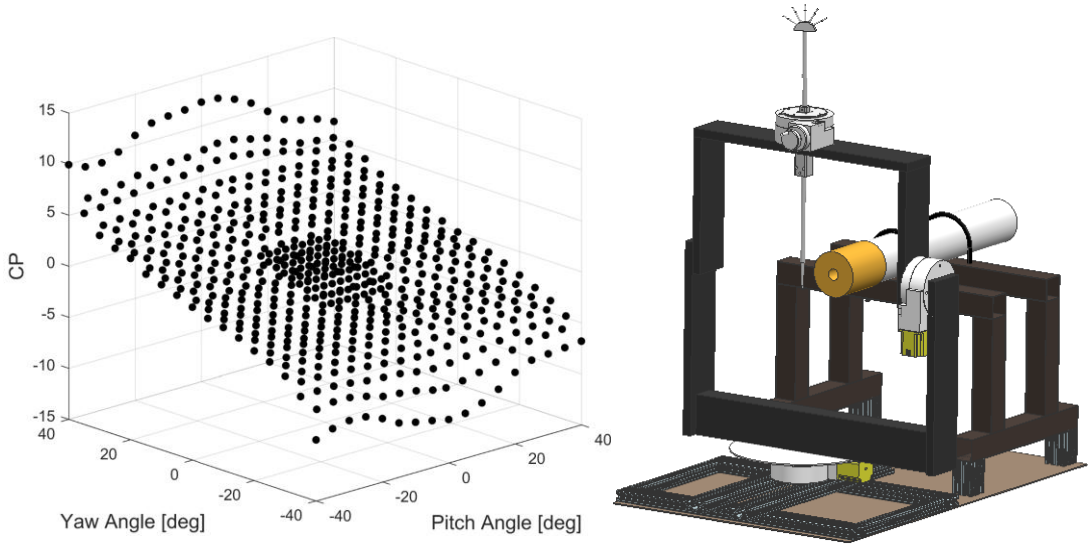

Figure 2.9. Pressure coefficient map (left) and calibration rig schematic (right).

Coefficients were calculated directly from the pressures measured at each pitch, yaw, and Mach number tested and took the form of Equation (2.3), with the coefficients only a function of the pitch and yaw angle of the probe.

$$CP = F(\alpha, \beta) \tag{2.3}$$

The pitch and yaw flow angle pressure coefficients were calculated using Equations (2.4) and (2.5), respectively, where the variable $\bar{P}$ is a pseudo average pressure that is calculated using Equation (2.6).

$$CP_{Pitch} = \frac{P_4 - P_5}{P_1 - \bar{P}} \tag{2.4}$$

$$CP_{Yaw} = \frac{P_2 - P_3}{P_1 - \bar{P}} \tag{2.5}$$

$$\bar{P} = \frac{1}{4}\sum_{i=1}^{4} P_i \tag{2.6}$$

The total and static pressure coefficients are calculated using Equations (2.7) and (2.8), respectively. P_T is the reference total pressure in the calibration tunnel and P_S is the atmospheric static pressure at the tunnel discharge.

$$CP_{Total} = \frac{P_1 - P_T}{P_1 - \bar{P}} \tag{2.7}$$

$$CP_{Static} = \frac{\bar{P} - P_S}{P_1 - \bar{P}} \tag{2.8}$$

2.2.3 Installation

Figure 2.10 shows a schematic and photograph of the installation setup. The probe was inserted into the fan case by way of a radial traverse that was electronically controlled outside of the test cell such that probe motion could occur during engine operation. The probe was fixed inside an alignment table that was used to null the probe in the yaw direction inside the engine prior to testing. The alignment table was attached to the radial traverse via a mounting sled. The slew for the traverse was approximately 6” for the inlet plane and 5” for the outlet plane. Radial positioning was verified during testing via the camera system shown in Figure 2.10-right. Further details on the traverse system can be found in previous publications [25].

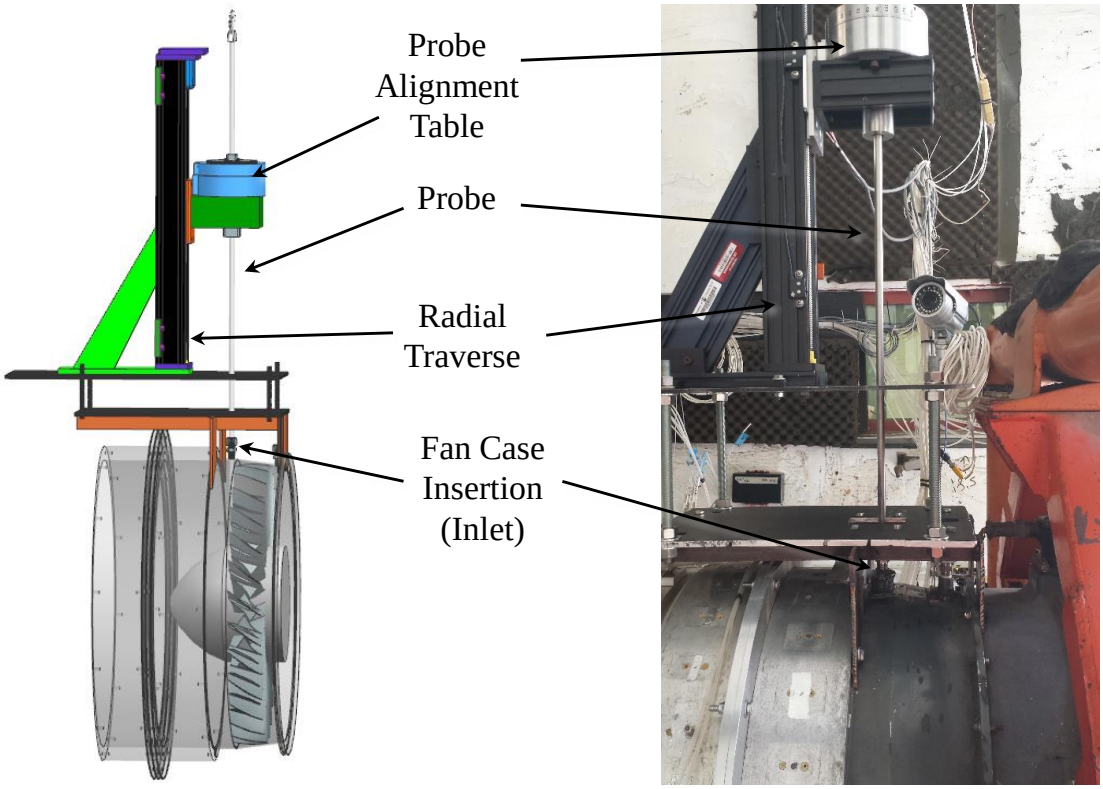

Figure 2.10. Probe installation schematic (left) and photograph (right).

2.3 Measurement Grids

2.3.1 Station 1 and Station 3

The static pressure taps at the Station 1 bellmouth measurement plane were located at 45 degree offsets from TDC and BDC. The four taps were equally spaced circumferentially around the tunnel and are shown schematically in Figure 2.11-left in blue markers overlaid on the uniform bellmouth inlet profile.

The AIP at Station 3 has 60 total pressure measurements and six static pressure taps. These are shown schematically in Figure 2.11-right, with the blue markers corresponding to the static taps and the black markers corresponding to the total pressure measurements. Only six static pressure taps were installed, equally spaced circumferentially around the tunnel wall starting at a 30 degree offset from TDC. The AIP rake produced 5 radial measurements at the geometric centers of equal area rings in 30° increments around the annulus. The distortion screen was rotated in 15° increments, which effectively doubled the circumferential resolution of both the static taps and rake total pressure measurements. The screen rotation also significantly increased the number of repeated measurements which reduced the installation bias for both the probes and taps.

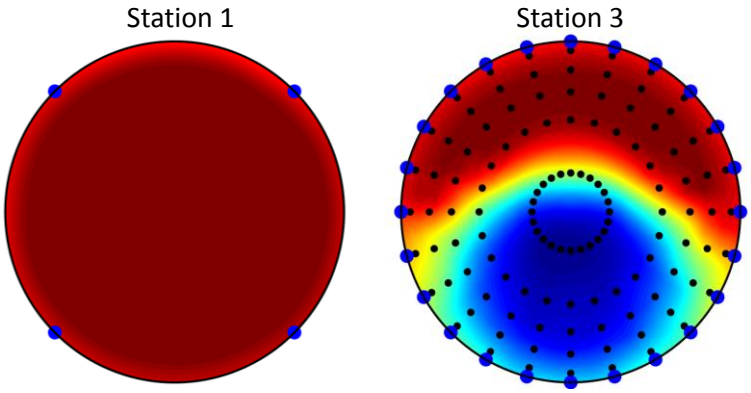

Figure 2.11. Measurement grids for Station 1 (left) and Station 3 (right).

2.3.2 Station 4 and Station 5

Due to the varying geometry of the fan inlet and outlet planes for Station 4 and Station 5, respectively, obtaining equivalent measurement grids was not feasible. Station 5 located the five-hole probe closer to the fan blades and since the blades were forward leaning from root to tip, the leading edge probe to trailing edge blade clearance decreased with plunge depth. Station 5 also placed the probe closer to the splitter, creating an interference with the probe reinforcement tube for large plunge depths. Despite these issues, sufficient radial measurement density was obtained for Station 4 (Figure 2.12-left) and Station 5 (Figure 2.12-center). Significant blade and engine geometry is identified in Figure 2.12-right.

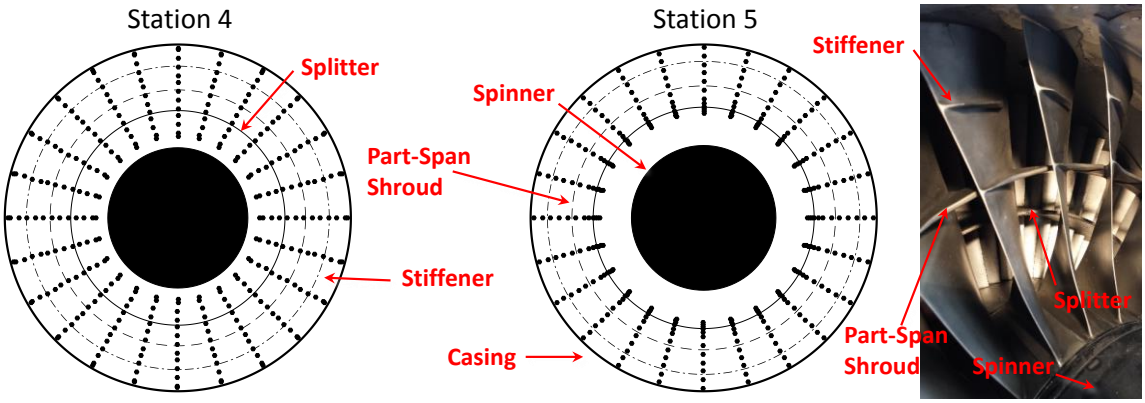

Figure 2.12. Measurement grids for Station 4 (left) and Station 5 (center) with fan blade geometry schematic (right).

2.4 Modified Turbofan Engine

All tests were conducted using a modified Pratt and Whitney Canada JT15D-1 turbofan engine, a picture of which is shown in Figure 2.13.

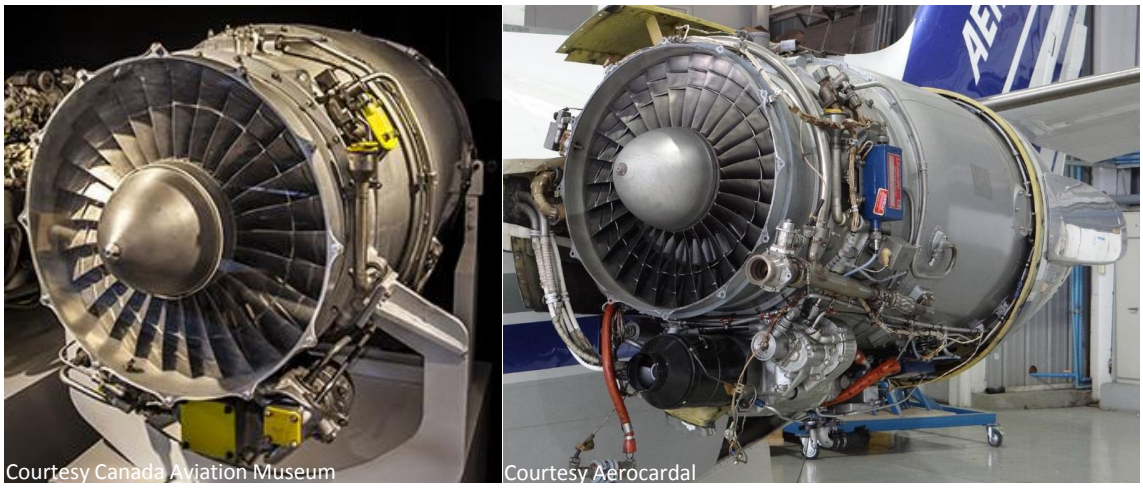

Figure 2.13. P&WC JT15D-1 turbofan engine.

At design conditions the transonic axi-centrifugal twin spool engine produces 2,200 lbs_f thrust and further design parameters are summarized in Table 2.1. Due to the strong distorted inlet conditions utilized, testing was completed at sub design conditions and the reduced engine performance is shown in Table 2.2 for all three distorted speeds tested.

Table 2.1. Modified JT15D-1 engine design parameters.

Fan Speed	16,000 RPM
Core Speed	32,000 RPM
Mass flow Rate	73.1 lbs_m/s
Fan Pressure Ratio	1.5
Bypass Ratio	3.3
Thrust	2,200 lbs_f
Fan Diameter	21 in
Number of Blades	28
Span Averaged Chord Length	2.74 in
Blade Tip Mach Number	1.3

Table 2.2. Engine performance parameters at distorted test conditions.

Corrected Fan Speed	**60%**	**70%**	**80%**
Mass flow Rate [lbs_m/s]	39.8	46.9	54.6
Fan Pressure Ratio	1.18	1.26	1.35
Blade Tip Mach Number	0.78	0.91	1.04

2.4.1 Blade Analysis

For good reason, engine manufacturers are concerned about the level of distortion ingested by the engines. While fatigue is of concern in regards to durability, a primary concern is excitation. Fan blades passing through pockets of low pressure distortion will experience an excitation as they traverse regions of low and high pressure during each

rotation, placing significant additional wear on the fan blade structure. This effect is further exacerbated for multiple-per-rev distortions.

2.4.1.1 Single-per-rev Excitation

The distortion pattern under study for this work was an intense, single-per-rev distortion, thus caution must be exercised to avoid exciting blade resonating frequencies. Shown in Figure 2.14 are the results of a modal analysis performed on the blade geometry to obtain the excitation frequencies, which is detailed in Appendix D. These frequencies were then compared to the engine order excitations via a Campbell diagram. Only the second engine order poses a serious concern as it intersects with the 1st mode frequency of the blade at approximately 61% fan speed, indicated in Figure 2.14-left. Care was taken during testing to ensure the engine avoided extensive operation at this condition, which was accomplished by reserving testing to cooler days when the uncorrected fan speed would be lower than 60% to match corrected conditions.

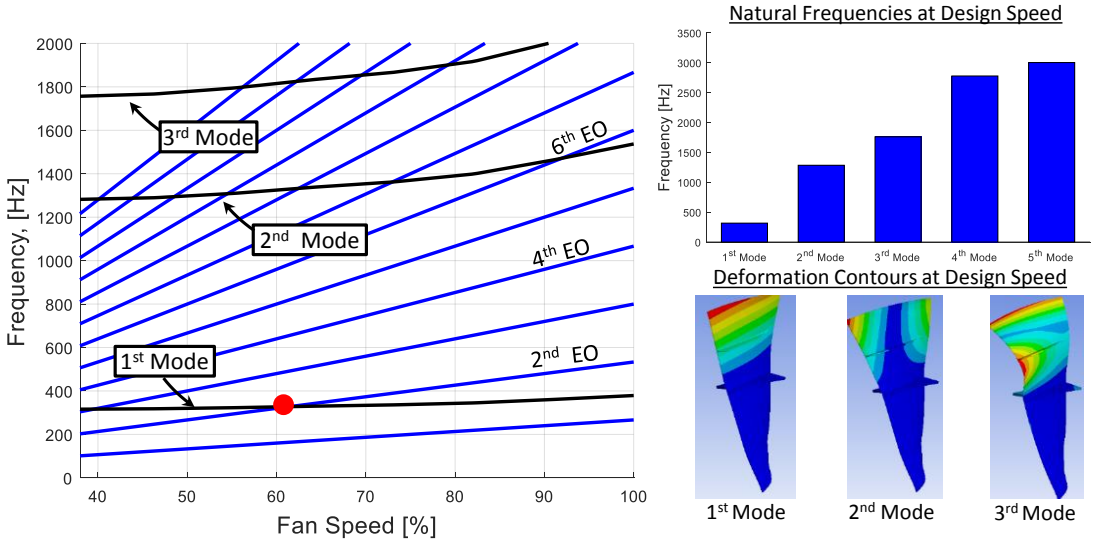

Figure 2.14. Campbell diagram (left) with accompanying modal frequency results at design speed (top-right) and deformation (bottom-right).

2.4.1.2 Metal Angles

To gain an understanding of the undistorted operating conditions of the engine it was necessary to obtain the metal angles of the fan blade. This was done by performing a three dimensional scan of the blade, breaking up the span into discrete sections, and then constructing the camber line at each section to obtain the leading and trailing edge angles. Figure 2.15 summarizes the process and results of this effort. A more detailed explanation of the process used, as well as a data table of the reversed engineered blade geometry, can be found in Appendix E.

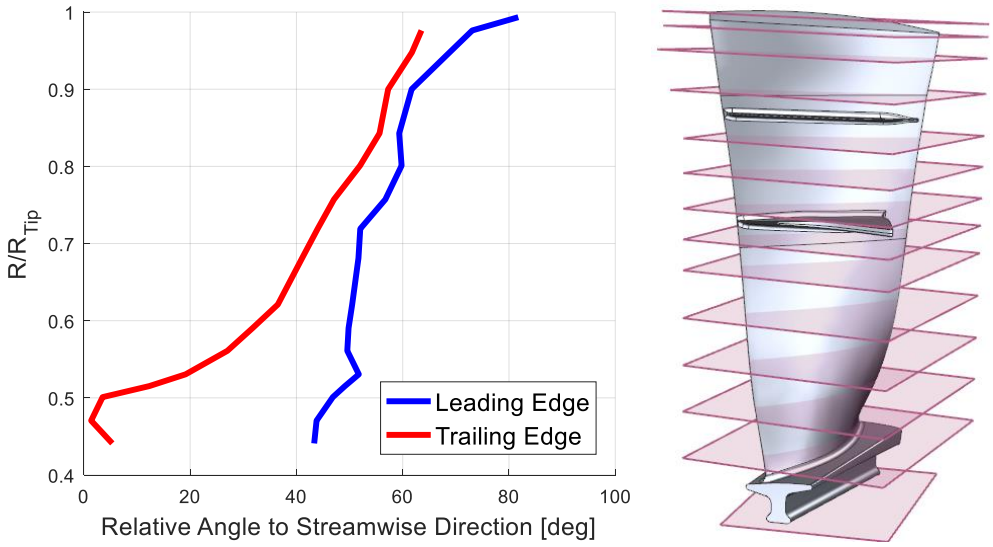

Figure 2.15. Metal angles of fan blade (left) and scan result deconstruction (right).

Chapter 3 Data Reduction

Due to the considerable amount of data required to complete this study, special care had to be taken to ensure adequate data quality. This was accomplished by verifying the experimental setup and transducer performance prior to and following each experiment. For these experiments, setup, inspection, and transducer calibration was performed before and after each test. Specifics on the methods utilized are described in the following sections.

3.1 Data Acquisition

A National Instruments™ (NI) digital data acquisition system measured and recorded all data obtained in the experiment, which included; voltage-output pressure transducers, a K-type thermocouple, and a voltage-output optical sensor used for accurate fan speed measurements.

3.1.1 Pressure

Two separate pressure transducer models were utilized in this experiment to account for the varying pressure ranges recorded. The manufacturer specifics for these transducers are summarized in Table 3.1.

Table 3.1. Pressure transducer specifications.

	Omega® PX139	Scanivalve® ZOC17
Full Scale Pressure Range	± 5 psig	± 15 psig
Accuracy	~ ± 0.32% Full Scale	± 0.08% Full Scale

The ZOC17 model was used to measure the five-hole probe pressures as well as three of the six AIP static pressures. All 60 total pressure measurements at the AIP, the remaining three static pressures at the AIP, and the four bellmouth static pressures were measured using the PX139's. All transducer outputs were measured and digitized in a NI PXI-6251 data acquisition card mounted inside a NI PXI-1044 chassis. Shielded wiring was used for both power and signal and tied into a common ground. The ZOC17 and PX139 had independent Agilent E3610A DC Power supplies. The pressure transducer outputs were sampled at 128 Hz.

3.1.2 Temperature

A single temperature measurement was recorded via the K-type thermocouple embedded in the five-hole probe. The thermocouple cabling terminated at a NI SCXI-1301 isothermal block which connected to an NI SCXI-1102 thermocouple signal conditioning

unit and digitized in a NI 6251 data acquisition card mounted in the chassis. The thermocouple output was sampled at 32 Hz.

3.1.3 Fan Speed

Fan speed was measured using an optical once-per-rev sensor system. A mirror-polished flat washer was installed on the tip of the engine spinner cone and the laser/encoder was mounted inside the tunnel wall of the experiment. A NI PXI-6251 data acquisition card measured and recorded the raw voltage output of the sensor and fan speed was calculated during post processing. A threshold subroutine was applied to the raw signal (Figure 3.1-left) to obtain the rotational frequency which was later resolved into fan speed (Figure 3.1-right). The once-per-rev signal was sampled at 500 kHz.

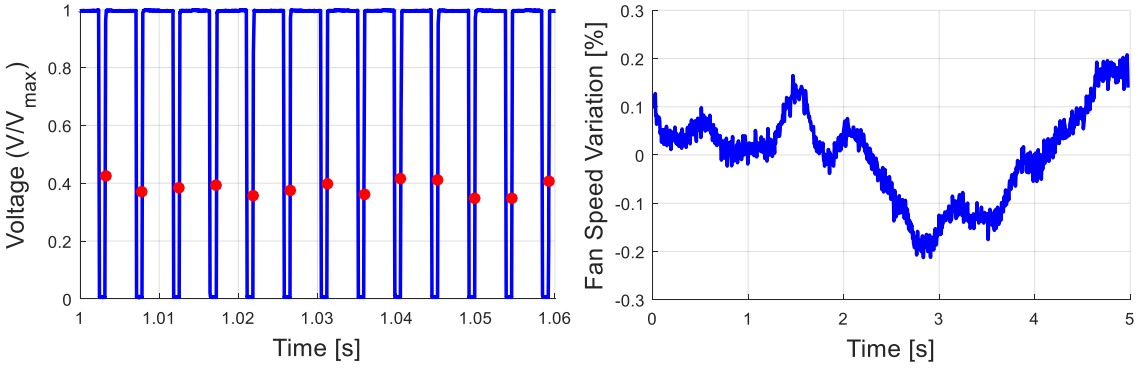

Figure 3.1. Optical once-per-rev post process (left) and resolved fan speed (right).

3.2 Data Collection

The motion control and data acquisition was controlled via an automated LabVIEW™ software program. Real-time data waveforms were monitored during the experiment such that any irregularities could be identified. In the event of such occurrences, tests were immediately aborted and restarted after corrections were performed at the point in the sequence prior to malfunction.

3.2.1 Sample time

A sample time of five seconds was chosen for all tests. This duration was selected considering several factors; previous experience, maintaining consistent inlet conditions, measurement grid density, test matrix size, and cost. Since these experiments require jet fuel to complete, lengthy test times can quickly become expensive. The primary driver for the sample time is the variation in engine operation condition over the course of a collection. The hydromechanical fuel control system onboard the engine limits how fine the power setting on the engine can be adjusted, thus during a data collection the fan speed can vary ±0.25% as shown in Figure 3.1-right. Longer collection times would result in an improved average, but a reduction in grid density or experimental conditions would be required to keep the experiment affordable.

Figure 3.2 shows a ‘good’ and ‘poor’ sample sixty second data collection for port one of the five hole probe during an experiment. As shown in both figures, the variability over the duration of the collection can be significantly more than the systematic uncertainty, with more than double the magnitude for the poor collection. These large scale fluctuations are caused primarily by the unsteady nature of the engine during operation. Good data collections, like Figure 3.2-left, show the running average within systematic uncertainty bounds for the duration of the collection, while the poor collection, shown in Figure 3.2-right, takes significantly longer for the running average to settle within the uncertainty bounds.

The majority of the measurements follow collection trends similar to the ‘good’ sample, where representative averages of the flow are obtained within five seconds, and thus a five second collection window was used for each measurement. For collections that were not well behaved, overall uncertainty was reduced via repeated experiments. For all data, a sample average was taken over the five second collection and treated as a single data point. The standard deviation of the five second signal was carried as random signal uncertainty through the overall uncertainty calculation.

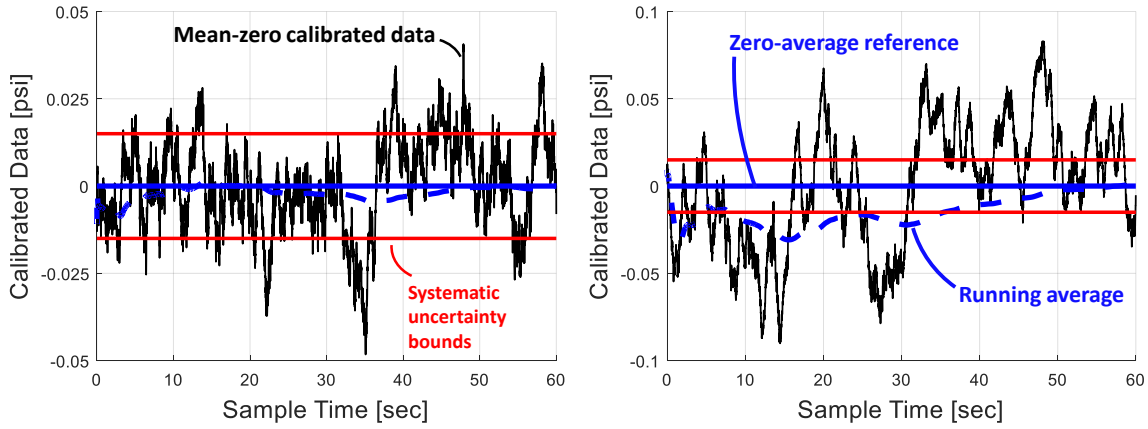

Figure 3.2. Good (left) and poor (right) sample calibrated pressure signal during 60 second data collection.

3.2.2 Test Replications

One of the most important components of experimental research and the scientific method is result verification; and the only way to accomplish this is through test replication. While one test result can be happenstance, and two tests with similar results can be coincidence, three experiments with similar results is indicative of a pattern. Using this framework, a minimum of three tests were performed for each test condition examined. Entire tests or subsets of tests that exhibited high variability between measurements were repeated further. This is particularly true of the undistorted cases, which were repeated ten to twelve times due to their lower time duration (less than 5% of a distorted test).

The number of test replications were factored into the overall uncertainty via the standard error, as calculated in Equation (3.1)

$$s_{\bar{x}} = \frac{s_x}{\sqrt{N}} \tag{3.1}$$

where s_x is the standard deviation of the data sample vector of repeated with measurement size, *N*.

3.2.3 Pressure Calibration

Static calibrations were performed on all transducers before and after each test. An example calibration curve is shown in Figure 3.3-left involving several transducers. The pressure transducer measurements were post processed by taking an average of the calibration curves between the pre- and post-test calibrations and applying to all data collected. Accompanying all calibration curves is an uncertainty relationship (Figure 3.3-right) that is also applied to each data point collected and carried as a systematic calibration uncertainty throughout the data reduction process. Details of the uncertainty methodology is described in Section 3.8. A NIST-traceable Dwyer™ digital manometer was used as the pressure reference. The calibration pressure source was compressed nitrogen that was downregulated to the required input value.

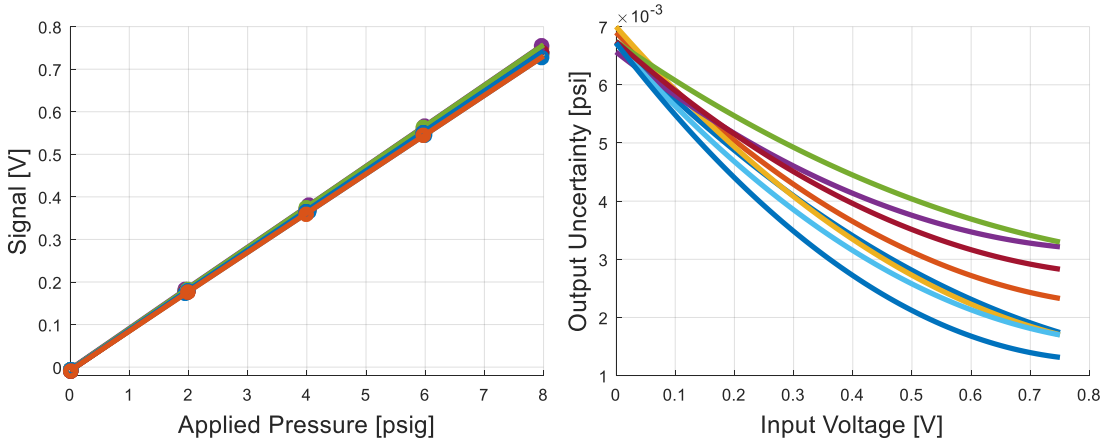

Figure 3.3. Static calibration (left) and uncertainty (right) curves of the pressure transducers.

3.3 Inlet Conditions

For each test configuration investigated (fan speed and profile) discrete points at Station 4 and Station 5 had to be taken to obtain the full profile. This took approximately 1.5 hours, in which case the engine fan speed had to be maintained as consistently as possible to corrected conditions. The following subsections describe how well these conditions were maintained using Equations (3.2) and (3.3) as the parameter metric, where RDFA represents the Relative Difference From Average and RDFT is the Relative Difference From Target.

$$Y_{RDFA} = 100 * \left(\frac{\left| Y_{Measured} - Y_{Average} \right|}{Y_{Average}} \right) \tag{3.2}$$

$$Y_{RDFT} = 100 * \left(\frac{\left| Y_{Measured} - Y_{Target} \right|}{Y_{Target}} \right) \tag{3.3}$$

3.3.1 Bellmouth Static Taps

The bellmouth measurement plane at Station 1 utilized four static pressure taps equally spaced circumferentially around the tunnel. Figure 3.4 shows the measurement consistency for each test case investigated. Higher fan speeds trended toward higher variability amongst the measurements and distorted and undistorted cases show close agreement. Since the magnitude of the variation is within 0.55% RDFA for all cases, the measurement variability for the static taps was concluded to be sufficiently low.

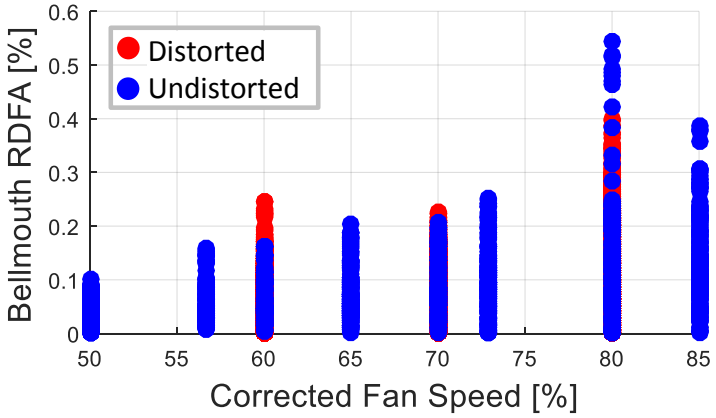

Figure 3.4. Bellmouth static pressure tap measurement consistency.

3.3.2 Mass Flow Rate Calculation

The mass flow rate was calculated through an iterative procedure incorporating a series of three relationships between the Reynold's Number (Re), mass flow rate ($\dot{m}$), and bellmouth discharge coefficient (C_D). The Re and $\dot{m}$ are solved for using Equations (3.4) and (3.5), respectively, and Figure 3.5-left is used to obtain C_D. For Equation (3.4), μ is the kinematic viscosity of air (8.9×10^{-4} kg/(m·s)) and d is the tunnel diameter (21in). For Equation (3.5), P_T and P_S is the total and static pressure in the tunnel, respectively, γ is the specific heat ratio of air as an ideal gas (used under standard atmospheric conditions as 1.4), M_{air} is the molecular weight of air (28.97 g/mol), T_T is the total temperature in the tunnel, and R is the specific gas constant for air (287 J/(kg·K)).

The data from Figure 3.5-left was obtained from the bellmouth calibration performed at the Virginia Tech TurboLab, details of which can be found in [20]. Figure 3.5-right

shows the uncertainty inherent in the calculation of C_D, which is carried as systematic uncertainty in the calculation of the overall uncertainty. Details of the uncertainty methodology is described in Section 3.8.

$$Re_d = \frac{4 * \dot{m}}{\pi * \mu * d} \tag{3.4}$$

$$\dot{m} = C_D \left(\frac{\pi}{4} d^2\right) P_T \sqrt{\left(\frac{2\gamma g_c M_{air}}{T_T R(\gamma - 1)}\right)\left(\frac{P_S}{P_T}\right)^{\frac{2}{\gamma}}\left[1 - \left(\frac{P_S}{P_T}\right)^{\frac{\gamma-1}{\gamma}}\right]} \tag{3.5}$$

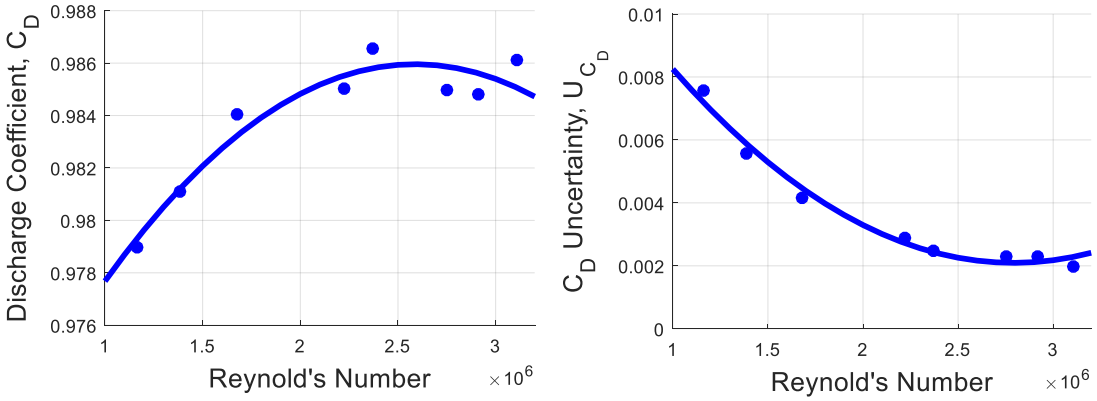

Figure 3.5. Discharge coefficient (left) and discharge coefficient uncertainty (right).

3.3.3 Mass Flow Rate and Fan Speed Consistency

The calculated mass flow rate and measured fan speed were kept as consistent as possible over the course of each test in order to validate the assumption of constant inlet flow conditions between measurement locations and test replications. Figure 3.6 shows the variability of the mass flow rate (left) and fan speed (right) between these measurements for the different test conditions investigated. The results show higher variability for the distorted cases and consistent ranges across fan speeds. The variability between measurements is small when compared to the parameter magnitude as indicated by the RDFA (Figure 3.6-left) and RDFT (Figure 3.6-right) values, validating the consistent inlet condition assumption.

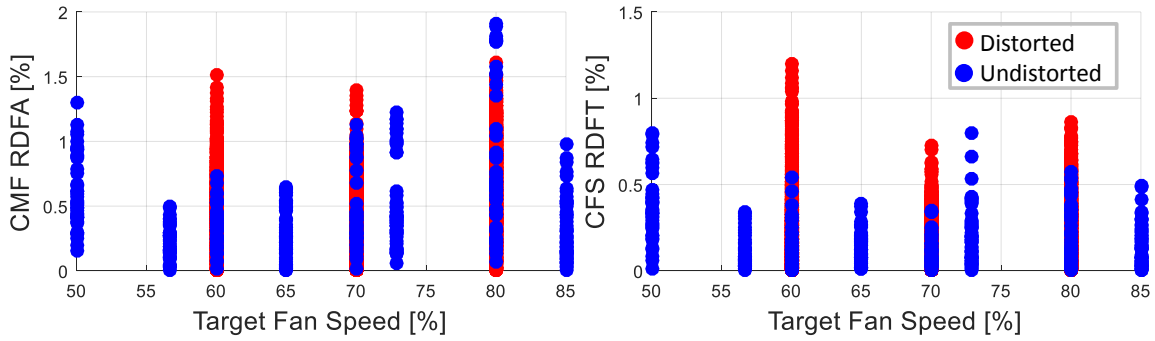

Figure 3.6. Corrected mass flow and fan speed measurement consistency.

3.4 AIP

3.4.1 Total Pressure Consistency

The variability in the total pressure measurements is shown in Figure 3.7 for the 70% CFS case, with the distorted data plotted on the left and the undistorted on the right. The maximum RDFA (Equation (3.2)) for each location is plotted and both the distorted and undistorted cases show insignificant variation as indicated by the 0.12% maximum magnitude. Thus the inlet mass flow variation shown from Figure 3.6-left caused insignificant variation on the pressure profile, further validating the consistent inlet condition consumption. Variability is higher in the distorted case due to the larger pressure variation in the profile as well as the secondary flow inherent from the flow redistribution, which will be examined in detail in Chapter 4. Previous literature examines this phenomenon in greater detail [23].

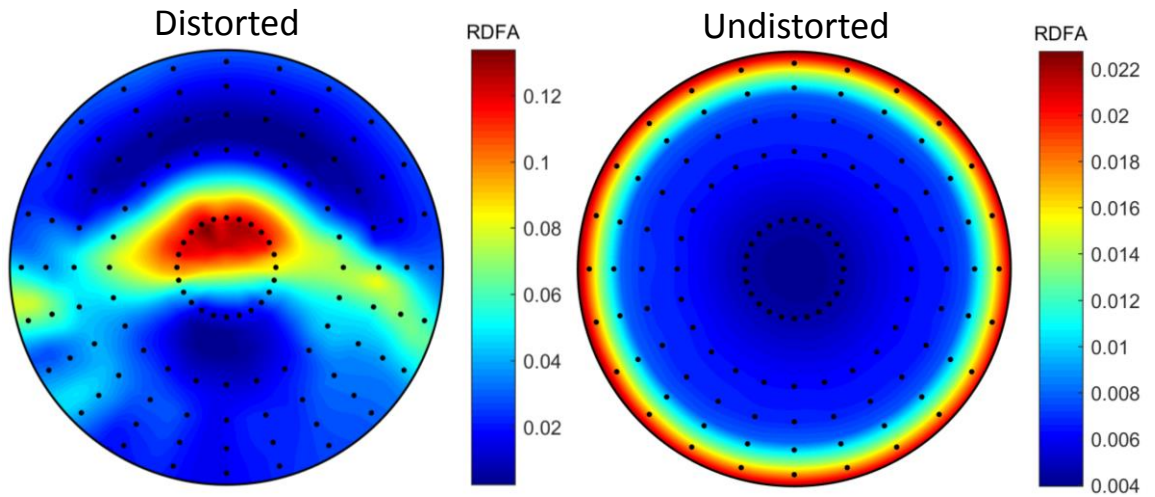

Figure 3.7. AIP total pressure measurement variability.

3.4.2 Static Pressure Consistency

Figure 3.8 shows the static pressure variability at the AIP for the different test cases investigated. The distorted profiles produce significantly higher variability and show a strong correlation to fan speed while the undistorted profiles show consistent variation magnitude across fan speeds. The calculated RDFA variation between repeated tests cases is shown to be satisfactorily small.

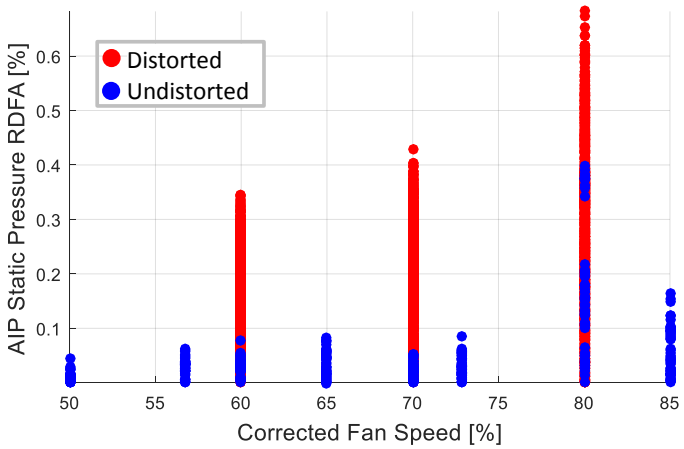

Figure 3.8. AIP static pressure taps measurement variability.

3.5 Five Hole Probe

3.5.1 Pressure and Flow Angularity

The non-nulling calibration described in Chapter 2 allowed for the creation of pressure coefficient maps that were used in the determination of flow angles and total and static pressure from experimental data. This was done by creating interpolation functions of the form given in Equation (3.6), where ψ represents the pitch and yaw flow angles, and the total and static pressure coefficients.

$$\psi = F(CP_{Pitch}, CP_{Yaw}) \tag{3.6}$$

The total and static pressures were calculated using Equations (3.7) and (3.8), respectively, where $\bar{P}$ and P_1 are defined in Section 2.2 and CP_{Total} and CP_{Static} are calculated from Equation (3.6).

$$P_T = P_1 - CP_{Total}(P_1 - \bar{P}) \tag{3.7}$$

$$P_S = \bar{P} - CP_{Static}(P_1 - \bar{P}) \tag{3.8}$$

Once the total and static pressures were known, the flow Mach number was calculated using Equation (3.9).

$$M = \sqrt{\frac{2}{\gamma - 1}\left[\left(\frac{P_T}{P_S}\right)^{\frac{\gamma-1}{\gamma}} - 1\right]} \tag{3.9}$$

3.5.2 Total Temperature

The total temperature was measured directly from the K-type thermocouple embedded in the sensing head of the probe.

3.5.3 Static Temperature

The static temperature, which was utilized to calculate the local flow velocities, was calculated using Equation (3.10), where T_T and T_S are the total and static temperatures, respectively.

$$T_S = \frac{T_T}{\left(1 + \frac{\gamma - 1}{2} M^2\right)} \tag{3.10}$$

3.5.4 Component Velocities

Once the static temperature was known, the velocity magnitude, $C_{rz\theta}$, was calculated utilizing the speed of sound, Equation (3.11), and the Mach number previously determined, as shown in Equation (3.12).

$$a = \sqrt{\gamma R T_S} \tag{3.11}$$

$$C_{rz\theta} = Ma \tag{3.12}$$

The velocity magnitude was then decomposed into polar coordinates as illustrated in Figure 3.9 via coordinate transformations, which follows from Treaster [36]. This results in the calculation of the radial, tangential, and axial velocity using Equations (3.13) - (3.15), respectively.

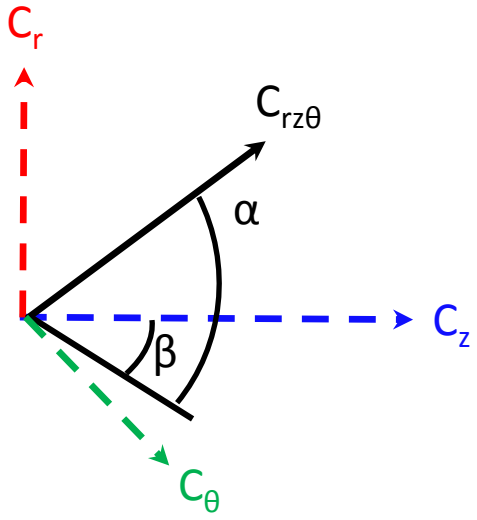

Figure 3.9. Polar coordinate velocity components.

$$C_r = C_{rz\theta} \sin(\alpha) \tag{3.13}$$

$$C_\theta = C_{rz\theta} \cos(\alpha) \sin(\beta) \tag{3.14}$$

$$C_z = C_{rz\theta} \cos(\alpha) \cos(\beta) \tag{3.15}$$

3.6 Fan Performance Parameters

Using the results obtained from Section 3.5, fan performance metrics were calculated using classical turbomachinery relationships. The following sections outline the equations used to obtain the parameters discussed in Chapter 4.

3.6.1 Incidence and Deviation

Using the component velocities calculated in Section 3.5, classical velocity triangles were constructed using a mean-line analysis such that the blade relative flow parameters could be calculated, as shown in Figure 3.10-left.

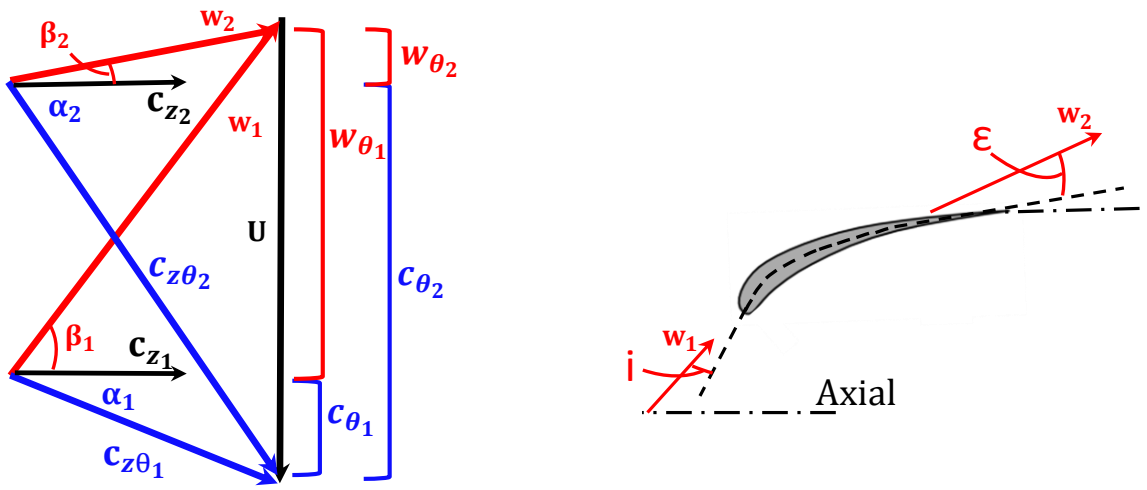

Figure 3.10. Schematic of rotor velocity triangles (left), and incidence (i) and deviation (ε) angles (right).

Blade relative flow angles at the inlet and outlet to the rotor, β_1 and β_2, were calculated using Equation (3.16), where U is the blade speed.

$$\beta = \tan^{-1}\left(\frac{U - C_\theta}{C_z}\right) \tag{3.16}$$

The leading edge metal angle is subtracted from the inlet relative flow angle to calculate the blade incidence, as shown in Equation (3.17), which is a representation of how far off-design the leading edge flow angle is. Positive incidence is indicative of the relative flow approaching more heavily on the pressure surface of the blade and negative incidence is indicative of the flow approaching more heavily on the suction surface.

$$i = \beta_{Inlet\ Flow} - \beta_{Metal\ Leading\ Edge} \tag{3.17}$$

The trailing edge metal angle is subtracted from the outlet relative flow angle to calculate the blade deviation, as shown in Equation (3.18). This parameter represents the magnitude of under turning or premature separation (negative values) and overturning (positive values). Overturning is a rare occurrence and is usually the result of non-uniform flows and non-standard fan geometry affecting the aerodynamics.

$$\epsilon = \beta_{Outlet\ Flow} - \beta_{Metal\ Trailing\ Edge} \tag{3.18}$$

3.6.2 Blade Loading

Blade loading is a representation of how much turning the blade is required to perform in order to maintain a constant work input across the rotor. This parameter is strongly dependent on the blade speed, as shown in Equation (3.19). Higher blade loading requires more output from the vanes, pushing them closer to their separation and stall limits.

$$\frac{\Delta h_0}{U^2} = \frac{\Delta C_\theta}{U} = 1 - \frac{c_{z_2}}{U_2} tan\,\beta_2 - \frac{c_{z_1}}{U_1} \tan \alpha_1 \tag{3.19}$$

Assuming constant U and constant axial velocity C_z through the rotor, Equation (3.19) can be simplified to Equation (3.20).

$$\frac{\Delta C_\theta}{U} = \ 1 - \frac{c_z}{U} (tan\,\beta_2 + \tan \alpha_1) \tag{3.20}$$

3.6.3 Pressure Rise

The pressure rise across the rotor is calculated by dividing the outlet local total pressure by the corresponding inlet total pressure, as shown in Equation (3.21).

$$PR = \frac{P_{T_2}}{P_{T_1}} \tag{3.21}$$

3.6.4 Efficiency

Combining the pressure ratio and blade loading, the local efficiency was calculated using Equation (3.22), where γ is the specific heat ratio for an ideal gas, c_p is the specific heat of air at constant pressure, and T_{T_1} is the total temperature at the fan inlet.

$$\eta = \frac{c_p T_{T_1}}{U \Delta C_\theta} \left[\left(\frac{P_{T_2}}{P_{T_1}} \right)^{\frac{\gamma-1}{\gamma}} - 1 \right] \tag{3.22}$$

3.6.5 Lieblein Diffusion Factor

The amount of turning possible across a blade, and thus the allowable work input, is limited by the amount of diffusion possible within a blade passage. The Lieblein diffusion factor, calculated in Equation (3.23), is the parameter most often used in determining excessive diffusion. Typical compressor designs limit the LDF to < 0.5 [28]. Figure 3.10-left can be used as a reference for the terminology in Equation (3.23). The parameters s

and c represent the blade spacing and chord, respectively. The chord to spacing ratio, c/s, is termed the solidity.

$$LDF = 1 - \frac{w_2}{w_1} + \frac{s}{c}\left(\frac{1}{2}\right)\left(\frac{w_{\theta_2} - w_{\theta_1}}{w_1}\right) \tag{3.23}$$

3.6.6 Mass Flux

The local mass flux, expressed as the mass flow rate per unit cross sectional area, is a representation of the local mass flow at a discrete point within the flow and was calculated with the flow parameters obtained from the five-hole probe. Combined with the local pressure rise, the mass flux can be used to approximate the fan performance characteristic which is shown later in Chapter 4.

$$\frac{\dot{m}}{A} = \frac{P_T\sqrt{\gamma}}{\sqrt{RT_T}} M \left(\frac{1}{1 + \frac{\gamma - 1}{2} M^2}\right)^{\left(\frac{\gamma+1}{2(\gamma-1)}\right)} \tag{3.24}$$

3.7 Comparison Metrics

3.7.1 Corrected Conditions for Fan Performance

Due to the strong secondary flow present for the distorted cases and that which is inherent in turbomachinery, it was necessary to develop a means of tracking streamtubes between measurement planes: from Station 4 to Station 5. This was accomplished by calculating circumferential and radial shift based on the flow velocity in those respective directions. For example, Figure 3.11 shows a graphical representation of the circumferential shift of a streamtube as it travels from Station 4 to Station 5.

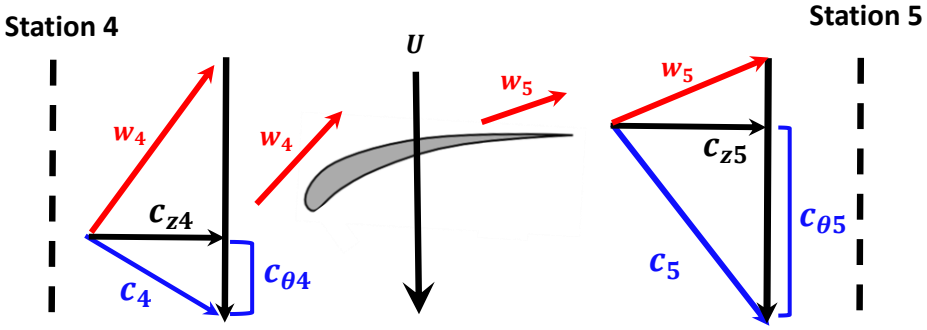

Figure 3.11. Schematic representing the components required for calculating circumferential displacement.

The streamtube travel path is broken into three sections:

1) Measurement Station 4 to the fan blade leading edge
2) Fan blade leading edge to the fan blade trailing edge
3) Fan blade trailing edge to measurement Station 5

The duration each fluid particle spends in sections 1) and 3) is calculated by Equation (3.25) while the duration through the fan is calculated similarly but using the average relative velocities, w_4 and w_5, in place of the axial velocity (C_Z) and the blade chord length in place of the axial length (z_z).

$$t = \frac{z_z}{C_z} \tag{3.25}$$

The tangential velocity component, C_θ, is then used in Equation (3.26) to calculate the circumferential displacement, where C_ψ represents a polar coordinate velocity.

$$D_\psi = C_\psi * t \tag{3.26}$$

This procedure is performed for each section and the overall displacement between Station 4 and Station 5 is obtained with a summation.

A similar procedure is performed for the radial displacement from Station 4 to Station 5 with the exception of using the radial velocity component, C_r, when utilizing Equation (3.26) to calculate displacement in place of the tangential velocity component, C_θ. A graphic representation is shown in Figure 3.12.

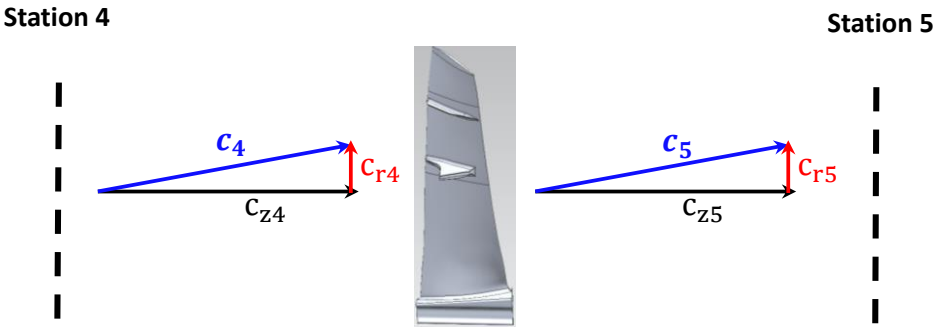

Figure 3.12. Schematic representing the components required in calculating radial displacement.

3.7.2 Data Presentation: Relative Difference from Undistorted

The majority of the distorted data is presented in a format called 'Relative Difference from Undistorted' (RDFU), calculated in Equation (3.27) where Y represents a measured or calculated parameter. This descriptor was used as a means of showing the parameter variation due to the distorted inlet conditions in relation to the undistorted conditions at equal fan speed, effectively removing the design nuances of the fan from the presented

results. For the results discussed in Chapter 4, this parameter is typically used in the data plots, presented as a percent (%), and abbreviated as RDFU.

$$Y_{RDFU} = 100 * \left(\frac{Y_{Distorted} - Y_{Undistorted}}{Y_{Undistorted}}\right) \tag{3.27}$$

For flow angles, a difference calculation is performed between the distorted and undistorted cases, as shown in Equation (3.28).

$$\Delta Y = Y_{Distorted} - Y_{Undistorted} \tag{3.28}$$

3.8 Uncertainty

The uncertainty for this study was determined through careful analysis of the calibration and measurement techniques utilized. Every measurement had a quantifiable uncertainty associated with it that was carried throughout the analysis procedure, from transducer calibration to parameter calculation. Recall from Figure 3.3-right, the uncertainty components associated with static transducer calibrations before and after each experiment. These uncertainty curves were established for each transducer and the uncertainty associated with each measured value was determined from the voltage recorded at the time of measurement. Combining these calibration uncertainties with the random uncertainties associated with repeated measurements, an overall uncertainty was obtained.

3.8.1 Measured Parameter

The overall uncertainty for a measured parameter is given in Equation (3.29) where the confidence interval used for the investigation was set at 95%.

$$u_{95} = t_{\nu,95} * \sqrt{s_{\bar{x}}^2 + \sum_{k=1}^{L} b_k^2 + \sum_{k=1}^{M} s_k^2} \tag{3.29}$$

A student's t-distribution, t_ν, was chosen as the mean estimation parameter, with ν representing the number of observations. Equation (3.29) utilizes the standard error, $s_{\bar{x}}$, defined in Equation (3.1). The systematic error sources in the system, b_k, represent measurement bias due to a number of factors; calibration reference, linear data fits, electrical wiring, pneumatic plumbing, data acquisition, signal conditioning, etc. The random error sources, s_k, represent fluctuations in the recorded data signal and include the standard deviation of the transducer signal for both the static calibration and the experimental measurement signal. The random error associated with the calibrations was very small and could have been considered negligible but was kept throughout the study for completeness. Uncertainties obtained from Equation (3.29) were obtained for each

unique measurement location, where repeat measurements were accounted for in the standard error, $s_{\bar{x}}$.

3.8.2 Five Hole Probe Parameters

The uncertainty associated with the five hole parameters has two additional components due to the non-nulling probe calibration performed. This is shown in Equation (3.30), where u_{cal} is the transducer calibration uncertainty from the probe calibration, u_{int} is the interpolation uncertainty associated with the interpolation schema employed when using the calibration maps to determine the flow parameters, and u_{exp} is the experimental uncertainty calculated in Equation (3.29) from the measured experimental engine data.

$$u_{FHP} = \sqrt{u_{cal}^2 + u_{int}^2 + u_{exp}^2} \tag{3.30}$$

The transducer calibration uncertainty, u_{cal}, is calculated similarly for the experimental engine data as the probe calibration incorporates several replicated data sets to ensure data quality. Pre and post-test transducer calibrations were performed for each probe calibration test and the uncertainties associated with each test were accounted for. The final overall probe calibration uncertainty is calculated using Equation (3.29).

The interpolation uncertainty is calculated using a jackknife approach, further details of which can be found in Tomczak [32]. The procedure essentially tests the 'goodness' of the interpolation schema utilized during post processing. This is performed by first calculating a pseudo-value five hole parameter (total pressure, static pressure, yaw angle, pitch angle), $\hat{Y}_i$, for each calibration data point 'i' as shown in Equation (3.31).

$$\hat{Y}_i = IY_{All} - (I-1)Y_{All-i} \tag{3.31}$$

I represents the total number of calibration points used in the interpolation, which for a two dimensional interpolation is 4. The parameters Y_{All} and Y_{All-i} represent the parameter of interest calculated utilizing all calibration points and with calibration point 'i' removed from the map, respectively. The interpolation uncertainty is then calculated using Equation (3.32). This procedure was performed for each unique experimental data point.

$$u_{int} = \sqrt{\frac{1}{I(I-1)}\sum_{i=1}^{I}\left(\hat{Y}_i - Y_{All}\right)^2} \tag{3.32}$$

Table 3.2 summarizes the RMS (Root Mean Square) nominal uncertainties for each term in Equation (3.30), where RMS is defined in Equation (3.33), where *N* is the data sample length and Ψ is the parameter of interest.

$$RMS = \sqrt{\frac{1}{N}\sum_{k=1}^{N} \Psi^2} \tag{3.33}$$

For the cases of percent (%) nominal, the parameter of interest, Ψ, is a dimensionless relative difference between the uncertainty and the nominal value, as calculated using Equation (3.34), where ψ represents the dimensioned parameter of interest.

$$\Psi = \frac{\psi_{Nominal} - \psi_{Uncertainty}}{\psi_{Nominal}} \tag{3.34}$$

As shown in Table 3.2, the uncertainty associated with the engine experiments has the highest contribution to the overall uncertainty, followed by the probe calibration uncertainty, and finally the interpolation map. This table shows that the probe calibration performed was sufficiently accurate for the experiments conducted.

Table 3.2. Five-hole parameter RMS uncertainty.

[RMS % Nominal]	$\boldsymbol{u_{cal}}$	$\boldsymbol{u_{int}}$	$\boldsymbol{u_{exp}}$	$\boldsymbol{u_{FHP}}$
Total Pressure	0.04	0.02	0.60	0.60
Static Pressure	0.08	0.02	0.14	0.16
Yaw Angle	0.59	0.32	1.39	1.54
Pitch Angle	1.68	0.71	4.23	4.61

3.8.3 Calculated Parameters

The uncertainty associated with calculated parameters was determined using a sequential perturbation technique, with details of the procedure found in Appendix B. Table 3.3 summarizes the RMS nominal values of the calculated parameter uncertainties presented throughout the dissertation.

Table 3.3. Measured and calculated parameter RMS uncertainty values given as a percent of the nominal value.

[RMS % Nominal]	$u_{95\%}$
CFS	3.5
Mass flow	6.2
Bellmouth Static Pressure	0.9
AIP Total Pressure	2.4
AIP Static Pressure	1.3
Total Temperature	9.5
Incidence	2.9
Deviation	2.9
Blade Loading	3.4
Pressure Rise	8.7
Efficiency	16.4
Lieblein Diffusion Factor	8.9
Mass flux	9.4

Chapter 4 Results and Discussion

4.1 Consistent Inlet Conditions

Since the probe and distortion screen were traversed and rotated, respectively, to obtain the measurement field, it was important to ensure that consistent inlet conditions were maintained between measurements. This was accomplished by continually monitoring and adjusting the uncorrected fan speed as atmospheric conditions varied over the course of a test. A similar procedure was performed between tests, which occurred on different days and different atmospheric conditions. The uncorrected fan speed was calculated real-time using Equation (4.1), where N_{cor} is the corrected fan speed (60, 70, 80%), and T_{atm} was the current local atmospheric temperature and T_{std} was the standard reference temperature used in the investigation (59°F). Figure 2.7 shows the consistency of such a procedure, which lead to the acceptable uncertainties listed in Table 3.3.

$$N_{uncor} = N_{cor} \cdot \sqrt{\frac{T_{atm}}{T_{std}}} \tag{4.1}$$

For all test configurations and speeds investigated, the corrected fan speed was kept to within ± 0.4%, and the corrected mass flow, Reynold's number, and tunnel Mach number were kept to within ± 1.2% of the target value. These variations represent 2 standard deviations of the sample population data. No distortion screen dependent variations were found in any of the above parameters mentioned.

4.2 Undistorted Inlet Flow Conditions

Undistorted fan performance conditions were obtained for two reasons; the first was to provide a means of comparison for the distorted conditions, and the second was to gain an understanding how the engine performs in the undistorted experimental rig utilized. The engine was always operating in off-design conditions, even in the undistorted inlet flow experiments due to the pressure loss of the backing screen. The bellmouth, accompanying tunnel sections, and AIP rake all contribute to losses in the overall system that must be accounted for. This was done with duplicating the measurements made in the distorted tests for the undistorted conditions. The following subsections highlight the results.

4.2.1 Station 3 - AIP Inlet Profile

The inlet total pressure profile for three respective test speeds investigated is shown Figure 4.1. Low losses through the experimental rig ducting is shown for the 50% CFS test conditions, with increasing losses for increasing fan speed. A more pronounced boundary layer becomes prevalent in the 65% CFS case and is at its most severe at 85% CFS. Figure

4.1 shows a uniform inlet profile for the test conditions evaluated, providing a valid inlet profile to compare against for distorted conditions. AIP static pressure results are included later in the document in the distorted inlet flow discussion of Section 4.3.

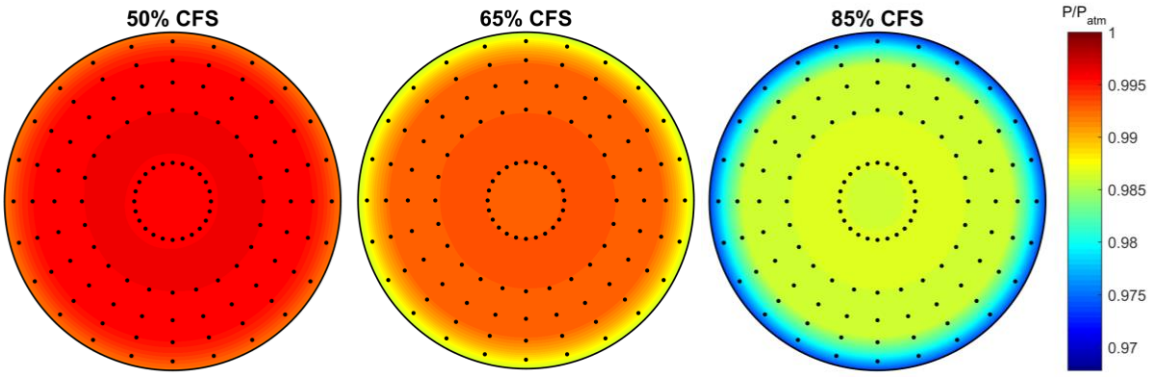

Figure 4.1. AIP total pressure contours for varying speed undistorted inlet conditions.

4.2.2 Station 4 and Station 5 - Fan Inlet and Fan Outlet Conditions

Undistorted data measured at Station 4 (fan inlet) and Station 5 (fan outlet) are summarized in the following subsections. For conciseness, both stations are plotted together, with solid lines representing Station 4 (fan inlet) and dashed lines representing Station 5 (fan outlet). Fan blade geometry (splitter, part-span shroud, stiffener) is additionally plotted for reference as their effects on the measurements are distinguishable.

4.2.2.1 Total and Static Pressure

The undistorted total and static pressure distributions at Station 4 and Station 5 are shown in Figure 4.2, with the total pressure results shown on the left and the static pressures shown on the right. Data is colored according to %CFS and referenced in the colorbar on the far right of the plot.

The inlet total pressure of Figure 4.2-left is well behaved across fan speeds; the only component of note is the drop in total pressure radially outward beyond the stiffener for CFS beyond 72.9%, which correspond to transonic conditions. The subsequent increase in static pressure for similar conditions (Figure 4.2-right) supports this. Station 5 total pressure also shows a well behaved distribution, with increasing fan output pressure for increasing blade span. The part-span shroud causes a disruption in the linearity of the distribution, and the mid-core region shows a more aggressive rise in total pressure before reducing as it approaches the splitter. Otherwise, the blade geometry effects on the undistorted total pressure distribution are small.

The static pressure distribution of Station 5 in Figure 4.2-right is more varied than the total pressure due to the profound effect the splitter has on the upstream measurements. The measurement plane of Station 5 is directly upstream of the splitter as engine geometry constraints prevented the plane from being further upstream. With the total pressure distribution unchanged in this region (Figure 4.2-left), the reduced flow velocity as it approaches the splitter will cause an increase in the static pressure as shown. Other than

the splitter effects, the static pressure distribution is similar to the total pressure, increasing in sensitivity with increasing CFS. The tip region of the static pressure distribution shows a slight reduction, indicating higher velocity flow as the total pressure distribution is unchanged.

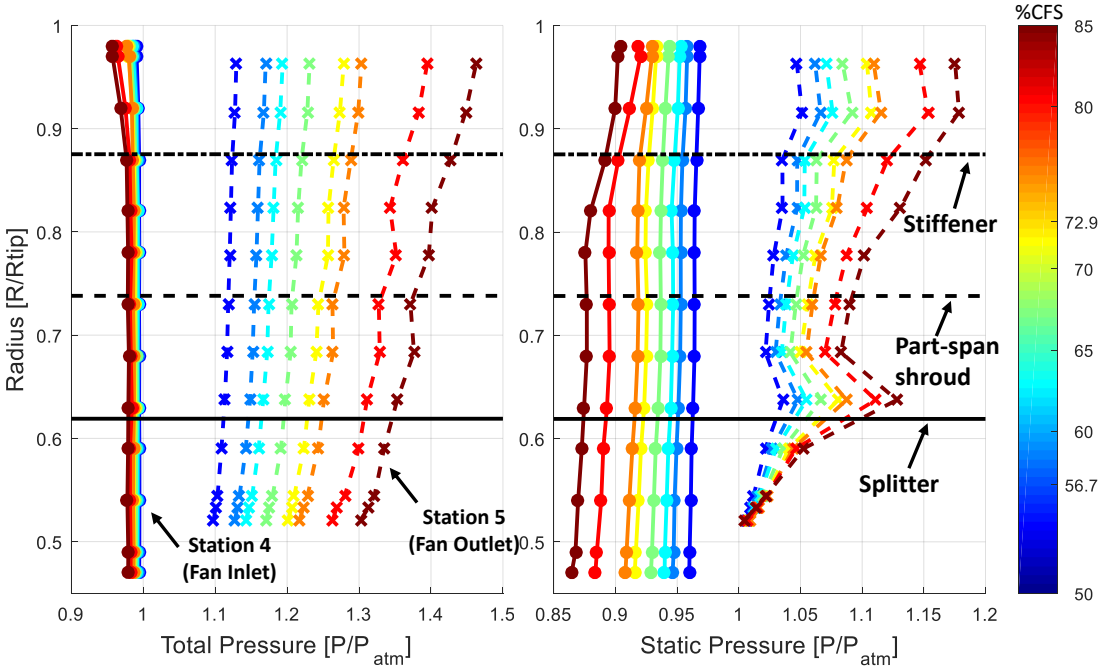

Figure 4.2. Undistorted total (left) and static (right) pressure for Station 4 and Station 5.

4.2.2.2 Tangential and Radial Flow Angle

The undistorted tangential and radial flow angles are plotted in Figure 4.3. The tangential flow angle (Figure 4.3-left) at Station 4 has a small, bulk fan-wise pre-swirl component that does not vary significantly in the radial direction. Near core flow will be heavily influenced by the spinner while bypass flow will be influenced by the blade rotation, though a uniformity is present across the span. Close agreement is observed between all CFS's tested.

Station 5 tangential flow angle is more heavily influenced by the splitter and part-span shroud. The overall distribution of the tangential flow angle has a backward lean, with increased angle near the root and reduced near the tip (this correlates well with the blade loading distribution shown later in Figure 4.7). This is required to maintain constant near-work input across the blade span, requiring more turning at lower radii. The splitter and part-span shroud cause a sharp rise in the tangential flow angle, with the effects from the part-span shroud perturbating further radially outward. Close agreement is observed between all CFS's tested.

The radial flow angles (Figure 4.3-right) at Station 4 are nearly exclusively positive, indicating radially outward flow toward the blade tip. This is strongest near the spinner, where flow is navigating around the cone and moving into the annulus portion of the engine. The radial flow angle magnitude decreases with increasing blade span as this

radially outward momentum is dissipated through the remainder of the flowfield. A sharp rise in radial flow angle at the tip is likely due to the clearance between the casing and blade tip, causing a static pressure gradient that forces flow outward toward the case, an effect supported in the Station 5 static pressure distribution of Figure 4.2-right. Although the majority of the data shows close agreement between CFS's, there is a higher discrepancy for transonic conditions radially outward from the part-span shroud, although the tip-most data point shows closer agreement.

The radial flow magnitude at Station 5 is reduced from that at Station 4. Core flow is on average exclusively axial, while the region directly above the splitter features a higher radial component, indicating flow moving out of the core and into the bypass. This effect is more pronounced at lower speeds, indicating a mismatch between the fan and core compressor at off-design conditions. Assuming the trend continues for increasing CFS, the design condition of the fan should reflect near zero radial flow at this location. The splitter and part-span shroud entrap the flow in a pocket of radial outward flow, before decreasing radially outward beyond the shroud, where it continually decreases before the sharp tip increase. Overall trends of both Station 4 and 5 for the radial flow angle show a backward lean distribution for increasing blade span, a trend that is disrupted at the tip.

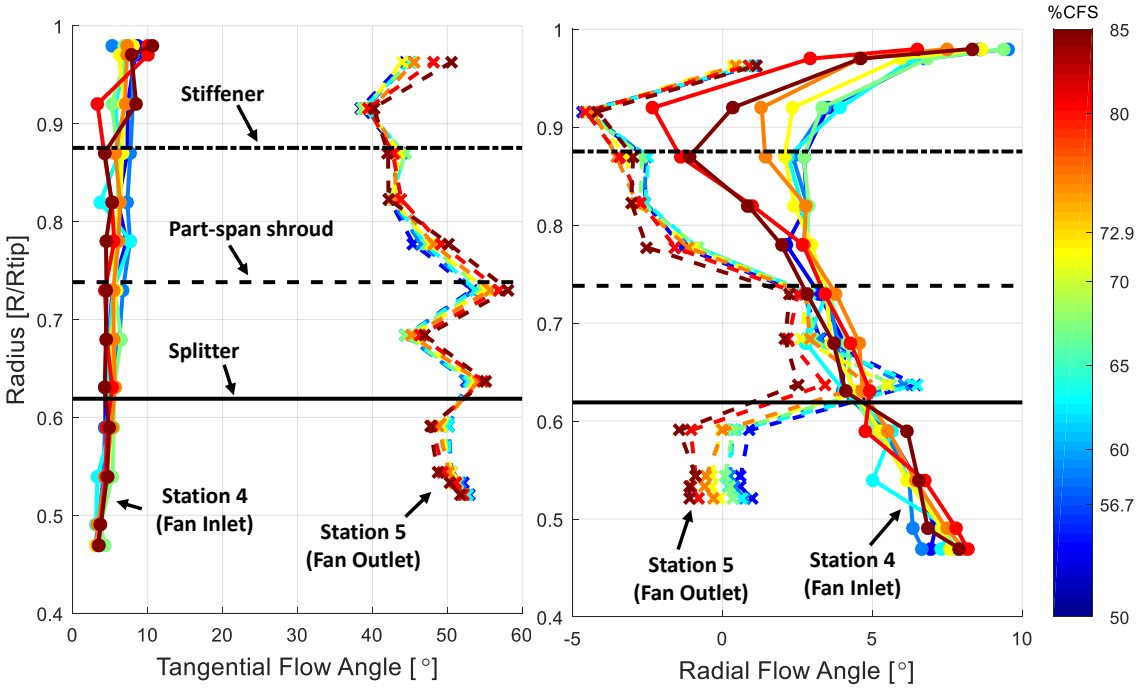

Figure 4.3. Undistorted tangential (left) and radial (right) flow angles

4.2.2.3 Total Temperature

The total temperature distribution is shown in Figure 4.4. Station 4 shows a constant inlet total temperature with the exception of the near-tip rise, which is more pronounced for higher CFS's. This will be shown later to be due to the reduced efficiency. Station 5 conditions show a similar trend to the total pressure of Figure 4.2-left, with increasing total

temperature with increasing blade span. The part-span shroud is the only portion of the blade geometry to significantly alter the distribution, producing a higher total temperature at the fan outlet in this region than the trend suggests.

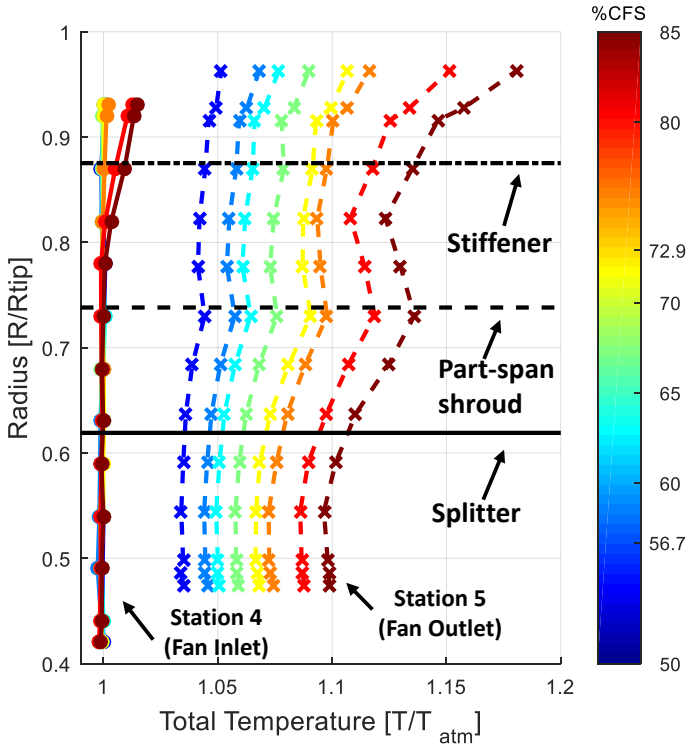

Figure 4.4. Undistorted total temperature span-wise distribution.

4.2.2.4 Velocity

The axial velocity (left) and velocity magnitude (right) span-wise distributions are shown in Figure 4.5. Close agreement of axial velocity between Stations 4 and 5 are shown at span locations below the part-span shroud, while large discrepancies exist radially outward. Both the splitter and part-span shroud cause severe axial velocity depreciations at Station 5. Axial velocity reductions at the tip are observed for transonic conditions, a consequence of the shock formation due to the high blade speed rotation rate.

The velocity magnitude distribution of Figure 4.5-right shows the accelerated flow profile from Station 4 to Station 5. Splitter effects at Station 5 are the primary engine geometry components that appear to affect the distribution, as both the stiffener and part-span shroud do not alter the distribution significantly.

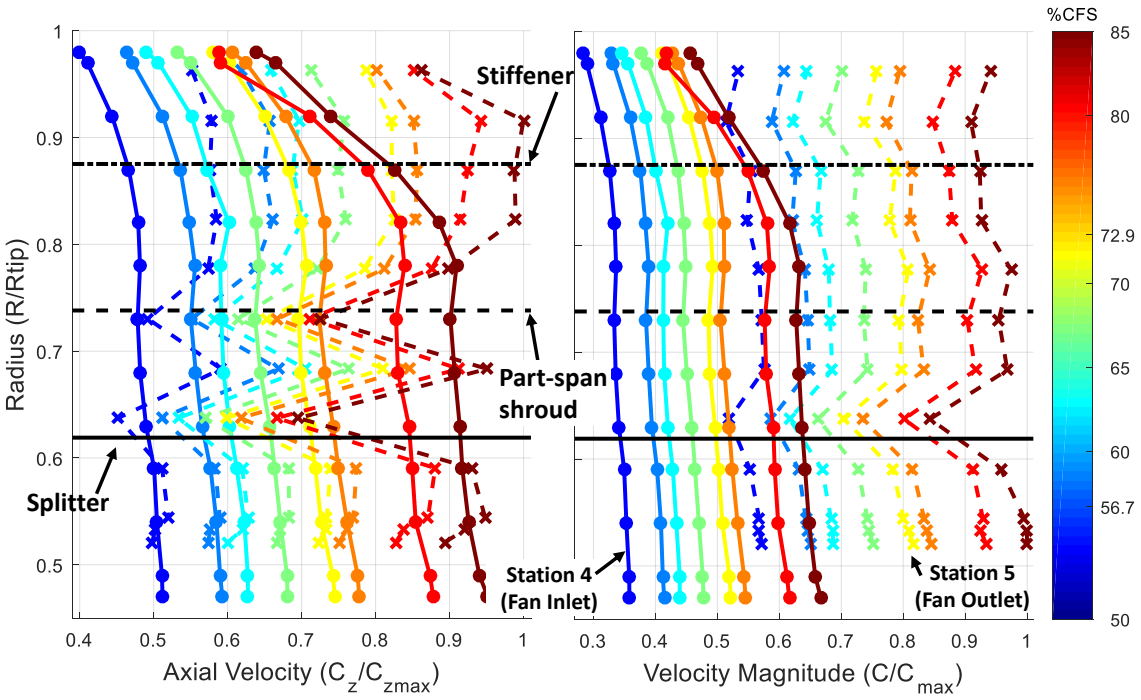

Figure 4.5. Undistorted axial (left) and velocity magnitude (right) span wise distributions

4.2.2.5 Incidence and Deviation

The fan blade incidence and deviation is shown in Figure 4.6. The results for Station 4 show a slightly varying positive incidence on the blades for all span locations measured with the exception of the tip, indicating the flow is directed more towards the pressure side of the blade than an optimal design would predict. Magnitude is shown to be speed dependent for radii below the blade stiffener. Station 5 shows a deviation of less than 5 degrees for the majority of the locations and speeds investigated. It is interesting that the near-splitter and shroud show a reduced deviation from the other measurements, with the splitter causing positive deviation, or overturning. Such an effect would not be possible in traditional cascade aerodynamics. The stiffener appears to not have affected the distribution. The results agree well with Carter's Rule, supporting a conclusion that the results are reasonable [22].

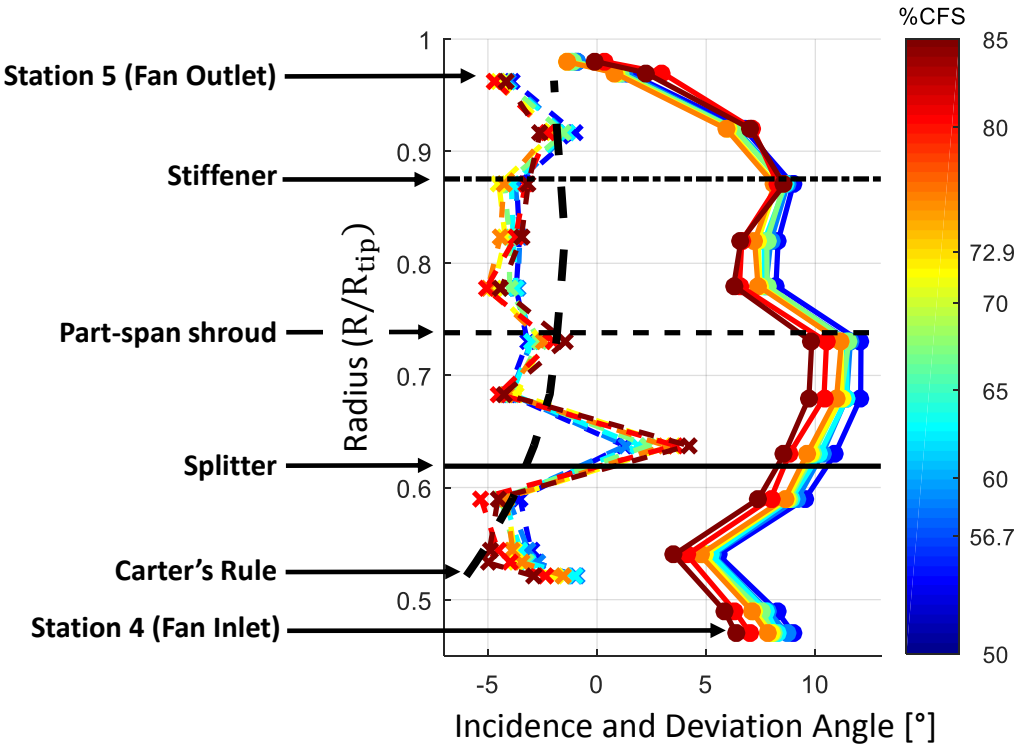

Figure 4.6. Undistorted incidence and deviation angle.

4.2.3 Fan Performance

The baseline undistorted fan performance metrics provided information on the design behavior of the engine. This was especially useful in validating the measurements as well as determining how the fan blade geometry affected such metrics.

4.2.3.1 Blade Loading ($\Delta C_\theta/U$) and Pressure Rise

The undistorted blade loading distribution is shown in Figure 4.7-left, with decreased loading for increasing blade span; a consequence of the near-constant work design input which requires more turning at lower blade span due to the lower blade speed. Details of the work input distribution are given in Appendix F. Close agreement between all speeds tested is observed. Differentiation from the linear backward lean trend is observed for the part-span shroud, causing increased loading at that location and the area radially outward from it. The stiffener and tip region also move the trend away from its close linear relationship, though less so than the shroud. This unloading at the blade tip was done to prevent separation [27]. The splitter appears to have negligible effect on the loading distribution.

The undistorted pressure rise distribution is shown in Figure 4.7-right with increasing sensitivity with blade span for increasing blade speed. Only the part-span shroud shows a significant alteration to the distribution, causing a reduction in the pressure rise, an effect observed across all fan speeds tested.

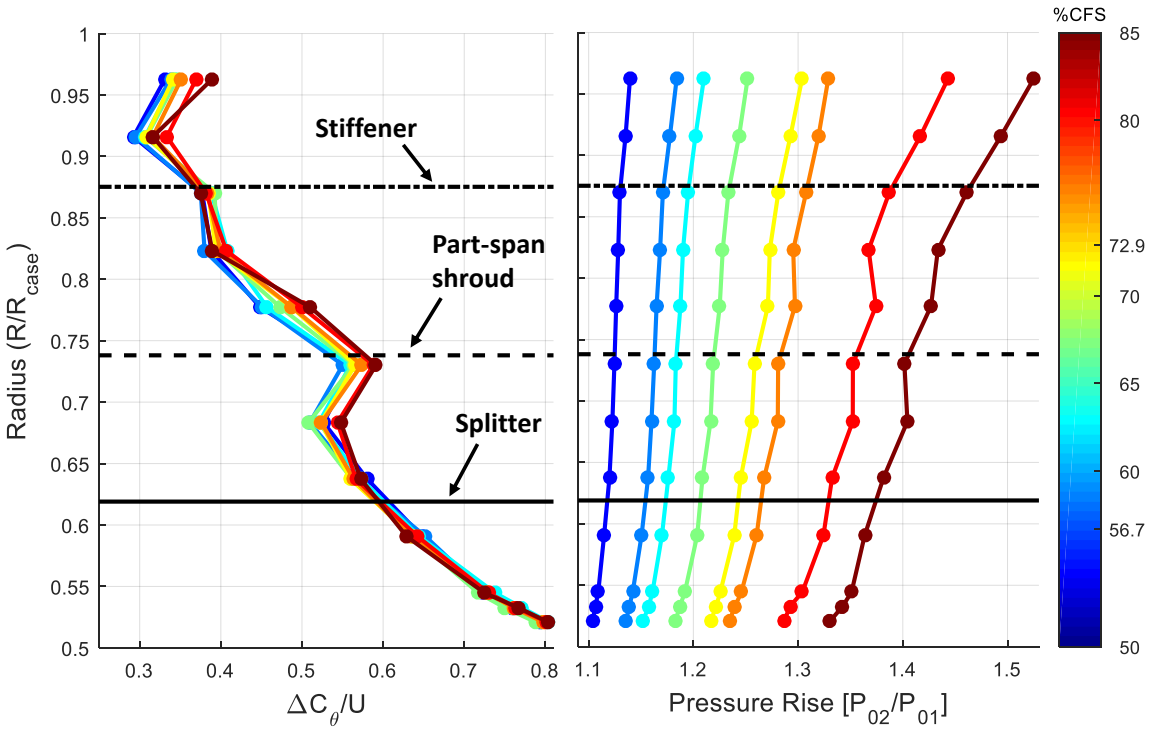

Figure 4.7. Undistorted blade loading (left) and pressure rise (right) blade span distributions.

4.2.3.2 Blade Loading Sensitivity

The blade loading calculation given in Equation (3.20) can be rearranged for the outlet absolute flow angle, α_5, and the inlet relative flow angle, β_4 as shown in Equation (4.2).

$$\frac{\Delta C_\theta}{U} = \frac{C_z}{U}(tan(\alpha_5) + tan(\beta_4)) - 1 \tag{4.2}$$

The fan blades are more sensitive to the inlet flow coefficient at higher radii due to the nature of the blade design. To maintain radially uniform work input, the turning required at higher radii is lessened due to the increased blade speed, U. The relative inlet flow angle (β_4) is increased as well for increased blade speed and is illustrated via the velocity triangles in Figure 4.8-right. As Figure 4.8-left shows, α_2 does not vary as strongly as β_1 nor is it monotonically increasing. Thus the proportionality constant to the inlet flow coefficient to Equation (4.2), C_Z/U, will correspondingly increase for increasing radii.

Reduced relative inlet flow angle is observed for increasing fan speed, a trend which extends from the core to the stiffener, before it is disrupted. Although the trend is consistent for the majority of the blade span, there remains close agreement between the measurements.

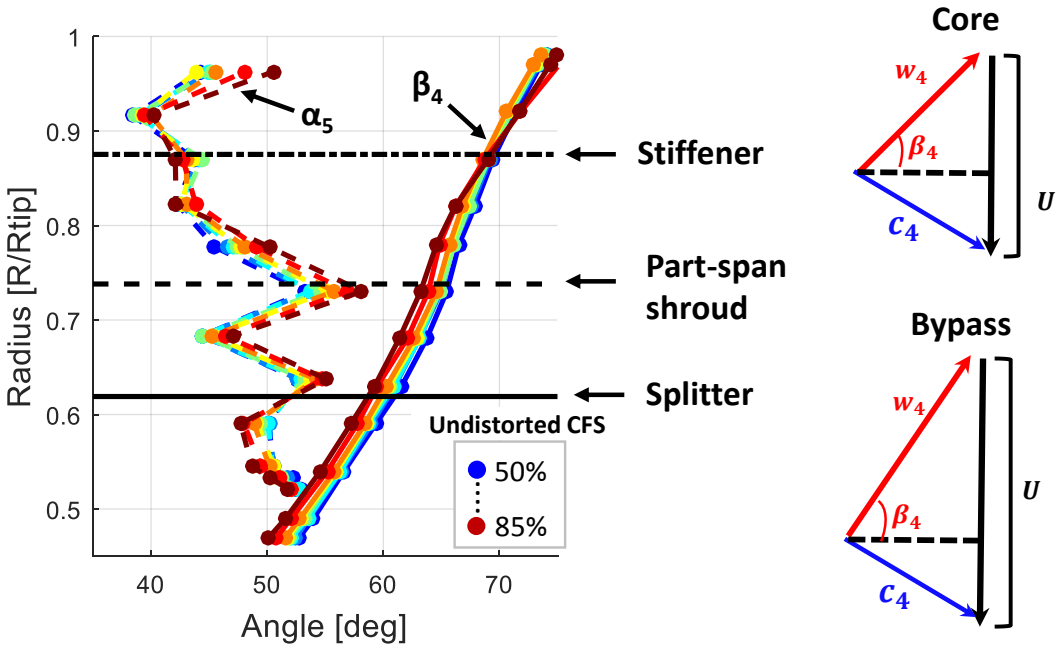

Figure 4.8. Outlet absolute flow angles (α_5) and inlet relative flow angles (β_4).

4.2.3.3 Diffusion and Efficiency

The Lieblein diffusion factor for the undistorted cases is shown in Figure 4.9-left, which follows a similar backward lean distribution as the blade loading observed in Figure 4.7-left; decreasing for higher blade spans. The diffusion shows a higher sensitivity to the engine geometry than the loading however, with noticeable shifts in the overall trend. Both the splitter and part-span shroud cause large increases in diffusion from expected values. The effects of the stiffener on diffusion are slight, less so than the tip effects. CFS appears to affect the severity of the diffusion depending on the location; reduced diffusion in the core for increasing CFS while the bypass shows increased LDF for increasing CFS. Without the splitter and shroud, the LDF should be below 0.5 for the entire bypass region, however these geometry components push the LDF close to 0.6 in both instances, and even higher for 85% CFS. The core LDF exceeds the recommended design limitation of 0.5, and along with the splitter and part-span shroud regions, are likely prematurely separating.

The efficiency distribution is shown in Figure 4.9-right, with magnitude strongly dependent on blade span. No coherent structure for the distribution is apparent, though close agreement is observed for the majority of the test cases investigated. The 85% CFS test case shows a higher diversion than the other speeds tested near the stiffener and tip region but follows closely with reduced speeds at lower blade span. The splitter appears to have negligible effects on the local efficiency, while the shroud and stiffener show reductions in the efficiency for regions near them, with very severe reductions observed for the shroud. The radial averaged efficiency of all speeds investigated is just under 80%.

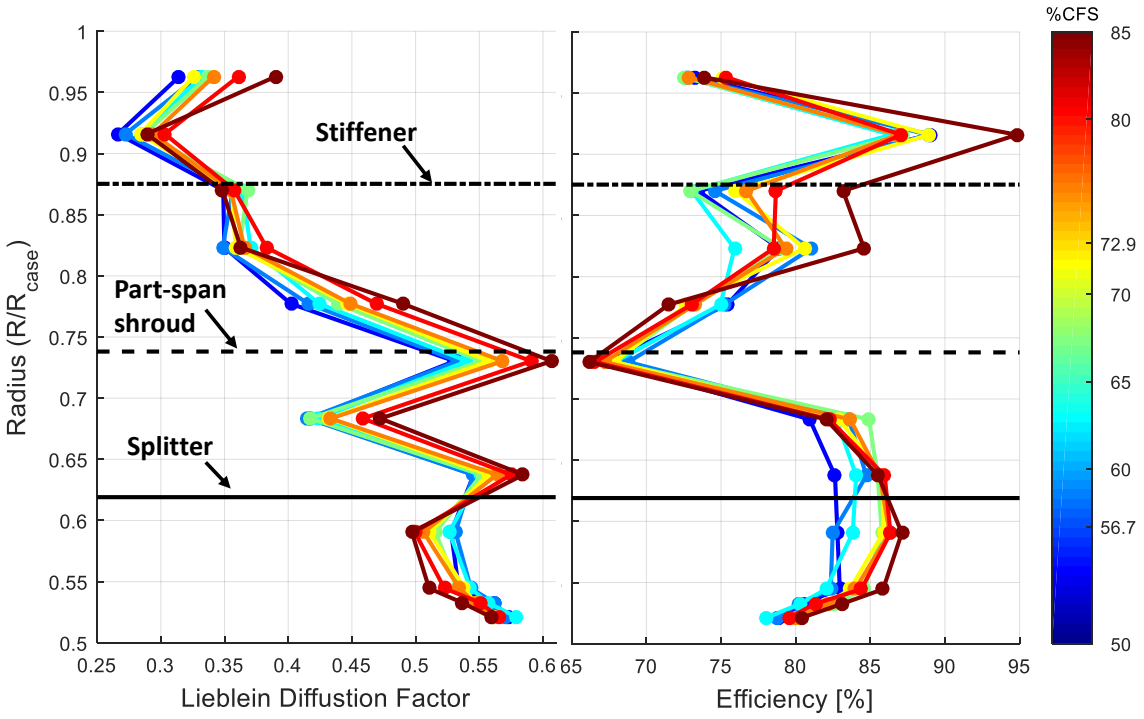

Figure 4.9. Undistorted diffusion (left) and efficiency (right) blade span distributions.

4.2.4 Summary

Fan inlet and fan outlet measurements were obtained for undistorted inlet conditions to serve as a baseline standard upon which to compare the distorted measurements. The inlet and outlet profiles allowed for the calculation of fan performance metrics that will be utilized in a similar way for the distorted tests. The data presented showed the impact the unique fan blade and engine geometry has on the radial distribution of the fan performance parameters and they will play a large role in the way the fan interacts with and responds to the distortion profile.

4.3 Distorted Inlet Flow Conditions

Distorted data was obtained for 60, 70, and 80% CFS and compared directly with the equivalent undistorted CFS. Unless otherwise stated, only the 70% CFS results will be presented in the body of this work. This was done for brevity as the majority of the profile features and parameters are consistent across speeds. Appendix G shows the results presented in Section 4.3 for all speeds investigated. On request, the full data set is available from the author. Recall that the distorted results are presented using the RDFU parameter defined in Equation (3.27) in most cases, with flow angularity and efficiency data presented as differences as calculated in Equation (3.28). This was done to remove the engine bias from the experiment and isolate the distortion effects.

4.3.1 AIP Inlet Profile

The total pressure profile measured at the AIP, representative of a BLI serpentine inlet, results in a distortion intensity more severe than probable inlet designs would employ. Figure 4.10 shows the intensities for all inlet speeds tested, with a minimum 91.5% recovery for 80% CFS. As can be seen, profile shape is preserved for each fan speed. The contour color schemas for the 60 and 70% CFS tests look identical to the 80% CFS when plotted on their relative scales. This is shown in Appendix G.

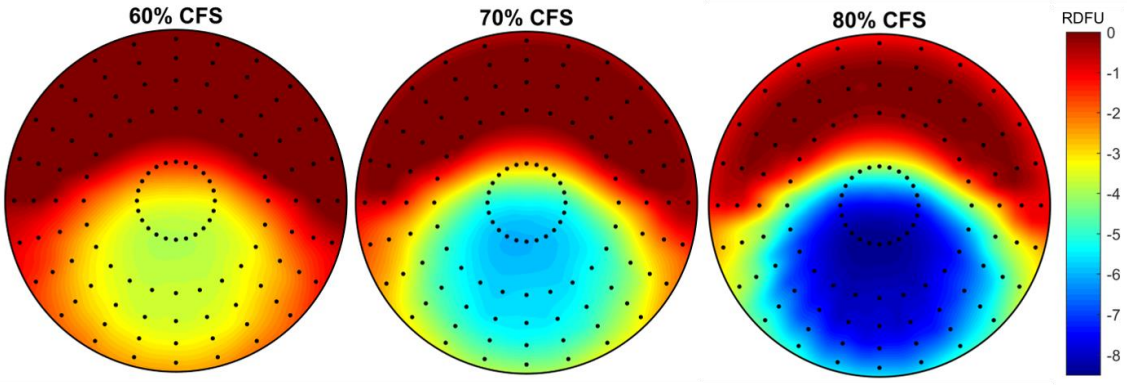

Figure 4.10. Distorted AIP total pressure profiles for the CFS's investigated.

The static pressure profile at the AIP exhibited similar characteristics between speeds, with the relative reduction in static pressure increasing in severity with increasing CFS, as shown in Figure 4.11. Minimum pressure occurs at BDC (180°), corresponding to that seen in the total pressure profile which is given to the right of Figure 4.11 as reference. Although the variation in static pressure is not nearly as significant as the total pressure, it is present and measureable, as Figure 4.11 shows. The systematic uncertainty of the measurements, u_{sys}, is shown within the figure for reference.

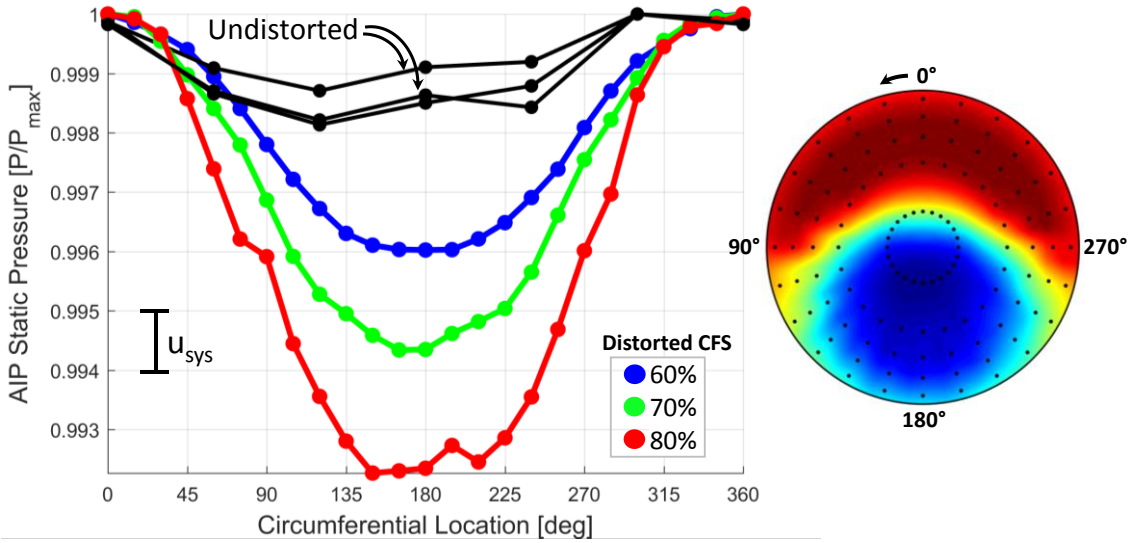

Figure 4.11. AIP static pressure results.

4.3.2 Station 4 and 5 - Fan Inlet and Fan Outlet Conditions

4.3.2.1 Total Pressure

The total pressure results for Station 4 and Station 5 are shown in Figure 4.12-left and Figure 4.12-right, respectively. The Station 4 total pressure profile is very similar to that measured at the AIP. A RMSD (Root Mean Square Difference) analysis between Station 4 and the projected Station 3 results onto Station 4 varies from 0.53% to 1.2%, for 60 to 80% CFS, respectively. RMSD is calculated using Equation (4.3), with N representing the data vector length and $\hat{\Psi}$ representing the data parameter of interest and Ψ the nominal value.

$$RMSD = \sqrt{\frac{1}{N}\sum_{k=1}^{N}\left(\hat{\Psi} - \Psi\right)^2} \tag{4.3}$$

This shows that not a significant amount of local or global total pressure variation occurs between these Stations, though there is evidence of mixing at the interfaces of the high and low total pressure regions (105° and 265°). A strong total pressure distortion is present at Station 5 and although not as extensive as at Station 4, it has increased in relative severity, causing significant losses to persist and exacerbate through the fan. The large, low total pressure pocket at Station 4 at BDC has been radially reduced and is limited to the core and splitter regions of Station 5. Some areas show an increased total pressure as a result of the distortion but they are limited, and a global average reduction of 4.3% from the undistorted case was calculated.

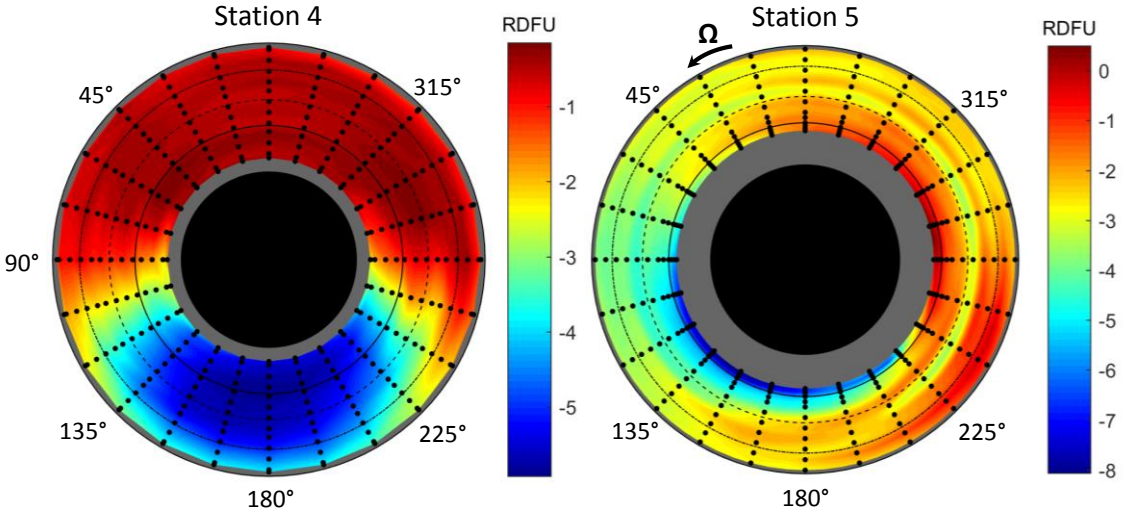

Figure 4.12. Distorted inlet (left) and outlet (right) total pressure profiles for 70% CFS.

4.3.2.2 Static Pressure

The static pressure non-uniformity becomes more prevalent at Station 4 than was observed at Station 3 (Figure 4.11), and is shown in Figure 4.13-left. An increase in the static pressure distortion develops as the profile approaches the fan, and is of nearly equal relative magnitude from the total pressure distortion of Figure 4.12-left. A noticeable asymmetry is also present, and interestingly it appears to have shifted the profile in the counter-fanwise direction. This static pressure distortion governs flow redistribution which will become clear in the flow angle and vector plots shown later.

Similar to the total pressure profile in Figure 4.12-right, the Station 5 static pressure results in Figure 4.13-right show the Station 4 non-uniformity entering the fan has been contracted radially and limited to the core. Acute regions of low and high static pressure variation still exist, particularly near the splitter and in the core flow regions. The entire flowfield exhibits a total reduction in static pressure from undistorted conditions of 4.9%.

Recall from Figure 4.11 that the static pressure variation at the AIP showed only a small variation, 0.7%, as compared to the 4.5% of Station 4. This indicates the high secondary flow variability is not present at the AIP, but quickly develops as the flow approaches the fan face.

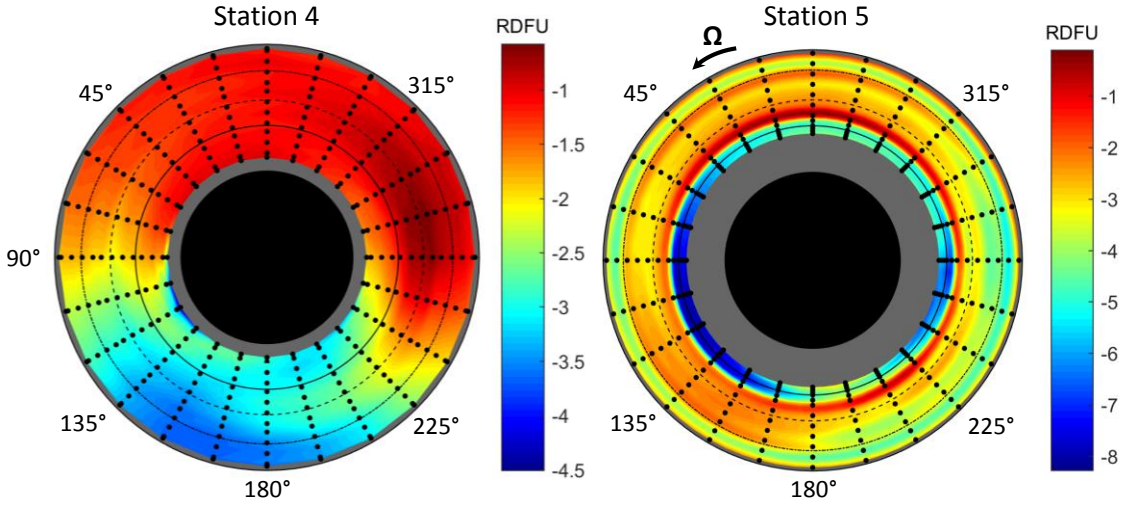

Figure 4.13. Distorted fan inlet (left) and outlet(right) static pressure profiles for 70% CFS.

4.3.2.3 Total Temperature

That total temperature profiles at Station 4 and Station 5 are shown in Figure 4.14. The differences between the distorted and undistorted conditions for station 4 (Figure 4.14-left) are negligible, varying approximately 0.3% across the profile. Station 5 (Figure 4.14-right) shows a larger variation, approximately 4%, with a distribution similar to that of the blade loading discussed later.

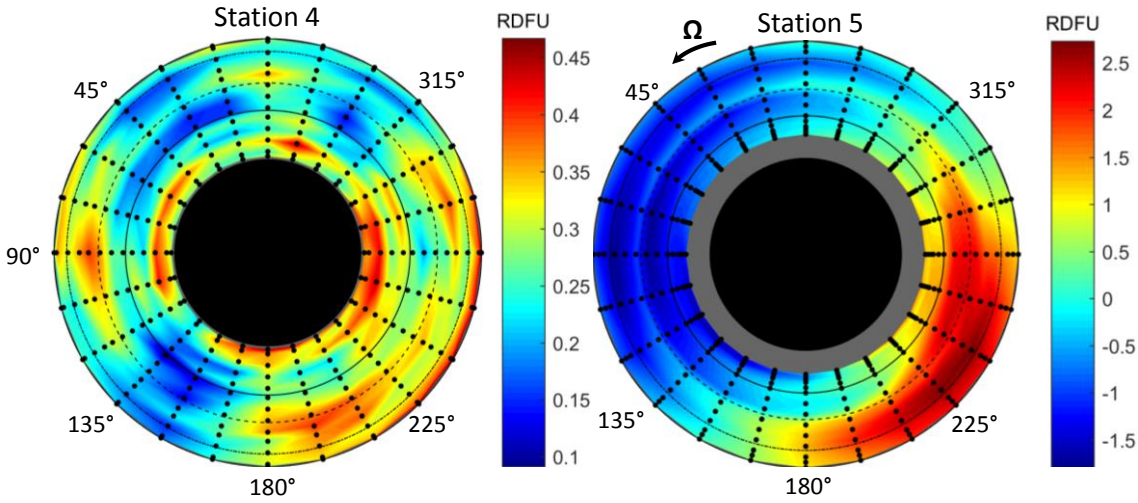

Figure 4.14. Distorted fan inlet (left) and fan outlet (right) total temperature profiles for 70% CFS.

4.3.2.4 Tangential Flow Angle

The tangential flow angle is shown in Figure 4.15. The redistribution of the flow driven by the static pressure deficit shown in Figure 4.13-left creates a substantial tangential flow angle variation that varies with both circumferential position and radius. Large co- and counter-swirl regions of significant intensity are present entering the fan. Larger tangential flow angles are present near the spinner, with reduced intensity radially outwards towards the tip. This radial gradient is stronger in the co-swirl region. The profile is slightly asymmetric with a larger counter-swirl region due to the higher static pressure on that side of the profile (see Figure 4.13-left). Co-swirl magnitude is higher due to spinner effects.

Station 5 of Figure 4.15-right shows transmission of the tangential flow angles through the fan. Higher flow turning with respect to undistorted conditions is seen exiting the co-swirl region and entering the counter-swirl region near BDC. Reduced turning is observed exiting the counter-swirl region starting near 240° for a large circumferential portion of the profile for the core flow region, where the significant turning required near the blade root has become too excessive. Banded regions around the profile show the effect of the blade and engine geometry (splitter, part-span shroud, and stiffener) appears to entrap flow exiting the fan. The shroud, specifically, appears to reduce the amount of turning produced by the blades at nearly all circumferential locations.

The tangential flow angle magnitude has been reduced while passing through the fan, but the fan outlet conditions still present severe flow angle variation that will reduce the efficiency of the stator vanes downstream, which are not in the proper orientation to efficiently turn this distorted fan outlet flow in the axial direction. This inefficiency will persist through the bypass duct, resulting in a system-wide reduction in operational efficiency.

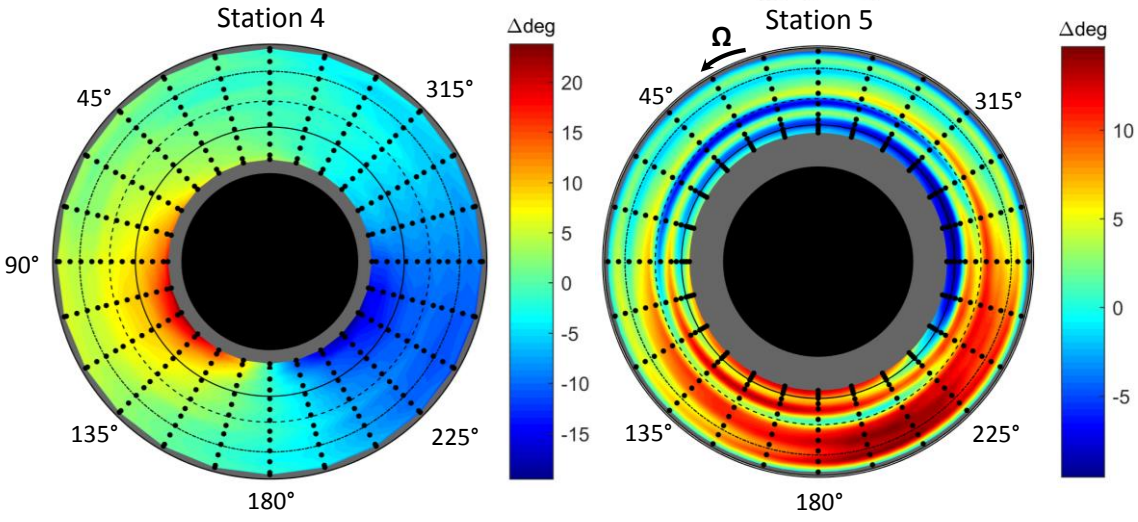

Figure 4.15. Distorted fan inlet (left) and fan outlet (right) tangential flow angles.

4.3.2.5 Radial Flow Angle

The radial flow angle, shown in Figure 4.16, is lower in magnitude than the tangential flow angle at Station 4 but increases in severity through the fan. At station 4 (Figure 4.16-left), the flow redistribution from the top of the profile to the bottom is shown with the high radially outward (positive) flow at the bottom of profile centered around 165°. This "sink point" is offset from BDC due to the non-axisymmetric static pressure distribution upstream of the fan that was shown in Figure 4.13-left, an interesting development considering the axisymmetric nature of the total pressure distortion entering the fan. Strong radially inward flow characteristics are shown in the right-half of the profile below the part-span shroud, centered at approximately 270°. This feature is also driven by the static pressure distribution which has a radial gradient in that region forcing flow radially inward.

Station 5 of Figure 4.16-right shows the radial flow distribution after traversing the fan. The majority of the flow does not contain a strong radial component, but a large circumferential band around the splitter radius shows a tendency toward radially inward flow. This is caused by the static pressure gradient around the splitter, creating strong radial flow migration into the core of the engine. This indicates that the core compressor is heavily influencing the distorted flow development. This thin band is the result of a radial contraction and circumferential spreading of the large radial inward flow on the right half of the Station 4 profile. The radial outward flow sink point from Station 4 has been circumferentially shifted approximately 70°, which can be calculated from Equation (4.4). Since the Ω/C_Z ratio is relatively constant for increasing fan speed, the angular displacement is independent of CFS.

$$\theta = \frac{\Omega}{C_z} * 2\pi * (z_5 - z_4) \tag{4.4}$$

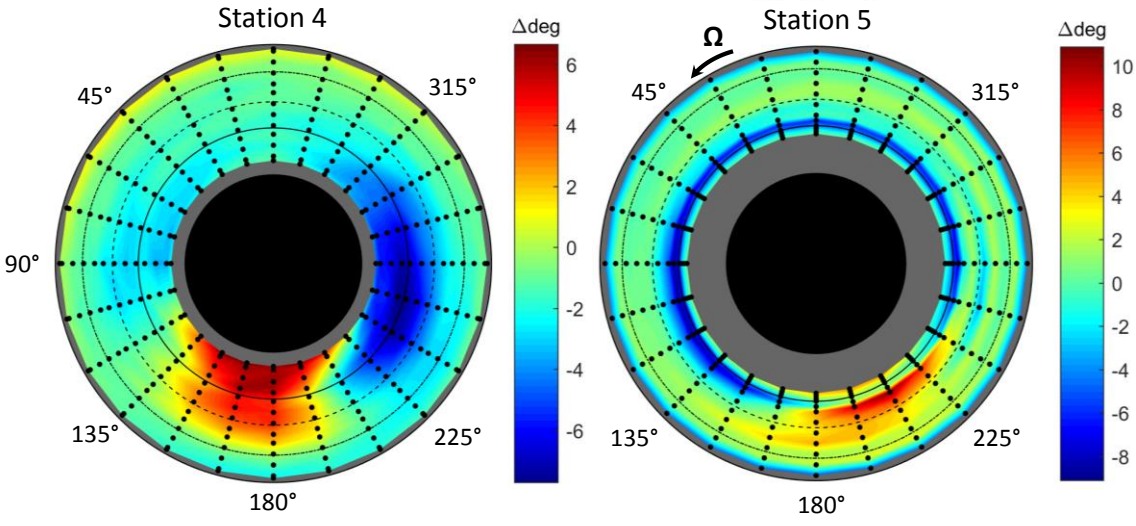

Figure 4.16. Distorted fan inlet (left) and fan outlet (right) radial flow angles for 70% CFS.

4.3.2.6 Upstream Flow Redistribution

Flow redistribution upstream of the fan face is the driving force for the high secondary flows measured at Station 4. The static pressure gradient created by the distortion results in the formation of large in-plane velocity components. This is best shown in the plots of Figure 4.17. Flow is redistributing from the high pressure regions in the top half of the profile, $270° > \theta < 90°$, to the lower pressure regions at the bottom of the profile, $90° < \theta < 270°$, creating high tangential flow angles at 90° (co-swirl) and 270° (counter-swirl) and high radial flow angles at 165° (tip-ward). The non-symmetric nature of the of the secondary flow profile is due to the offset, non-symmetric static pressure profile at the fan face, as shown in Figure 4.13. This effect is most clearly seen in the sink point of Figure 4.17-right near 165°.

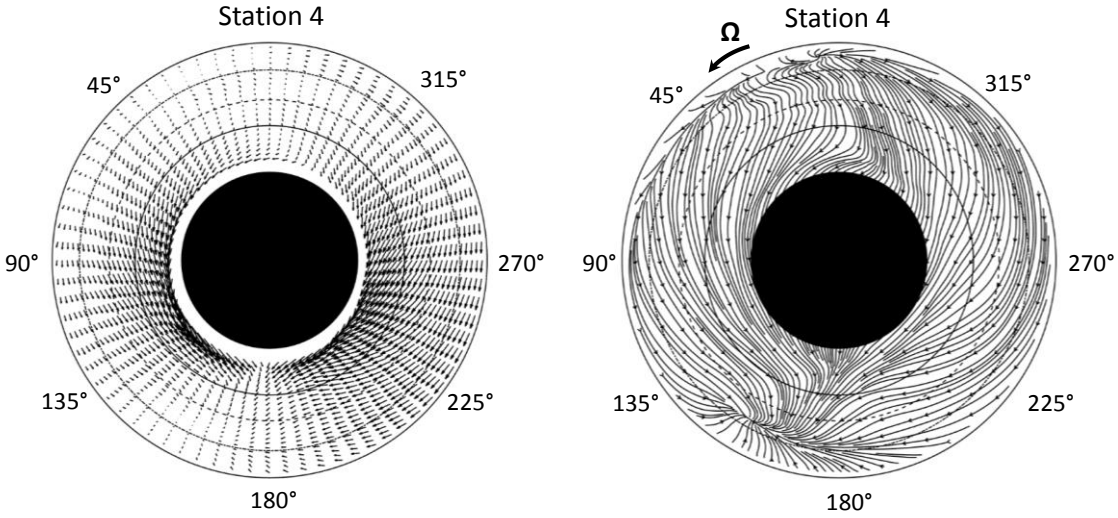

Figure 4.17. Distorted vector (left) and streamline (right) plots of the Station 4 in-plane velocity field at 70% CFS.

4.3.2.7 Incidence and Deviation

The change in incidence and deviation on the blades due to the distortion is shown in Figure 4.18, with incidence angle at Station 4 on the left and deviation angle at Station 5 on the right. The incidence is heavily influenced by the location of the total pressure deficit, but the approximate 30° fan-wise offset of the positive incident region centerline shows an increased sensitivity toward counter-swirl. Incidence is strongest when total pressure and counter swirl act in combination. Reduced incidence near the hub around 90° is in the area of strong co-swirl.

Figure 4.18-right shows a negative to positive deviation swing in the majority of the profile and most heavily in the co-swirl region, beginning in the core and moving radially outward to the part-span shroud. The bulk of the co-and counter-swirl inlet flow regions show increased and reduced deviation, respectively. Reduced deviation is shown for the majority of the core region, with overturning present at BDC at minimum total pressure and on the left-side of the profile within the bypass. Strong radial gradients are present due

to the fan blade and engine geometry which heavily influence the propagation of the distortion through the fan. The fan and engine geometry also tend to collect the flow into bands around the annulus.

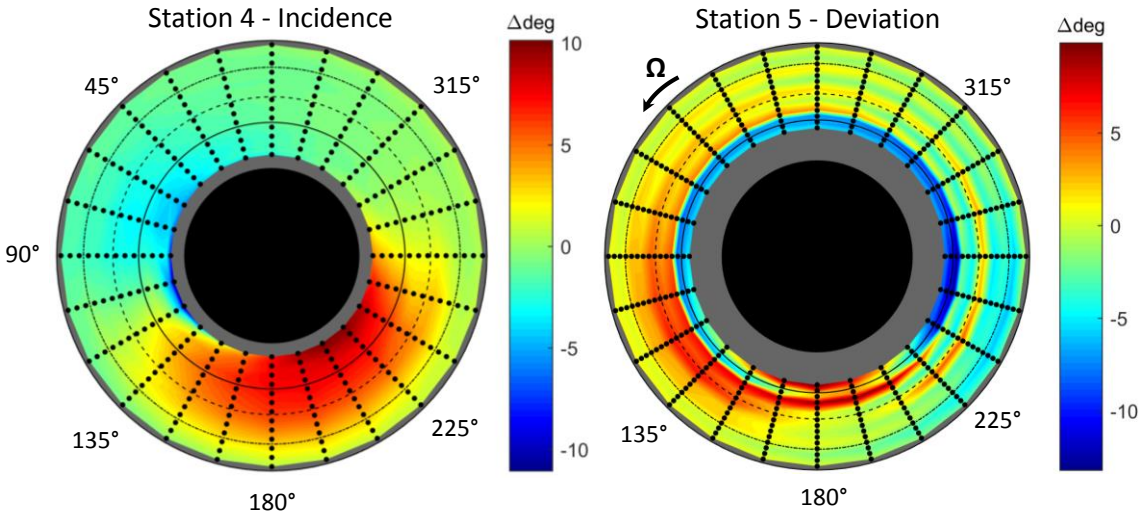

Figure 4.18. Changes in incidence (left) and deviation (right) angles relative to undistorted inlet conditions at 70% CFS.

4.3.3 Fan Performance

Due to the complex nature of the distortion profile, a non-uniform fan performance distribution was found for all fan performance metrics. Unless otherwise stated, figures are from the 70% CFS data sets as the profile distributions are independent of fan speed, though the ranges will vary. Performance metrics for all speeds are given in Appendix G.

4.3.3.1 Blade Loading ($\Delta C_\theta / U$) Distribution

The blade loading relative difference from undistorted conditions is shown in Figure 4.19-right, with the tangential inlet flow angle at Station 4 shown for reference in Figure 4.19-left. The loading shows a profile that is divided into two distinct circumferential regions, 345° < θ < 135° where the loading is largely reduced, and 135° < θ < 345° where the loading is largely increased, particularly radially tip-ward beyond the part-span shroud. There exists a blending between these regions, but this trend applies to the majority of the profile.

The reduced loading area is within the region of high and transitional total pressure, but also co-rotating tangential flow (co-swirl). The positive loading region of the profile is where the fan is exiting the low pressure region of the distortion and being subjected to increased pressure and increased counter-swirl. The increased counter-swirl will aim to increase the aerodynamic loading on the blades. The higher magnitude for more highly loaded blades indicates that the counter swirl more heavily influences the loading distribution, with a global increase of around 10%. The heavy loading also makes the

blades more susceptible to premature separation, which occurs in the 195° < θ < 285° region. This is supported in the Lieblein diffusion factor calculation presented in Section 4.3.3.5

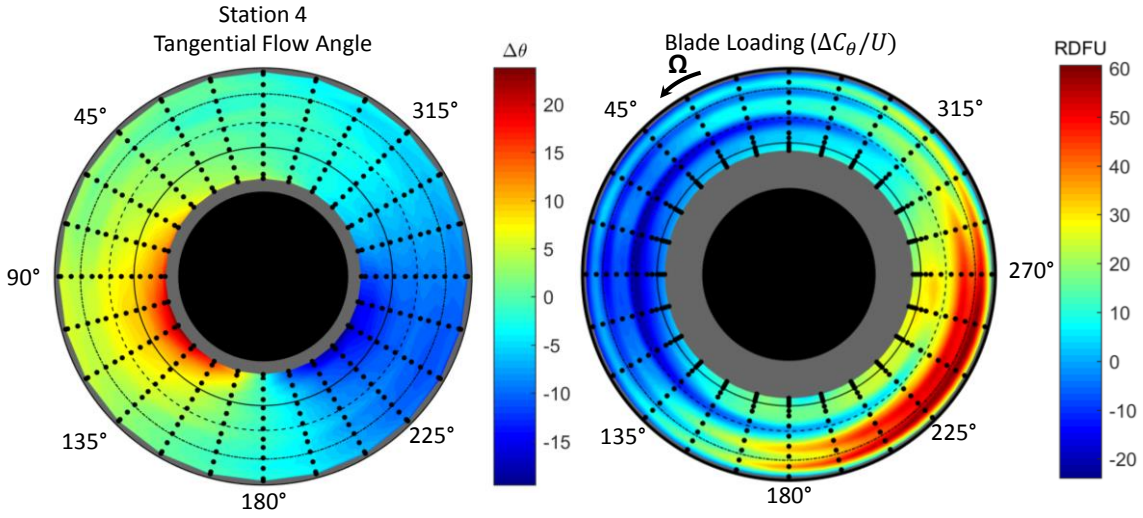

Figure 4.19. Station 4 tangential flow angle (left) and fan blade loading (right) at 70% CFS.

4.3.3.2 Blade Loading Orbits

Due to the non-uniform distribution of blade loading caused by the distortion, individual fan blade performance will vary as it completes a rotation. This is shown in Figure 4.20 where the distorted and undistorted blade loading relationships are plotted together. The loading structure as a function of axial inlet flow coefficient is shown in Figure 4.20-left, with good agreement between all three speeds tested. Data points are colored by circumferential position using the colorbar for reference on the far right of Figure 4.20 and the Station 4 total pressure distribution is shown for reference in the bottom right of Figure 4.20-left. Minimum inlet flow coefficient corresponds to 180° or BDC on the total pressure contour. The radial loading characteristic for the undistorted cases is plotted as a dashed line for 60, 70, and 80% CFS.

Orbital paths for sample core and bypass flows are plotted for simplicity, though the orbital relationships are preserved throughout the span – higher loading sensitivity for increasing radius. Note that the maximum loading occurs at approximately 240° for both the core and bypass radii, indicating that blade loading is more strongly influenced by tangential flow angle than inlet flow coefficient. Maximum loading also appears to be independent of radii, with all span-wise locations peaking at approximately the same circumferential locations. A typical behavior occurs at the part span shroud, as observed in the undistorted characteristic.

The orbital paths are plotted as function of the tangential inlet flow coefficient, normalized by axial inlet flow in Figure 4.20-right. The inlet swirl angle profile at Station 4 is plotted in the bottom right of the figure for reference. As shown, the maximum loading occurs at approximately 240°, the location of maximum counter-rotating swirl. Minimum

blade loading occurs at approximately 135°, the location of maximum co-rotating swirl. Orbit structure is preserved across the blade span, with increasing sensitivity for increasing radius, though much less aggressive than with inlet flow coefficient.

The lower the stage loading, the more likely the flow will remain attached to the blades and operate as efficiently as possible, with modern engines typically keeping the maximum blade loading to 0.75 [30]. While the undistorted profile shows blade loading values exceeding this maximum in the core, the distorted flow will have large circumferential regions that exceed this limit at higher span-wise locations. Also note the location of the undistorted operating point in relation to the orbits – on the lower spectrum of the blade loading orbital path. This means that the work input due to distortion is nearly exclusively higher in all areas of the profile and not limited to the undistorted region. Despite nearly half the distorted profile being of high recovery that could be considered 'undistorted', the loading is higher than the operating point for the majority of the fan rotation, indicating the full annulus effect of localized distortions and the inability of the fan to recover from distortions as severe as the one investigated in this work.

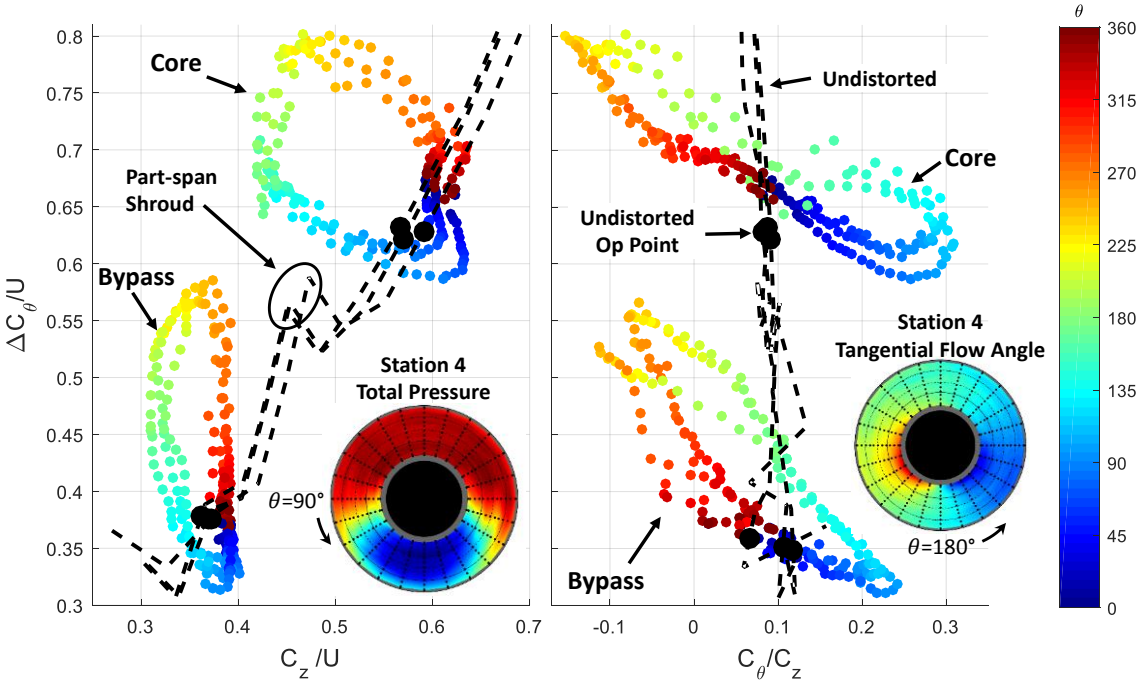

Figure 4.20. Blade loading as a function of inlet flow coefficient (left) and tangential inlet flow ratio (right) for distorted and undistorted conditions at all distorted CFS's.

4.3.3.3 Pressure Rise Distribution

The total pressure rise relative difference from undistorted conditions is shown in Figure 4.21-right, with the Station 4 inlet total pressure plotted for reference in Figure 4.21-left. The pressure rise distribution shows higher pressure rise in the lower pressure region of the distortion and a lower pressure rise in the higher pressure regions. It was shown in Figure 4.12-right that the total pressure uniformity at the fan exit will have greater significance for lower pressure fan inlet regions. The severely reduced pressure rise radially

inward from the part-span shroud at BDC is due to the low total pressure exiting the fan in that region, caused by both excessive diffusion (supported in Figure 4.23-left) and low axial inlet velocity. Note the rotated nature of the profile, approximately 15° in the fan-wise direction.

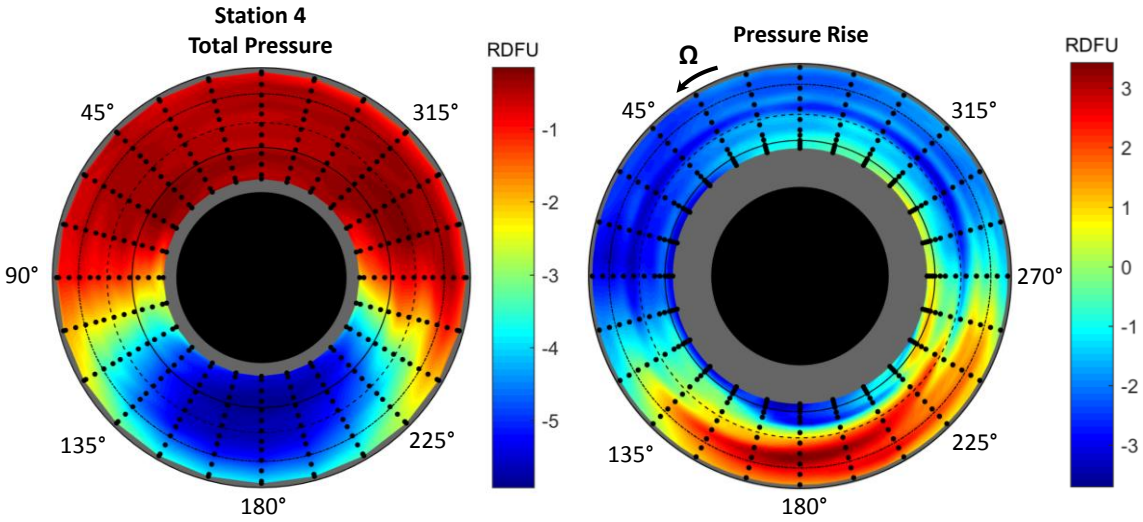

Figure 4.21. Station 4 total pressure (left) and total pressure rise RDFU (right) at 70% CFS.

4.3.3.4 Pressure Rise Orbits

Total pressure rise orbits are plotted as functions of axial and tangential inlet flow coefficients in Figure 4.22-left and Figure 4.22-right, respectively, for all three distortion speeds tested. The black dashed line is the undistorted conditions across the blade span with the circular black markers indicating the undistorted fan speed operation point and the diamond markers indicating the equivalent mass flow conditions for 70% CFS. As shown, orbital structure is preserved for each speed but the range is increased and shifted for higher output values. Well behaved orbits can be seen in the core region, with maximum pressure rise occurring at approximately 255°. Minimum pressure rise occurs at approximately 90° at the transition between high and low total pressure regions. The majority of the bypass flow has maximum pressure rises near the minimum inlet flow coefficients at approximately 180°. Minimum pressure rise occurs at the location of maximum pressure at TDC.

The discrepancy between the bypass and core maximum and minimum pressure rise locations is due to the significantly reduced outlet total pressure in the core, caused by increased flow separation as a result of excessive diffusion. This is supported by the LDF calculation (Equation (3.23) and shown in Section 4.3.3.5), which exceeds 0.65 in this region. Orbital structure variation between the core and bypass is due to the increased fan speed at higher radii, where the relative difference between the axial inlet flow and fan speed is increased and the pressure rise characteristic is more sensitive to changes in inlet axial flow. Notice how the core orbits contain both the equivalent fan speed and equivalent

mass flow operating points while the bypass only contains the equivalent fan speed, which indicates the core has a wider performance range and more stable operation.

The pressure rise as a function of the inlet tangential flow ratio for the 70% CFS is shown in Figure 4.22-right. For the bypass orbit, maximum pressure rise occurs at the minimum tangential flow ratio, slightly before BDC at 180°. Maximum pressure rise in the core corresponds to the location of maximum counter-swirl, at approximately 255°. Minimum pressure rise for both core and bypass occurs at approximately 105°, corresponding to the location of maximum co-swirl.

The slope characteristic of the core flow orbit in Figure 4.22-left suggests small pressure rise sensitivity to inlet flow for highly loaded blades, while the slope characteristic in Figure 4.22-right suggests a more sensitive pressure rise distribution to inlet flow angles. An opposing relationship exists for the bypass region where a sharp sensitivity to inlet flow and a relaxed sensitivity to inlet flow angle. In summary: blade loading affects the pressure rise sensitivity to inlet flow coefficient and inlet flow angle.

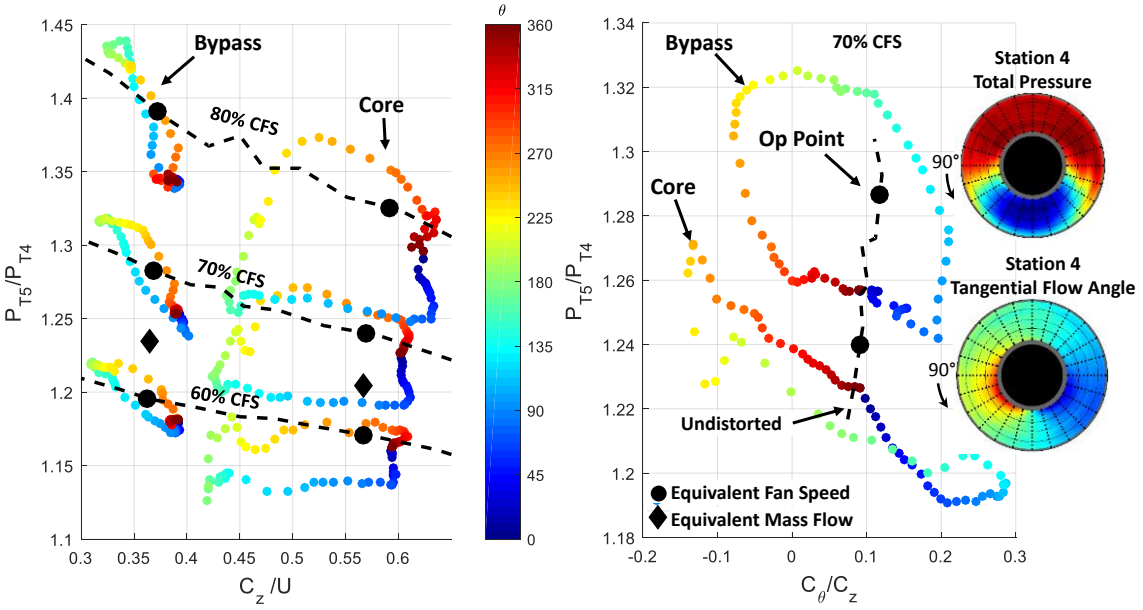

Figure 4.22. Total pressure rise as a function of inlet flow coefficient (left) and tangential inlet flow ratio (right) for distorted and undistorted conditions at multiple CFS's.

4.3.3.5 Diffusion and Efficiency

The Lieblein diffusion factor distribution, calculated using Equation (3.23), is shown in Figure 4.23-left, displaying a similar distribution to the blade loading profile of Figure 4.19-left. Higher LDF's are found in the core region where blade turning is more aggressive. Figure 4.23-left shows the overall LDF to be excessively high in the more heavily loaded regions, far beyond the 0.5 recommended value for non-separated flow [29]. This suggests the flow is separated in this region, but lower LDF elsewhere in the profile help offset the separation and allow the blades to recover and avoid initiating a rotating stall phenomena and potentially fan surge. The difference in LDF from undistorted conditions results in a localized decrease of 0.05 in limited areas to large area decreases up

to 0.4. The near entirely positive difference between conditions indicates that there is little relaxation in diffusion across the rotor due to distortion. Even the high recovery region near TDC of the total pressure profile results in small increases in the diffusion coefficient, creating a more aerodynamically difficult environment nearly everywhere in the profile despite the limited extent of the distortion.

The local efficiency of the fan is calculated following Equation (3.22), utilizing the local measured total pressure rise, the inlet total temperature, and the work input to the rotor. Although efficiency calculations in turbomachinery applications have been shown to carry large uncertainties [20], the reported trends and behaviors of the present measurements still provide valuable information on fan performance, as shown in Figure 4.23-right. Low efficiency values as a result of the counter-swirl is shown within the majority of the bypass region for areas of high counter-swirl ($180° < \theta < 345°$). High efficiency values were obtained between the splitter and part-span shroud ($315° < \theta < 150°$), as well as above and below the stiffener ($45° < \theta < 135°$). These blade geometry components appear to entrap efficiency values circumferentially, creating bands of consistent performance within the annulus. Efficiency characteristics are largely dependent on the inlet tangential flow angle; increased efficiency in co-swirl regions, $45° < \theta < 165°$, and reduced efficiency in counter-swirl regions, $195° < \theta < 315°$. The efficiency difference compared to undistorted conditions ranges from a reduction of 30% to an increase in 15%, with a distribution nearly identical to that shown in Figure 4.23-right, with a global reduction of 8.5%.

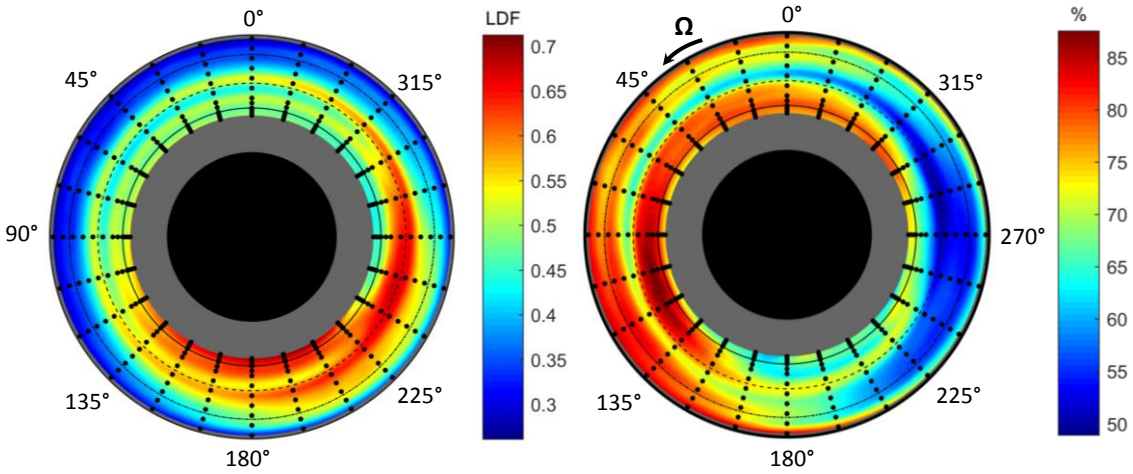

Figure 4.23. Local Lieblein diffusion factor (left) and local efficiency (right) under distorted conditions at 70% CFS.

4.3.3.6 Compressor Map

A simulated performance map of the fan can be constructed utilizing the experimental data collected. Although the mass flow was not varied for the fan speeds under investigation, the mass flux can be used to simulate such a procedure. Figure 4.24-left shows the pressure rise characteristic as a function of the mass flux, where the distorted conditions are shown in colored markers and the undistorted in colored lines overlaid with

black markers. The colors correspond to CFS as shown in the colored label on the far right of the figure. The distorted pressure rise - mass flux characteristic follows orbital paths like that shown in Figure 4.22-left for each radial location along the blade span, increasing in pressure rise for increasing blade span.

To obtain a single characteristic line typically used for compressor maps, the distorted condition had to be averaged in two ways. The first incorporated a radial average, where all the data at each circumferential location was averaged at each radial measurement location across the blade span, resulting in a single pressure rise orbit, as shown in Figure 4.24-right. The final characteristic was obtained by sorting the radially averaged data for increasing mass flux and performing a two-point moving average, given in Equation (4.5) and results shown in Figure 4.25-left. For Equation (4.5), Y is the radially averaged data set, Z is the two-point moving average, N is the number of data points, and k is the mass flux sorted index in data set Y.

$$Z_{k-1} = \frac{1}{2}(Y_k + Y_{k-1}) \text{ , } for\ k = 2{:}N \tag{4.5}$$

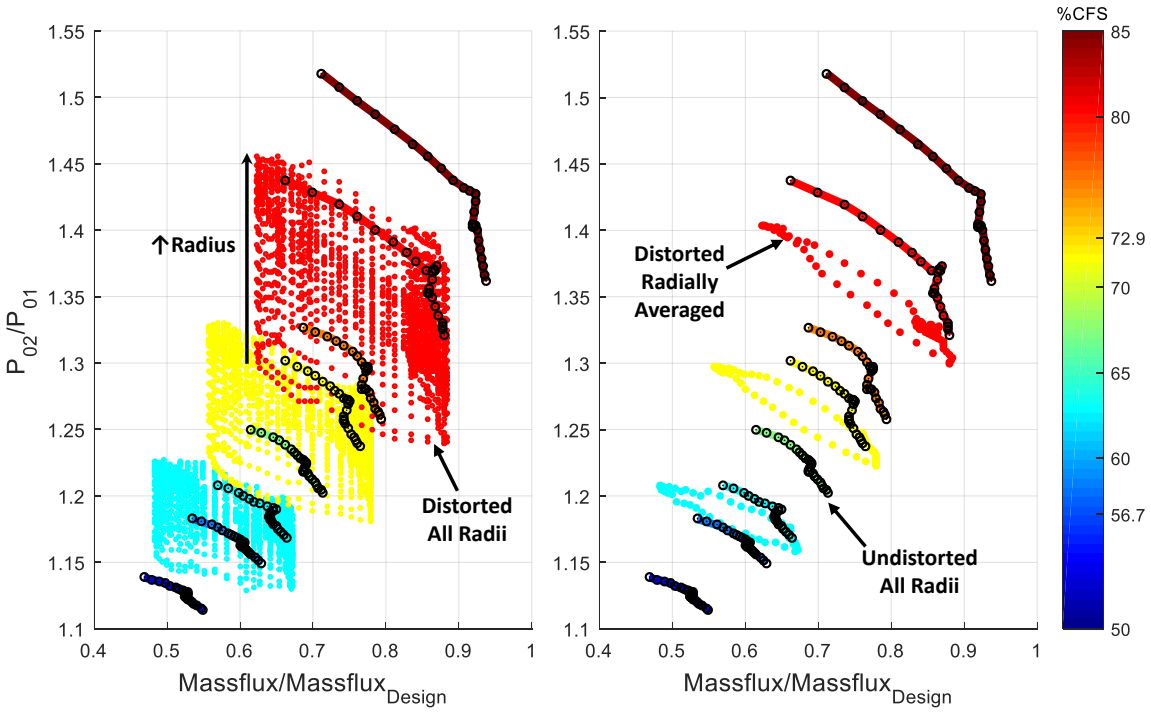

Figure 4.24. Pressure rise – mass flux characteristic, all radii (left) and radially averaged distorted conditions (right).

While the shape of the lines do not replicate expected characteristic curves like Figure 4.25-right, they do indicate the reduced performance expected from distortion and its relation to undistorted performance. If we recall from Figure 1.2, the distortion is expected to reduce the performance of the compressor for a given speed, and this reduction increases as design conditions are approached [7]. The results from Figure 4.25-left show the reduced

performance values, most specifically in the bypass region of the fan. The data from this investigation shows that the pressure characteristic for the distortion lies approximately midway between undistorted performance for equivalent fan speed (above the distortion line) and equivalent mass flow (below the distortion line). This relationship can then be subsequently used to estimate what overcompensated fan operating conditions are required to obtain the design condition performance in the presence of distortion, until the onset of stall.

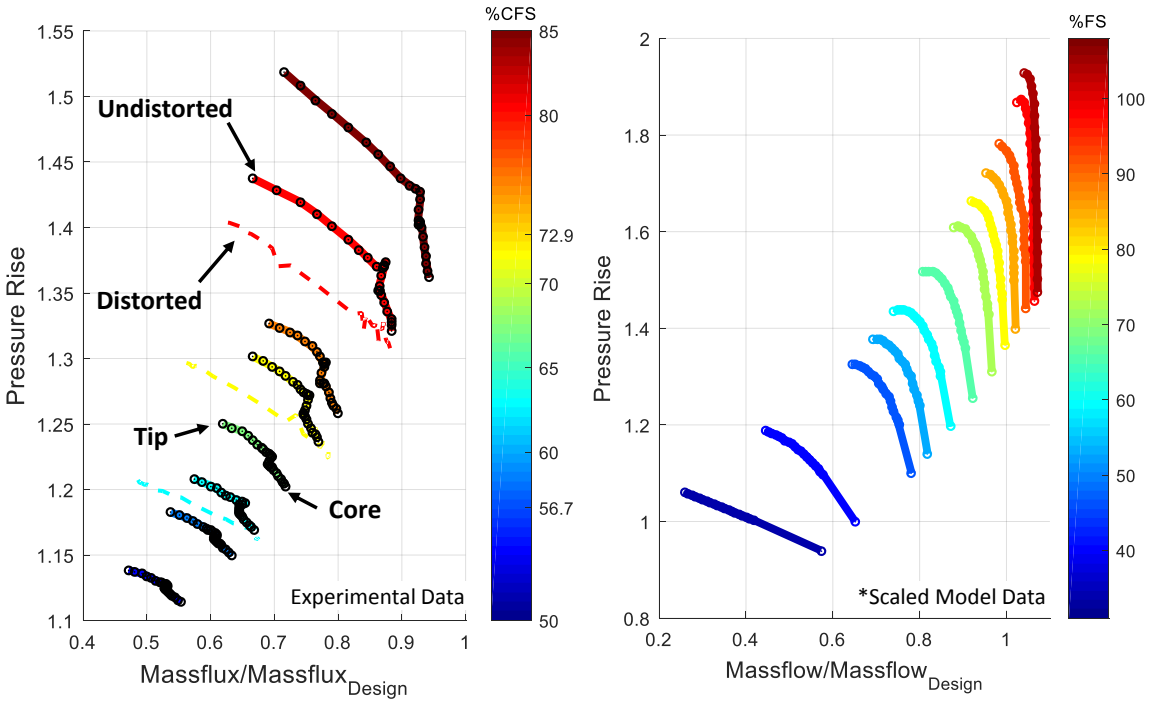

Figure 4.25. Simulated compressor map (left) and scaled model data for the JT15D-1 (right).

4.3.4 Summary

The results presented in previous sections show the impact of total pressure distortion on fan performance for several engine speeds. The reduced axial velocity upstream of the fan caused by the pressure deficit creates varying inlet conditions integral to fan performance. The result of this pressure deficit produced by the distortion screen results in downstream flow redistribution that creates significantly high tangential and radial flow variations. This secondary flowfield distribution produces varying fan performance profiles, whose trends are governed heavily by the total pressure and tangential inlet flow characteristics, as well as the design blade loading distribution.

Global fan performance calculations due to distortion are shown in relation to undistorted equivalent conditions in Table 4.1 The global average pressure ratio lies between the undistorted equivalent fan speed and equivalent mass flow cases (see Section

2.1.2 and Figure 2.7 for reference), while the global averaged blade loading and efficiency show an average 8.5% increase and a 11% reduction, respectively.

Table 4.1. Global performance parameters for distorted and undistorted cases.

	Fan Speed	Undistorted Equivalent Fan Speed	Distorted	Undistorted Equivalent Mass flow
Pressure Ratio	60	1.19	1.18	1.17
	70	1.27	1.26	1.22
	80	1.37	1.35	1.29
Blade Loading	60	0.47	0.51	0.46
	70	0.47	0.52	0.47
	80	0.49	0.52	0.48
Efficiency [%]	60	78	69	79
	70	79	70	79
	80	79	73	79

Plots of local performance parameters as a function of circumferential position for select core and bypass radii are shown in Figure 4.26, along with the inlet total pressure (1st row) and the tangential inlet flow angle (2nd row) for reference. This plot configuration shows the variation of the performance metrics as the fan rotates through key distortion features. The undistorted equivalent fan speed metric or reference is shown in the dashed blue line and the distorted parameter is shown in red.

Pressure rise (3rd row) follows an atypical trend for the core flow, showing a closer matching with the tangential inlet flow angle than the inlet total pressure. The bypass shows a more expected trend, with the pressure rise inversely related to the inlet total pressure for as long as the flow can remain attached.

Blade loading trends exclusively with tangential flow angle, decreasing in regions of co-rotating swirl and increasing in areas of counter-rotating swirl. Despite the relatively equal magnitude of the tangential flow angles, unequal magnitudes of the blade loading result from the distortion that is heavily biased to increased loading, which precedes the directional change of the flow angle by approximately 30° for both core and bypass regions.

Efficiency in the core appears to be largely unaffected by the trends of the inlet total pressure and tangential flow angle. The bypass region tracks well with the tangential flow angle, increasing for co-swirl and decreasing for counter-swirl. Both core and bypass regions show significant overall reductions in fan efficiency.

The Lieblein diffusion factor is inversely proportional to inlet total pressure, a consequence of its dependence on the relative inlet flow angle to the blades which is directly tied to the inlet axial velocity. Lower axial velocity will tend the blades toward positive stall, increasing the relative velocity to a larger percentage of the blade speed, increasing the diffusion factor and reducing the blade stall margin. The bypass distribution favors the counter-swirl region, with peak values obtained at approximately 225°, corresponding to the peak in blade loading.

A few final notes referring to Figure 4.26 show the full annulus impact of the distortion profile. Due to the severity and three dimensional nature of the distortion, a recovery point is never achieved for any of the fan performance parameters investigated. There are very few points in the fan performance profiles that can be considered 'settle points', where performance settles back to undistorted equivalent fan speed conditions. Blade loading and the diffusion factor are two exceptions, while the primary performance metric of fans, total pressure ratio, is constantly varying through a revolution. Also, the loading and diffusion are nearly exclusively increased and decreased as a result of the distortion. While the pressure rise metric may be higher in some areas, this is a deceptive result as the efficiency and amount of work is reduced and increased, respectively.

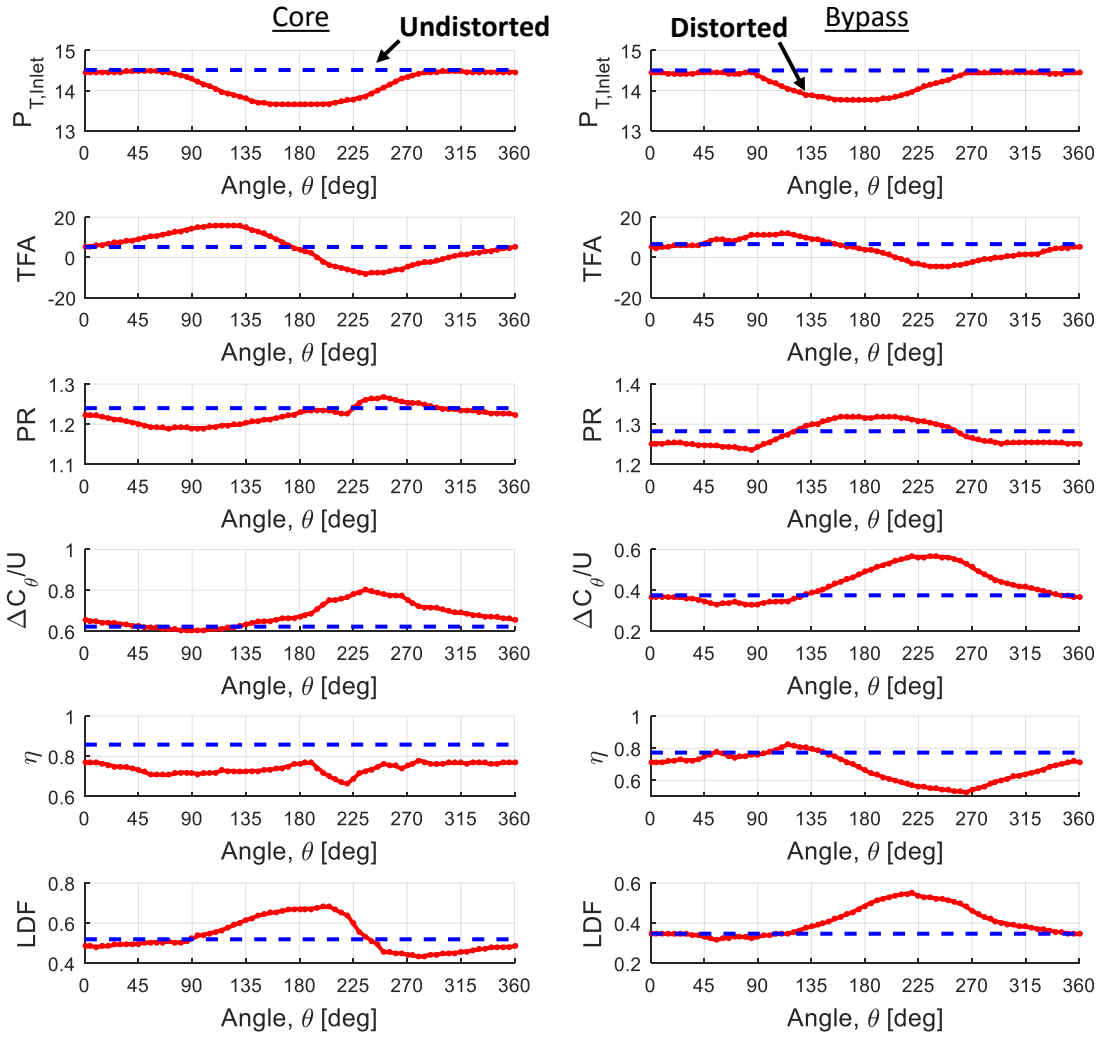

Figure 4.26. Distorted and undistorted performance parameters trends for core and bypass flow

Table 4.2 summarizes the fan performance metrics for measured inlet profiles, and corrected-uncorrected outlet conditions as defined in Section 3.7.1. The bulk of the results

presented were for both measured fan inlet profiles and corrected fan outlet conditions. The purpose of this table is to show the importance of measuring the fan inlet conditions such that accurate fan performance metrics can be calculated. Contour plots of the different parameter calculations were not plotted due to their strong similarity in shape to the corrected and inlet measured case. However, the data values varied significantly, especially for the 'Unmeasured Inlet' conditions where the fan inlet profile was not measured.

As shown in Table 4.2, the pressure ratio variation between cases is negligible, as the pressure difference between Station 3 and Station 4 is very small, only 0.53% at 60% CFS and 1.2% at 80% CFS. Due to the high circumferential extent of the pressure distortion at Station 4 and Station 5, there is insignificant mismatching between fan inlet to fan outlet comparisons, thus the global pressure ratios are similar.

Blade loading and efficiency, which are both heavily dependent on the inlet tangential flow angle, show strong discrepancies between measured and unmeasured fan inlet profiles. Relative differences between the calculated parameters are approximately 8% for blade loading and 7% for efficiency, of nearly equal value as the distorted effect being investigated. The discrepancies between loading and efficiency are not strongly dependent on fan speed. These results emphasize the importance of measuring the inlet flow profiles in order to calculate accurate performance results, otherwise the effects of distortion can be exaggerated.

Table 4.2. Fan performance parameter comparisons between corrected outlet conditions and unmeasured fan inlet.

Fan Speed	Parameter	Corrected Outlet Measured Inlet	Uncorrected Outlet Measured Inlet	Uncorrected Outlet Unmeasured Inlet
60	Pressure Ratio	1.18	1.18	1.18
	Blade Loading	0.51	0.51	0.55
	Efficiency	69	70	65
70	Pressure Ratio	1.26	1.26	1.26
	Blade Loading	0.52	0.52	0.55
	Efficiency	70	71	65
80	Pressure Ratio	1.35	1.34	1.35
	Blade Loading	0.52	0.53	0.56
	Efficiency	73	71	66

Chapter 5 Conclusions and Recommendations

This dissertation presented a full scale experimental study on the effects of total pressure inlet distortion on fan performance. A total pressure distortion representative of a boundary layer ingesting serpentine inlet was introduced upstream of a modified Pratt and Whitney Canada JT15D-1 turbofan engine. Using a calibrated 5-hole probe, flow parameters necessary to characterize the fan inlet and fan outlet flowfields were measured and results calculated. The results presented in this dissertation have highlighted the necessity of the extensive testing procedures required to accurately determine the effect total pressure distortion has on fan performance. Using the measurements and analyses previously described, the following sections summarize the conclusions obtained from this study as well as providing recommendations for future research and development.

5.1 Summary

Principal conclusions associated with the following discussions are shown in italics. These conclusions will be summarized and collected at the end of this section.

5.1.1 Full Flowfield Measurements

The automated traverse system utilized in this experiment allowed data to be taken quickly and repeatedly. The fine radial and circumferential control enabled dense measurement grids to be obtained for all test cases investigated. Without this capability, full flowfield measurements would not have been possible and a sparse measurement grid would have been insufficient to locally characterize blade performance. This dense measurement grid allowed sufficient data to be collected to characterize the full flow field, such that linear interpolations between data points could be accurately made. This enabled accurate determination of the distortion effect distribution and global characterization.

The results presented show the full annulus effect of the distortion despite its limited circumferential extent. This non-symmetric circumferential variation required a fine circumferential grid to accurately measure the distortion changes as the fan passed through the distortion. *Fan blade and engine geometry characteristics thus require a fine radial grid in order to accurately capture bypass and core flow behavior*. The part-span shroud and blade stiffener significantly changed the fan performance and quantifying this required sufficient measurement density around both components.

Acceptable radial and circumferential density at the fan outlet also allowed for accurate determination of fan outlet angle distribution. Such information would be required for optimal design of outlet stator vanes for maximum stage efficiency.

5.1.2 Fan Inlet Profile

Total pressure distortion screens are typically calibrated in wind tunnel configurations in the absence of downstream turbomachinery where the distortion profile measured one diameter downstream of the screen plane is established as the fan inlet profile for future engine testing [7]. In this configuration flow angularity is so low as to be considered negligible. These screens are then placed in fan testing environments where the screen is located two diameters upstream of the fan inlet and the measured profile from the wind tunnel configurations is expected to hold true. While this has been shown to be a good assumption for lower speed flows in the case of total pressure, it is not a good assumption for higher speed flows [23] and ignores the considerable radial and tangential flow variation entering the fan.

Utilizing this AIP plane in screen calibration tests and assuming the measured profile is applicable to fan performance tests is inaccurate. Proper characterization of the fan inlet profile requires calibration in the performance testing configuration with full flowfield parameter measurements directly upstream of the fan. *Without this correct inlet profile, global work and efficiency calculations are exaggerated and local performance trends and relationships to the incoming profile are lost.* It was found in this research that the global pressure rise calculation was impartial to fan inlet measuring, but work and efficiency are strongly affected.

Fan inlet measurements also provide important detail of the distortion development, shown in this dissertation as the *substantial flow redistribution upstream of the fan that resulted in high tangential and radial flow components*. The secondary flow profiles produced by the screen were a result of the fan interaction with the distortion profile, creating a non-axisymmetric static pressure profile at the fan inlet and driving flow redistribution, creating non-axisymmetric tangential and radial flow variation. This off-centerline convergence point for the secondary flowfield was a result of the fan interaction as the total pressure distortion was axisymmetric. The spinner geometry also heavily influences the distortion development, particularly with core flow and co-swirl regions. The measured inlet profile will also allow for blade redesign, such that the optimal blade shape can be constructed that bests performs for the total pressure and secondary flow distortion it is subjected to.

5.1.3 Distortion Transfer

The results obtained at the fan outlet, Station 5, showed that *pressure and secondary flow variations persisted in the distortion profile.* While the *radial flow angle variation was mitigated* through the fan, *total pressure, static pressure, and tangential flow angles were exacerbated* in magnitude. The structure of the distortion was also significantly altered; flow phenomena entering the fan experienced large radial contractions and circumferential spreading. Much of the flow phenomena was banded in extrema regions due to the interaction of the distortion with the blade geometry; splitter, part-span shroud, and stiffener.

5.1.4 Distortion-Fan Interaction

Due to the coupled effect of the fan and distortion screen, the fan is acting as a driver of the distortion development in a way that varies from traditional wind tunnel screen calibration. Varying work input and non-uniform pressure outputs contribute to non-uniform inlet pressure profiles that drive flow redistribution further upstream of the fan inlet. This flow redistribution creates secondary flow characteristics that further complicate the distortion profile.

Since the fan and screen form a coupled system, the total and static pressure distortion as well as the resulting secondary flow effects become inseparable. Therefore, obtaining isolated total pressure effects on fan performance is not feasible, and *secondary flow effects cannot be decoupled from the total pressure distortion in traditional fan performance measurement configurations.*

5.1.5 Fan Performance Ground Tests

Fan speed was shown not to significantly vary the results for the parameters and measurements of interest in this investigation. *Trends and distributions of the fan behavior in varying regions of the distortion were preserved between speeds*. Thus, lower speed distortion tests can be performed to reduce cost and risk, while preserving the flow phenomena behavior for speeds up to the engine stall limit. The benefit of performing varying distortion speed measurements would be for estimation of fan performance in relation to the compressor map. A minimum of two distortion speed tests could be completed at reduced speed to obtain the operating line characteristic, allowing estimation of the distortion mass flow at varying engine speeds. The losses at each engine speed could then be estimated by averaging the undistorted equivalent fan speed and equivalent mass flow pressure rise. This estimation would be accurate at lower speeds, but unstable at near design conditions as the stall limit of the fan is rapidly approached as a consequence of the distortion.

5.1.6 Local Performance Calculations

This dissertation showed the radial and circumferential variations of fan performance as a result of the total pressure distortion. This was accomplished by having full inlet profile measurements to accurately calculate performance metrics. The strong association of blade loading and efficiency with inlet tangential flow angle, and the strong association between pressure rise and inlet total pressure could not have been determined without the fan inlet profile. The behavior of the fan at varying positions within the distortion could be determined and the sensitivity to each inlet flow parameter could be evaluated.

The local performance metrics resulted in improved global calculations where estimated compressor maps could be constructed to show the increased operating conditions required to meet design conditions. One such map was created, and it was observed the distortion performance was bounded between undistorted equivalent fan speed and equivalent mass flow conditions. To offset the distortion degradation to

performance, however, the target design speed would need to be less than 100%. The distortion profile investigated in this dissertation featured a maximum 90% recovery at the AIP and resulted in a 15% reduction in the engine operating range (global engine stall at 85% CFS).

Local performance calculations also show the range of performance metric variations. For example; performance increases were observed in the low total pressure and counter swirl regions but came at the cost of reduced efficiency. Large efficiency reductions around 30% occupied a substantial region of the profile distribution in areas of high counter-swirl.

Varying behavior between the core and bypass was observable through this data set, providing a comparison for highly loaded areas of the blade root to the less loaded areas of the blade mid-span and tip. It was shown that the blade loading affected the pressure rise sensitivity to inlet flow coefficient and inlet flow angle, an effect distinguished between the core and bypass regions. The core output flow also showed varying magnitude and distribution form the bypass, necessitating varying and possibly nonlinear stator design

Finally, *local performance calculations show the full annulus effect of localized distortions*. For example; blade loading due to distortion was found to be nearly consistently higher in all areas of the profile and not limited to the 'undistorted' region. Despite nearly half the distorted profile being of high recovery and considered 'undistorted', the blade loading was higher than the undistorted op point for the majority of the fan rotation, indicating the full annulus effect of localized distortions and the inability of the fan to recover from distortions as severe as the one investigated.

5.1.7 Secondary Flow Impact

The impact of a total pressure distortion of this magnitude on fan performance is severe. In a research effort where inlet duct architectures are designed to minimize fan efficiency losses to 1%, an 8% global fan efficiency loss for total pressure distortions indicates research efforts need to be redirected to the components most susceptible to performance degradation as a result of next generation aircraft architectures. While pressure rise can be shown to be higher across the fan in some areas, this is a deceptive performance improvement as efficiency reductions and increased blade loading are observed almost everywhere in the profile, a direct result from the secondary flow developed due to the total pressure distortion.

The counter-swirl developed in the distortion most heavily impacted the fan performance, contributing to increased diffusion that affected the entire profile, resulting in a global blade loading increase of 10%. High recovery regions of the profile that would have thought to have been undistorted showed increased diffusion, evidence of the full profile effect of localized distortions. Also, the fan responded unequally to the relatively equal inlet swirl angles magnitudes, creating a bias toward increased blade loading in the counter-swirl regions that was not offset by equal unloading in the co-swirl region which resulted in the global loading increases and efficiency decreases.

5.2 Conclusions

The primary points of note from the previous section are summarized below:

1) Full flowfield measurements allow for sufficient data to be collected to characterize the fan response to the distortion; allowing for A) accurate linear interpolation between data points in both the radial and circumferential directions, B) flow parameter distributions to be created upstream and downstream of the rotor, and C) fan blade geometry effects to be discerned.
2) Measuring the fan inlet profile is essential to ensure that performance and efficiency are calculated correctly and that local trends and relationships are accurately determined. Significant differences were calculated for fan performance in the absence of fan inlet measurements. The fan inlet measurement plane also provides detail on the distortion development and the substantial flow redistribution upstream of the fan that resulted in high tangential and radial flow components due to the total pressure distortion that created blade incidence swings of +/- 10°.
3) Fan outlet measurements showed the persistence of the pressure and secondary flow variations in the distortion profile. While the radial flow angle variation was mitigated through the fan, total pressure, static pressure, and tangential flow angles were exacerbated in magnitude
4) Secondary flow effects cannot be decoupled from total pressure distortion in traditional fan performance measurement configurations, and it is these primarily these secondary flow characteristics that drive the local fan response, not the total pressure.
5) The counter-swirl region of the distortion led to local efficiency reductions of 30%, blade loading increases of 60%, and diffusion factors exceeding 0.7.
6) Trends and distributions of the fan behavior in varying regions of the distortion were preserved between speeds, indicating that lower speed tests can be performed to study distortion interactions to reduce cost while preserving the phenomena of interest.
7) Local performance metrics resulted in improved global calculations, the range of performance metric variations, and the full annulus effect of localized distortions.

5.3 Recommendations

As part of NASA's Environmentally Responsible Aviation (ERA) project, NASA collaborated with General Electric on a project that improved compressor aerodynamic efficiency that could offer 2.5% savings in fuel burn [35] for uniform inlet flow. If such extensive research effort is being pursued to improve modern engine designs, it is the author's strongest recommendation that more research must be invested in the area of

distortion tolerant fan design, where this work showed global efficiency reductions can reach 8% for distorted inlet flows characteristic of next generation airframe architectures. This future engine operating environment create challenges that 2.5% efficiency increases will not offset, and future research needs to focus on the problems that cause the most performance loss.

The following sections highlight several other recommendations obtained from this work.

5.3.1 Distortion Screen Calibration

Recommended procedures for future investigators include the following:

- When possible, measure the fan inlet profile with equal measurement density as that performed for the fan outlet. Distortion profiles measured in wind tunnel configurations in the absence of fan effects will develop differently when placed upstream of the fan. The improved accuracy on performance calculations more than offset the difficulty and risk associated with the procedure.
- Use caution when attempting to perform isolated pressure and swirl distortion fan response tests. Total pressure distortions inherently produce their own secondary flow variations that can be of equal magnitude to the swirl distortion produced by the inlet that is being simulated.
- Include flow angularity measurements at the AIP to determine the severity of the secondary flow formation farther upstream of the fan face. This will indicate whether the mixing of pressure regions creates secondary flow further upstream than the fan face.

5.3.2 Fan Performance Ground Testing

- High speed or near design engine tests are not necessary for characterizing fan response to distorted inflows. This will reduce experiment costs, and lower speeds will allow for more intense distortions to be safely studied without fear of engine stall.
- Multiple speeds should be studied for evaluating the distortion over a large portion of the compressor map. Such information will be useful in estimating the fan performance at higher speeds and developing a model for the fan behavior with respect to the distortion.
- Testing on a full scale engine should be performed whenever possible, as isolated electric driven fan designs lack the coupled low pressure turbine operation that exists in full-scale engine experiments.

5.3.3 Distortion Tolerant Fan Design

- Although the part-span fan blade shroud on this engine did significantly alter the fan performance, the riblet-type feature near the tip of the blade showed far

less departure from expected performance. Thus, a riblet-type feature could be considered for future fan designs to provide aeromechanical support without suffering the significant losses in fan performance that part-span shrouds produce.

- Future research should include adjusting the stator vane outlet profile position based on the fan outlet flowfield for improved aerodynamic efficiency.
- Conduct research into developing a fan model that will assist in designing a distortion-tolerant fan. The extensive data set generated through this research can be used as experimental validation. The recommendations and conclusions obtained from this work should be implemented for the initial design.

5.4 Closing Statements

The goal of this work was to contribute to the body of research that has been pushing towards designing a distortion tolerant fan for next generation aircraft architectures. How that is accomplished has still yet to be determined. Shrouds, placed in at the mid-span in the engine investigated here, or at the top of the fan blades create a more stable blade that increases the stall margin, allowing for more complex distortions but at the cost of reduced performance, increasing fuel consumption over a flight envelope.

A more coupled solution between inlets and fans could result, where fans are individually designed for maximum performance for specific inlets. Inlet and exit guide vanes are tailor-designed as well to operate most efficiently for the distortion produced by the inlet at design conditions. This would be an expensive solution between airframe and engine designers, but would allow for the greatest performance and efficiency benefit.

The work presented here shows that the performance and stability margin reductions are substantial for the severity of distortion investigated and will require extensive redesigns on modern fans to power the aircrafts long-term effectively. The overall performance benefit may offset the reduction in fan performance, but the durability of the engines will be significantly affected and this must be taken into consideration.

The solution to performance and operability challenges inherent in blended wing body architectures will involve several aspects mentioned above, and new ones gathered from quality full scale experiments. The current state of the art is just beginning to understand the impact these distortions have on the performance of the engines and more research is required before a complete solution can be found. The work presented here highlights some of the inaccuracies of current experimental testing methodology. Utilizing the recommendations mentioned in the previous subsections, more accurate measurements can be made, leading to improved fan performance and flow development calculations and further characterize distortions and their impact on fan performance.

Bibliography

[1] Collier, F., Thomas, R., Burley, C., Nickol, C., Lee, C., and Tong, M., "Environmentally Responsible Aviation – Real Solutions for Environmental Challenges Facing Aviation," *27th International Congress of the Aeronautical Sciences*, No. ICAS 2010-1.6.1, ICAS, Nice, France, September 2010.

[2] Suder, K.L., "Overview of the NASA Environmentally Responsible Aviation Project's Propulsion Technology Portfolio," 48th AIAA/ASME/SAE/ASEE Joint Propulsion Conference & Exhibit, No. AIAA 2012-4038, AIAA, Atlanta, Georgia, August 2012.

[3] Plas, A.P., Sargeant, M. A., Madani, V., Crichton, D., Greitzer E. M., Hynes, T. P., and Hall, C. A. Performance of a boundary layer ingesting (bli) propulsion system. In 45th AIAA Aerospace Sciences Meeting & Exhibit, number AIAA-2007-450, Reno, Nevada, January 2007. AIAA.

[4] Ferrar, A., O'Brien, W.F., Progress in boundary layer ingesting embedded engine research. In 48th AIAA/ASME/SAE/ASEE Joint Propulsion Conference and Exhibit, number AIAA-2012-4283, Atlanta, GA, August 2012. AIAA.

[5] Anabtawi, A., Blackwelder, R., Liebeck, R., and Lissaman, P. Experimental investigation of boundary layer ingesting diffusers of a semi-circular cross section. In 36th Aerospace Sciences Meeting & Exhibit, number AIAA-98-16743, Reno, Nevada, January 1998. AIAA.

[6] Hamed, A. and Numbers, K. Inlet distortion considerations for high cycle fatigue in gas turbine engine. AIAA, (AIAA-1997-3364), 1997. University of Cincinnati.

[7] SAE Aerospace. Aerospace Information Report 1419. July 2011.

[8] Moore, F. K., and Greitzer, E. M. A theory of post-stall transients in axial compression systems: Part 1-development of equations. Transactions of the ASME, 108:68-76, January 1986.

[9] Moore, F. K., and Greitzer, E. M. A theory of post-stall transients in axial compression systems: Part 2-application. Transactions of the ASME, 108:231-239, January 1986.

[10] Hynes, T. P., and Greitzer, E. M. A method for assessing effects of circumferential flow distortion on compressor stability. Journal of Turbomachinery, 109:371-379, July 1987.

[11] Cousins, W.T. and Davis, M.W. Evaluating complex inlet distortion with a parallel compressor model: Part 1-concepts, theory, extensions, and limitations. In ASME Turbo Expo 2011, Vancouver, British Columbia, Canada, June 2011. GT2011- 45067.

[12] Cousins, W.T. and Davis, M.W. Evaluating complex inlet distortion with a parallel compressor model: Part 2-applications to complex patterns. In ASME Turbo Expo 2011, Vancouver, British Columbia, Canada, June 2011. GT2011-450.

[13] Lucas, J., O'Brien, W.F., and Ferrar, A. Effect of bli type inlet distortion on turbofan engine performance. In ASME Turbo Expo 2014: Turbine Technical Conference and Exposition, number GT2014-26666, Dusseldorf, Germany, June 2014. ASME.

[14] Fidalgo, V. J., Hall, C.A. and Colin, Y. A study of fan-distortion interaction within the nasa rotor 67 transonic stage. Journal of Turbomachinery, 134, September 2012.

[15] Gunn, E., Tooze, S., Hall, C., and Colin, Y., "An Experimental Study of Loss Sources in a Fan Operating with Continuous Inlet Stagnation Pressure Distortion," Vol. 135, Journal of Turbomachinery, Sept. 2013.

[16] Gunn, E., and Hall, C., "Aerodynamics of Boundary Layer Ingesting Fans," ASME Turbo Expo 2014: Turbine Technical Conference and Exposition, Dusseldorf, Germany, June 16-20 2014.

[17] Pearson, H. and McKenzie, A. B., "Wakes in Axial Compressors, Journal of the Royal Aeronautical Society, Vol. 63, No. 583,1959, p.415.

[18] Plourde, G.A. and Stenning, A.H., "The Attenuation of Circumferential Inlet Distortion in Multi-Stage Axial Compressors," Journal of Aircraft, Vol. 5, No. 3, May-June, 1968.

[19] Soeder, R.H. and Bobula, G.A., "Effect of Steady-State Pressure Distortion on Inlet Flow to a High-Bypass-Ratio Turbofan Engine,", NASA Technical Memo, Lewis Research Center, Cleveland, Ohio, October 1982.

[20] Ferrar, A. M., "Measurement and Uncertainty Analysis of Transonic Fan Response to Total Pressure Inlet Distortion," Ph.D. Dissertation, Mechanical Engineering Department, Virginia Polytechnic Institute and State University, 2015.

[21] ASME MFC Committee. Measurement of gas flow by bellmouth inlet flowmeters. August 2011. ASME MFC-26-2011.

[22] Carter, A. F. and Novak, R. A., "Computed Aspect Ratio-Curvature Effects Upon the Performance of a High-Pressure-Ratio Single-Stage Compressor," ASME Paper No. 65-WA/GTP- 12.

[23] Bailey, J. The influence of development and fan/screen interaction on screen-generated total pressure distortion profiles. Master's thesis, Virginia Polytechnic Institute and State University, Blacksburg, Virginia, 2014.

[24] SAE International, S-16 Committee. Gas turbine inlet flow distortion guidelines. January 2001. Aerospace Recommended Practice 1420.

[25] Frohnapfel, D.J. Experimental Investigation of Fan Rotor Response to Inlet Swirl Distortion. Master's thesis, Virginia Polytechnic Institute and State University, Blacksburg, Virginia, 2016.

[26] Wrong, C.B., "An Introduction to the JT15D Engine," ASME Paper No. 69-GT-119.

[27] Cook, D.L., "Development of the JT15D-1 Turbofan Engine," SAE Paper No. 720352, National Business Aircraft Meeting, Wichita, KS, March 15-17, 1972.

[28] Coleman, H. and Steele, G. Experimentation, Validation, and Uncertainty Analysis for Engineers. John Wiley and Sons, Inc., Hoboken, NJ, third edition, 2009.

[29] Hill, P. and Peterson, C. *Mechanics and Thermodynamics of Propulsion*. Addison Wesley, Reading, Massachusetts, second edition, 1992.

[30] Dixon, S.L. and Hall, C.A. *Fluid Mechanics and Thermodynamics of Turbomachinery*. Butterworth-Heinemann/Elsevier, UK, sixth edition, 2010.

[31] Figliola, R. and Beasley, D. *Theory and Design for Mechanical Measurements.* Wiley, Hoboken, New Jersey, fourth edition, 2006.

[32] Tomczak, M. Spatial interpolation and its uncertainty using automated anisotropic inverse distance weighting (idw) cross validation/jackknife approach. Journal of Geographic Information and Decision Analysis, 2(2):18-30, 1998.

[33] Berrier, B.L., Carter, M.B., Allan, B.G. "High Reynolds Number Investigation of a Flush-Mounted, S-Duct Inlet with Large Amounts of Boundary Layer Ingestion," NASA/TP-2005-213766. Langley Research Center, Hampton, Virginia

[34] Tillman, T.G. System study and distortion-tolerant fan design for a boundary layer ingesting propulsion system. NASA Contractor Report, (NASA NRA NNC07CB59C Phase 2 Final Report), July 2010. United Technologies Research Center.

[35] Heidmann, J. "Improving Engine Efficiency Through Core Developments," AIAA Aero Sciences Meeting Presentation, January 6, 2011.

[36] A. Treaster and M. Yocum. The calibration and application of five hole probes. Technical Memorandum, (TM 78-10), January 1978. The Pennsylvania State University, Institute for Science and Engineering, Applied Research Laboratory.

Appendix A Five-Hole Probe Calibration

The following sections detail a subset of the five-hole probe analysis, specifically the Mach number dependency study and the final interpolation maps.

A.1 Five-Hole Interpolation Maps

Final pressure coefficient maps for the five-hole probe are shown in Figure A.1. These maps were used to calculate the five-hole probe parameters discussed in Section 3.5. The map structure is well behaved and uniform through the bulk of the pitch and yaw angles calibrated. More variability is shown at the outer edges of the grid domain but as shown in the blue experimental data markers, the engine data was captured exclusively within ± 20° yaw and ± 15° pitch bounds.

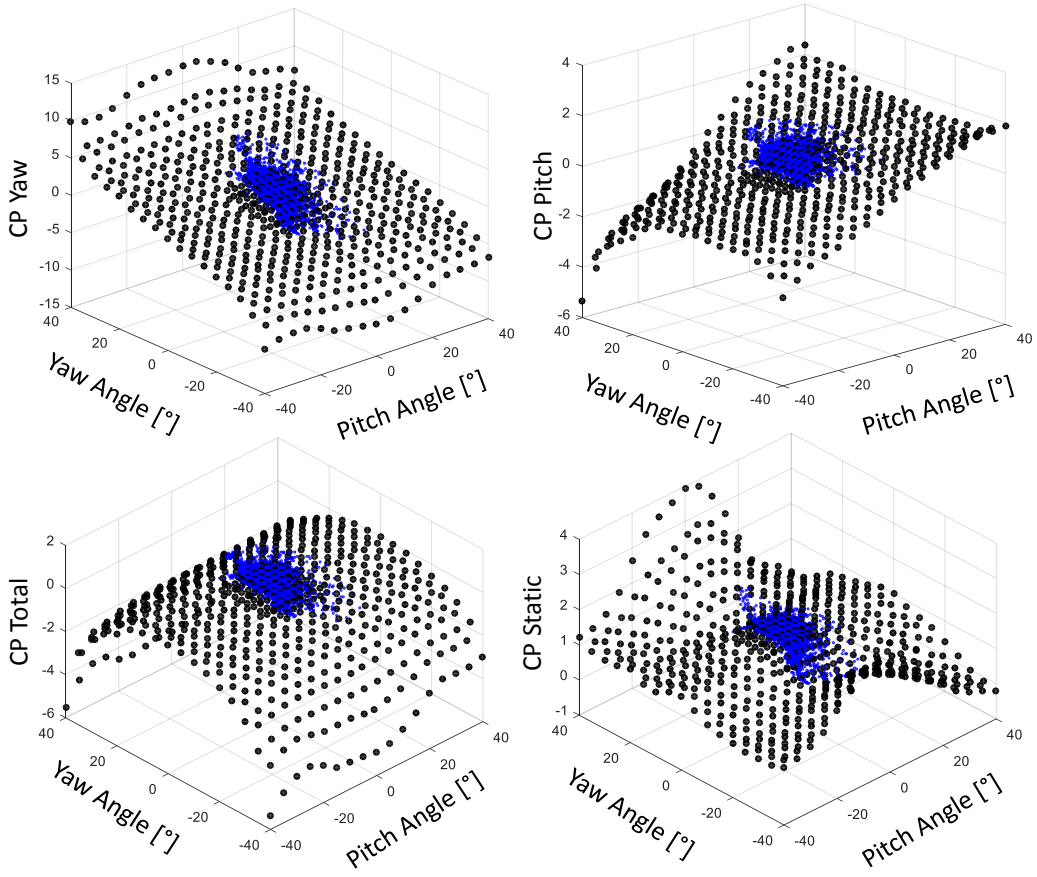

Figure A.1. Pressure coefficients for the five-hole probe calibration with experimental data (blue).

A.2 Mach Number Dependency

The five-hole probe calibration included several tests performed at multiple Mach numbers: 0.4, 0.5, and 0.6. The Mach number dependency was determined by comparing the difference between the numerical standard deviation from the experimental.

The numerical derivative was calculated for each five-hole pressure coefficient: total pressure, static pressure, yaw angle, and pitch angle. The pressure coefficient relationships are of the form given in Equation (A.1), where σ_{CP} represents the standard deviation from the mean and δ_{CP} represents variability in the final result due to error sources in the measurement.

$$\overline{CP} \pm \sigma_{CP} = F(P_1, P_2, \dots, P_5 \pm \delta_{CP}) \tag{A.1}$$

The numerical variation between for the five-hole probe parameters was estimated using a Taylor series expansion as shown in Equation (A.2), where σ_{P_i} is the measurement uncertainty of pressure port 'i', obtained during pre and post-test transducer calibrations.

$$\sigma_{CP}^2 = \sum_{i=i}^{5} \left(\frac{\partial Y}{\partial P_i}\right)^2 \sigma_{P_i}^2 \tag{A.2}$$

This procedure was performed for each pressure coefficient and compared to the standard deviation of the experimental data for all three speeds tested and is shown in Figure A.2.

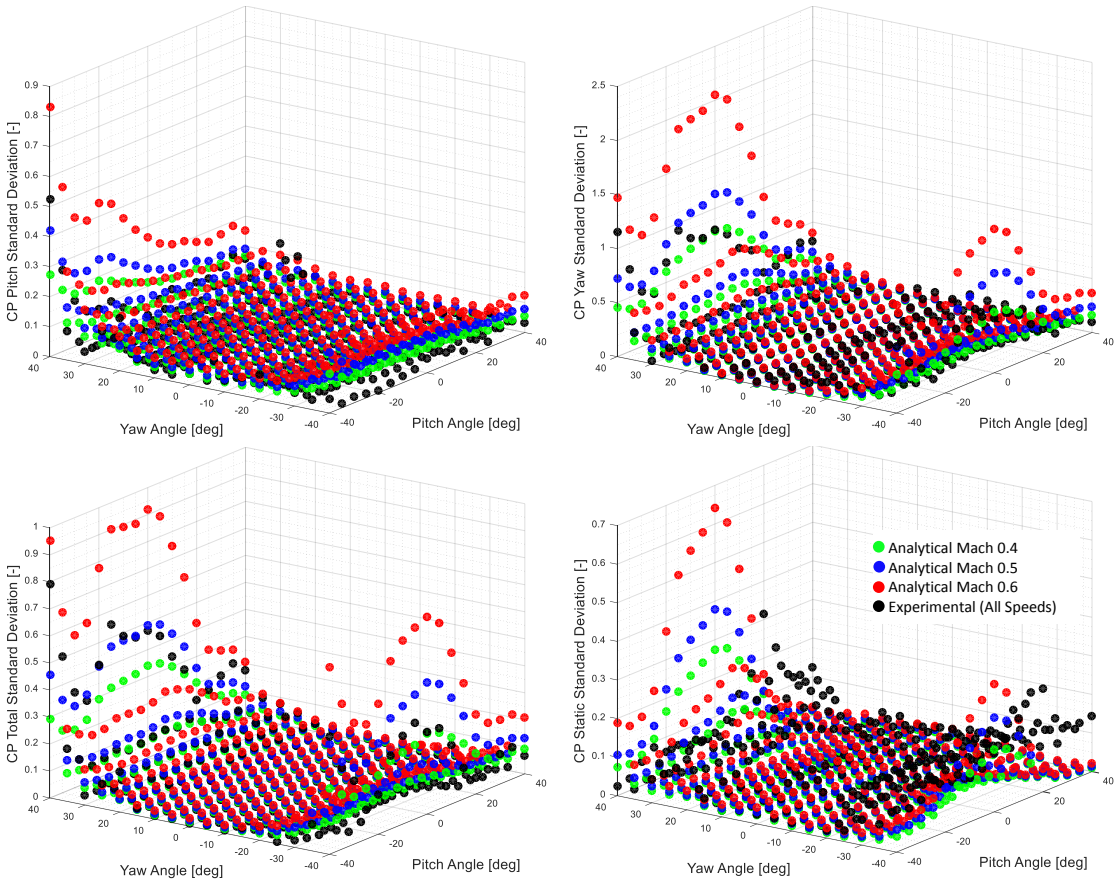

Figure A.2. Analytical and experimental pressure coefficient variability.

Table A.1 summarizes the RMS standard deviations for the numerical and experimental data sets. As shown, the experimental standard deviation between pressure coefficient measurements is comparable to the numerical results for the 0.5 and 0.6 Mach number cases, making them indistinguishable. The 0.4 Mach number case shows a higher variability due to the relatively higher uncertainty percentage of the nominal pressure values. Since the varying speeds could not be distinguished experimentally, it was concluded that the Mach number effects on the probe in the ranges expected were negligible and calibration maps were constructed using an average of all three speeds and functions of pitch and yaw angle only.

Table A.1. Numerical and experimental RMS measurement standard deviation.

	Numerical			Experimental - All Speeds
Mach Number	0.4	0.5	0.6	
CP Total	0.4	0.13	0.09	0.12
CP Static	0.11	0.07	0.05	0.09
CP Yaw	0.44	0.26	0.18	0.20
CP Pitch	0.12	0.08	0.05	0.05

Appendix B Uncertainty Propagation

The uncertainties associated with the calculated parameters detailed in Sections 3.5 and 3.6 were derived using the numerical sequential perturbation technique. This is summarized below and follows from Figliola and Beasley [31].

Beginning with a relationship among an independent variable, Y, and a finite number of dependent variables, X, that number from 1 to L, such that:

$$Y = F(X_1, X_2, \dots, X_L) \tag{B.1}$$

Perturb each independent variable in the positive manner by adding its corresponding uncertainty, u_i.

$$\begin{aligned} Y_1^+ &= F\left(X_1 + u_{X_1}, X_2, \dots, X_L\right), \\ Y_2^+ &= F\left(X_1, X_2 + u_{X_2}, \dots, X_L\right), \\ &\vdots \\ Y_L^+ &= F(X_1, X_2, \dots, X_L + u_L) \end{aligned} \tag{B.2}$$

Perturb each independent variable in the negative manner by subtracting its corresponding uncertainty, u_i.

$$\begin{aligned} Y_1^- &= F\left(X_1 - u_{X_1}, X_2, \dots, X_L\right), \\ Y_2^- &= F\left(X_1, X_2 - u_{X_2}, \dots, X_L\right), \\ &\vdots \\ Y_L^- &= F(X_1, X_2, \dots, X_L - u_L) \end{aligned} \tag{B.3}$$

Using a central difference scheme, the dependent variable perturbation with respect to each independent variable uncertainty can be calculated for i = 1, 2, …, L.

$$\frac{dY}{dX_i} = \frac{Y_i^+ - Y_i^-}{2u_{X_i}} \tag{B.4}$$

The overall uncertainty can then be calculated by performing a root sum square for all dependent perturbations.

$$U_Y = \sqrt{\sum_{i=1}^{L} \left(\frac{dY}{dX_i}\right)^2} \tag{B.5}$$

Appendix C Five-Hole Probe Analysis

C.1 Structural

A geometric parameterization was performed on the five-hole probe used throughout this research to maximize structural integrity while minimizing instrument intrusiveness. A brief description of the final probe dimensions are given in Section 2.2, a design result from the structural analysis performed. Figure C.1 details the design steps taken to achieve this, utilizing Ansys® CFX and Static Structural analyses.

Figure C.1-left shows the probe in the fan inlet measurement configuration where the maximum amount of probe surface area is exposed to the flow, representing the structurally weakest position of the probe during the experiment. The probe behaves like a cantilevered beam, with a cylindrical support at the compression fitting mounted to the top of the fan case. To obtain the radial pressure distribution, a 30° wedge CFD model was performed with the probe modeled as a fixed boundary, with the inlet flow corresponding to the highest CFS tested (80%), and the spinner was modeled as a rotating boundary. The model domain is shown in Figure C.1-center. The resulting pressure profile on the probe was then input into the static structural analysis using a cylindrical support at the top of the probe where the compression fitting would be located. A schematic of the analysis is shown in Figure C.1-right. Sensing head diameter and reinforcement tube diameter were selected based on this procedure. The tube wall thickness was a standard used for United Sensor™ for their pressure probes and was a fixed parameter in the analysis.

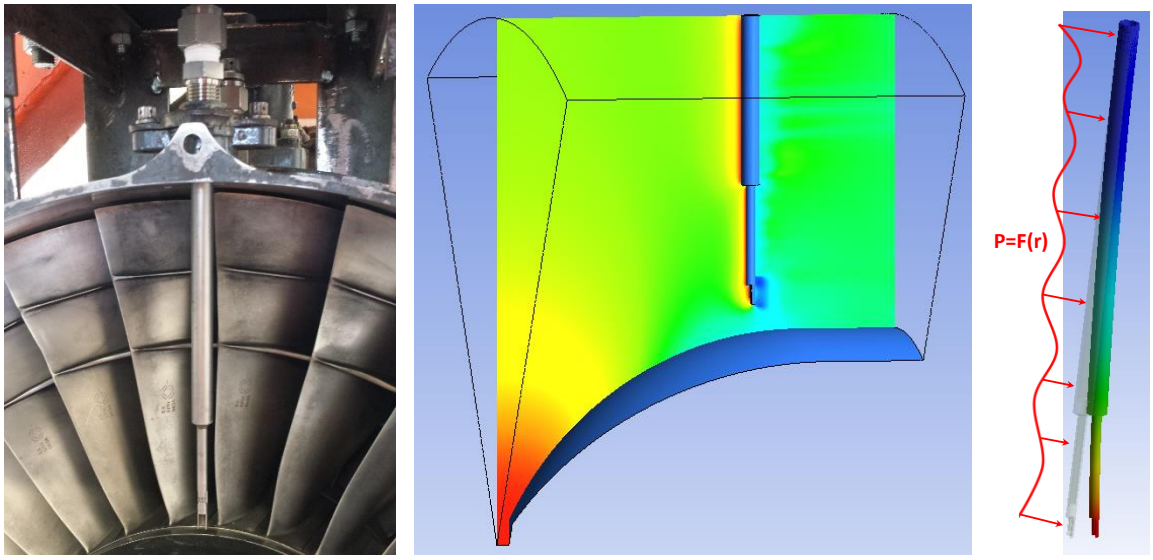

Figure C.1. Five-hole probe structural analysis: experimental setup (left), 30° section CFD model (center), and structural analysis deformation (right).

C.2 Modal

A modal analysis was performed on the probe geometry to indicate any blade passing frequencies that should be avoided during testing. The results are summarized in Figure C.2, with the modal analysis shown in the top-right for increasing insertion length. The blade passing frequencies (BPF) of interest are shown in the bottom-right, with only the 1st mode of the 6" insertion length of concern. Insertion lengths between 5 and 6 inches near 80% CFS were observed with caution with no vibratory probe effects found. The PTFE ferrule compression fitting at the fan case insertion helped dampen the vibratory effects of the flow over the probe.

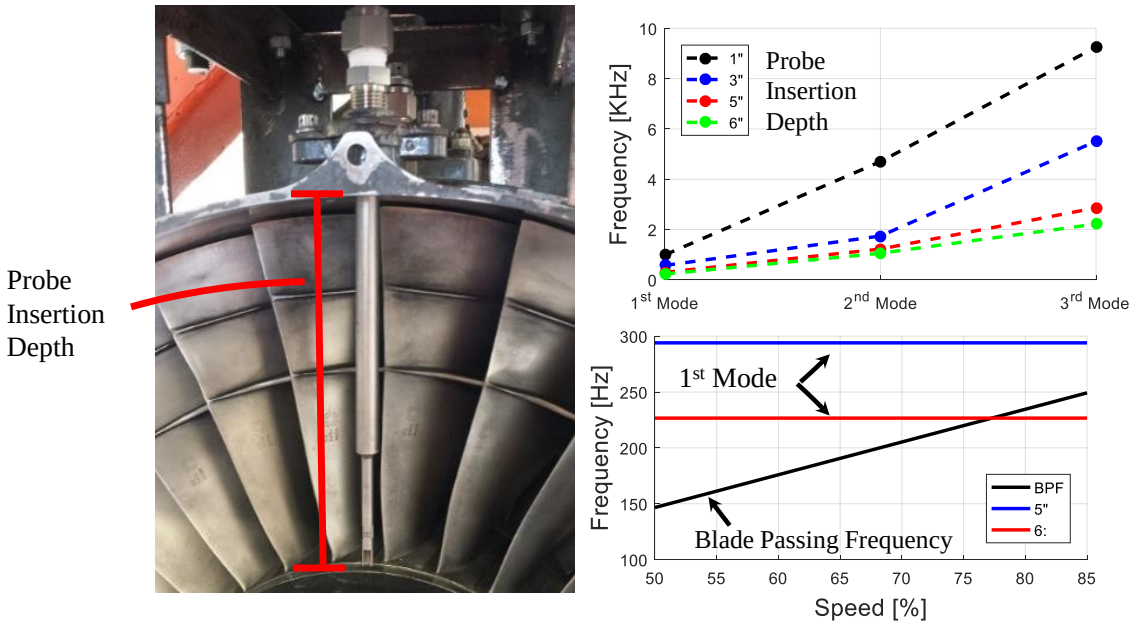

Figure C.2. Five-hole probe modal analysis.

C.3 Time Response

The time response of the five-hole probe pneumatic measurement system was estimated using a gated valve system in which a known pressure source was opened to the measurement system by electronic control of a gate valve. The pressure input was placed on the probe, followed by 25 feet of pneumatic tubing, and terminated in the transducer input port. Synchronizing the gate valve with the data acquisition, an estimation of the response time of the pressure probe system can be obtained.

The results of the test are shown in Figure C.3 with the time domain shown on the left and the frequency domain shown on the right. The standard score given on the ordinate of Figure C.3-left is calculated using Equation (C.1), where X is the recorded pressure data, μ is the population mean of X, and σ is the population standard deviation of X.

$$Z = \frac{X - \mu}{\sigma} \tag{C.1}$$

The results from Figure C.3 show that for a 0.25% error of the input pressure, the rise time is approximately 0.5 seconds with a settle time of approximately 0.8 seconds.

The frequency response, shown in Figure C.3-right, is obtained by performing a fast Fourier transform of the pressure data, X. This calculation as shown in Equation (C.2), where *n* is represents the sample length.

$$Y(k) = \sum_{j=1}^{n} X(j) W_n^{(j-1)(k-1)} \tag{C.2}$$

Where

$$W_n = e^{\frac{-2\pi i}{n}} \tag{C.3}$$

Figure C.3-right shows a peak amplitude of approximately 0.5 Hz, indicating a two second response time for the measurement system utilized. These pressure results can also be applied to the Station 1 and Station 3 data as it utilizes a similar measurement methodology.

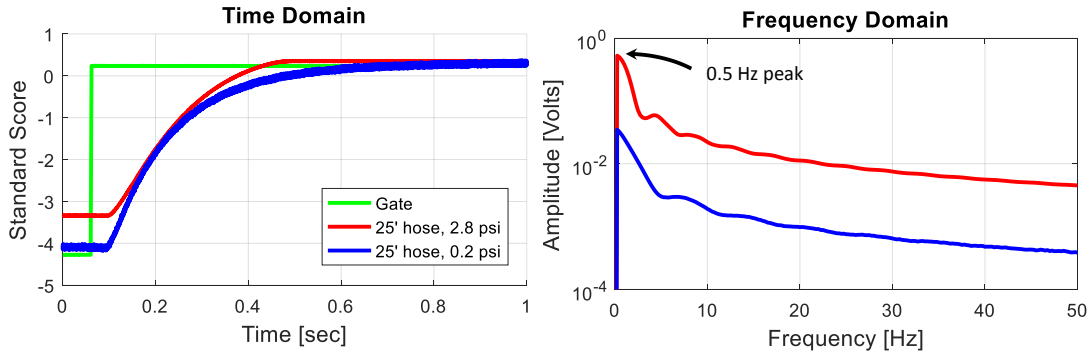

Figure C.3. Time (left) and frequency (right) of the pressure measurements from the five-hole probe.

Appendix D Fan Blade Modal Analysis

The blade modal analysis mentioned in Section 2.4.1.1 resulted from a modal analysis performed in Ansys® using the geometry obtained from a 3D scan. The blade was modeled as titanium, with compression supports at the pressure and suction sides of the part-span shroud, and a fixed support at the blade root. A similar analysis was run with frictionless supports at the pressure and suction sides of the part-span shrouds but the results were nearly indistinguishable to the compression only support. The compression only support boundary condition provided the most realistic setup to experimental conditions and was therefore used in the analysis. Figure 2.14 is reproduced below for convenience.

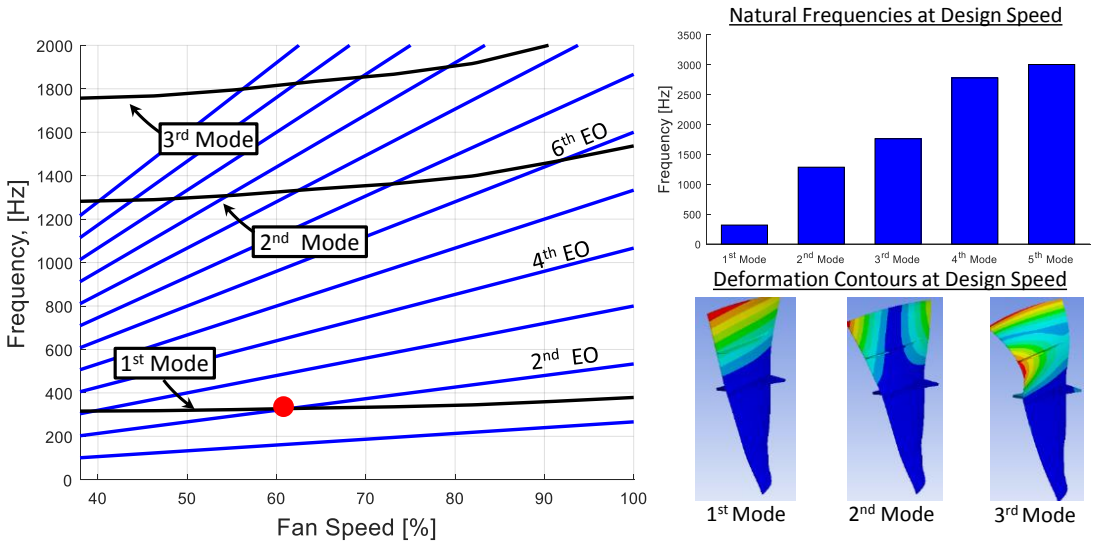

Figure D.1. Results of blade modal analysis.

Appendix E Fan Blade Geometry

The JT15D-1 fan blade geometry was reverse engineered by way of a 3D scan. This geometry was then imported into a CAD software package to fix coordinate locations. Figure E.1 details the process used to deconstruct the scan geometry. The scanned geometry was imported in Unigraphics® and a common data coordinate reference was created at the intersection of the three planes (Figure E.1-left), one that was normal to the fir-tree base front face, one that was bi-normal to the base front, and one that was tangent to the bottom of the base. Using the bottom tangent datum plane as a reference, datum planes were created span-wise along the blade, creating 2D curves at the intersections of the plane with the blade (Figure E.1-center). Finally, circles tangent to the pressure and suction sides of the intersections were created at the leading and trailing edges of the blade as shown in Figure E.1-right. A line was created through the center of these circles and extended beyond the end of the blade where its angle offset with respect to the axial flow direction could be measured (β).

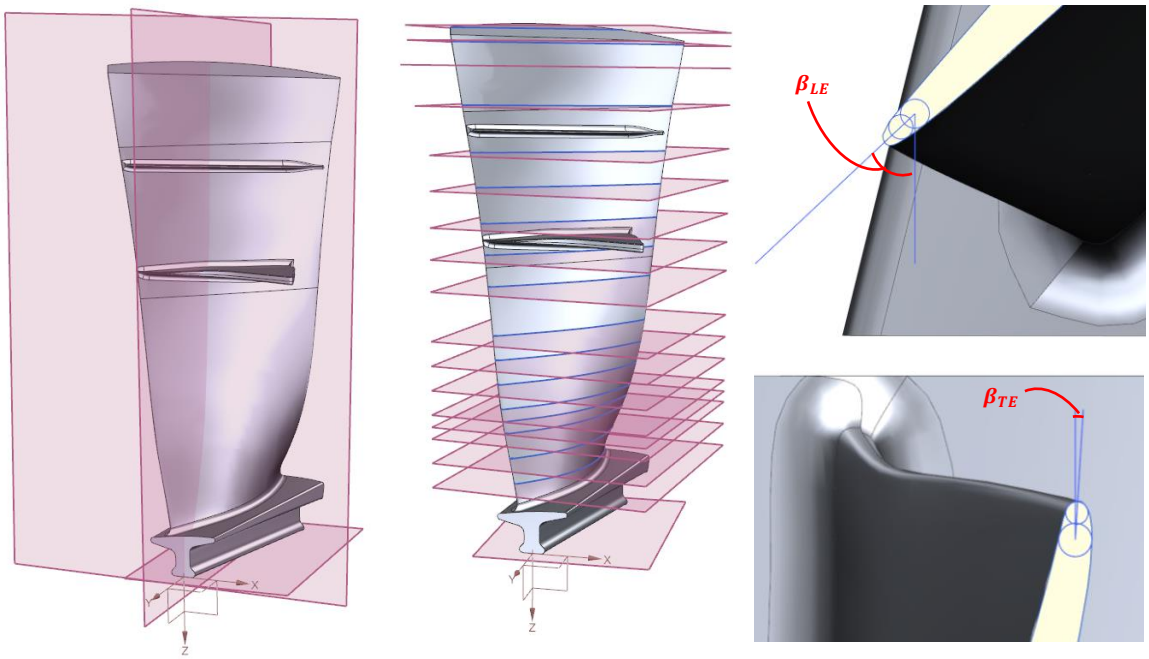

Figure E.1. Fan blade geometry deconstruction.

A summary of the blade geometry obtained from the process outlined above is given in Table E.1. The solidity was calculated by measuring the chord of the blade at each intersection and dividing by the base width. The data in Table E.1 was used throughout the dissertation.

Table E.1. JT15D-1 fan blade geometry.

Slice Number	Span-wise Distance from Engine Centerline to Slice [R/R_{tip}]	Leading Edge Blade Angle [°]	Trailing Edge Blade Angle [°]	Solidity
1	0.44	43.3	5.3	2.3
2	0.47	43.8	1.4	2.3
3	0.50	46.9	3.5	2.4
4	0.52	49.1	12.3	2.4
5	0.53	51.7	19.1	2.4
6	0.56	49.6	27.0	2.4
7	0.59	49.8	31.8	2.5
8	0.62	50.5	36.5	2.5
9	0.68	51.7	41.1	2.5
10	0.72	52.0	44.0	2.6
11	0.76	56.7	47.1	2.6
12	0.80	59.8	52.0	2.7
13	0.84	59.3	55.6	2.8
14	0.90	61.7	57.3	2.9
15	0.95	68.8	61.7	3.0
16	0.98	73.1	63.5	3.1
17	0.99	81.7	NA	NA

Appendix F Design Work Input

The undistorted blade loading distribution given in Figure 4.7-left was the result of the design requirements for near-constant work input on the flow. A constant work input creates a more uniform outlet flow that results in greater efficiency. The undistorted work distribution for the JT15D-1 is shown below in Figure F.1. The distribution shows some radial and geometrical variation but trends toward uniformity. Variations are shown to be exacerbated at higher fan speeds.

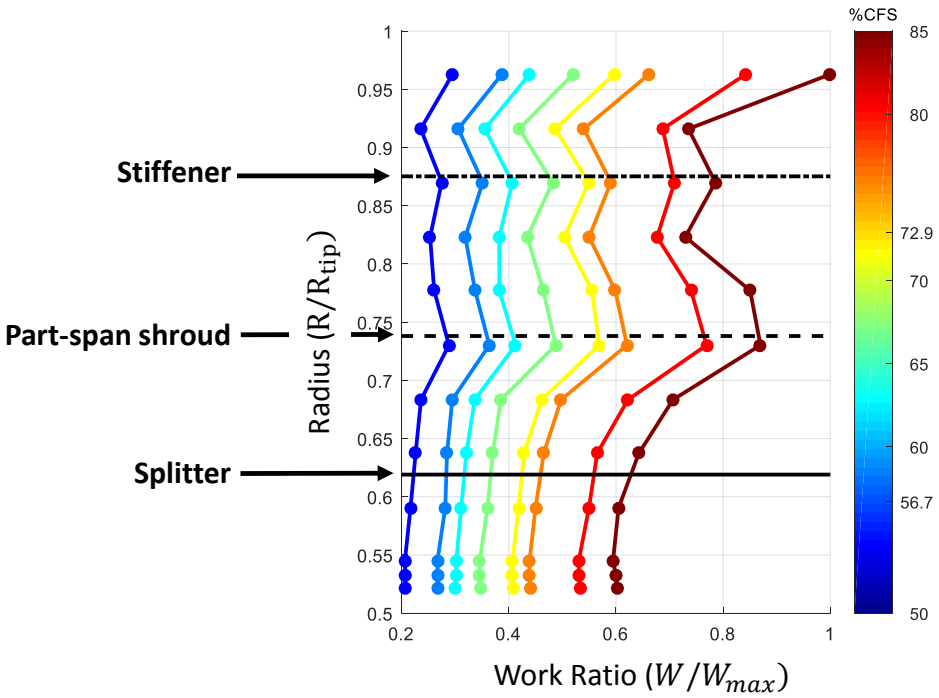

Figure F.1. Undistorted work input design distribution.

Appendix G Multiple Speed Data

Given below is a collection of the results presented in Section 4.3 for all of the speeds investigated. The results in Section 4.3 were for 70% CFS case for brevity and the remaining distortion conditions are given below for reference.

G.1 AIP

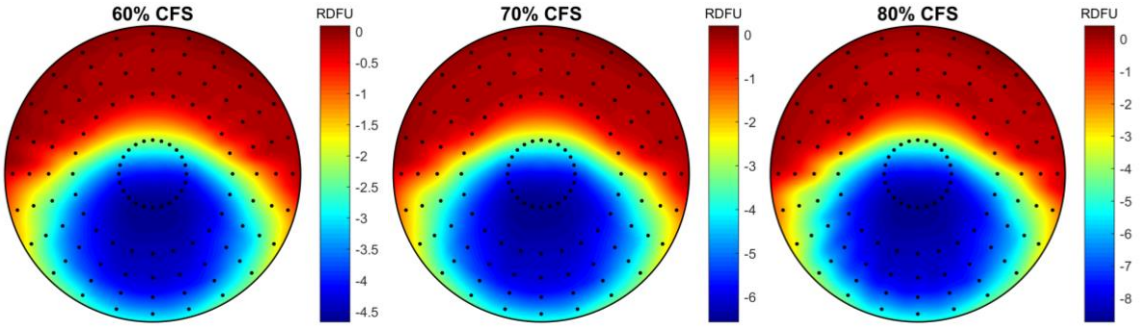

Figure G.1. Relative AIP Data from undistorted all speeds investigated.

G.2 Station 4

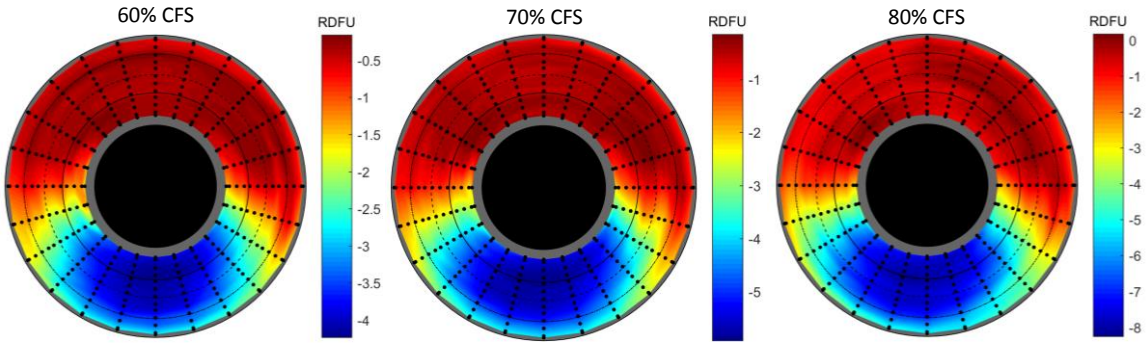

Figure G.2. Relative Station 4 total pressure from undistorted all fan speeds investigated.

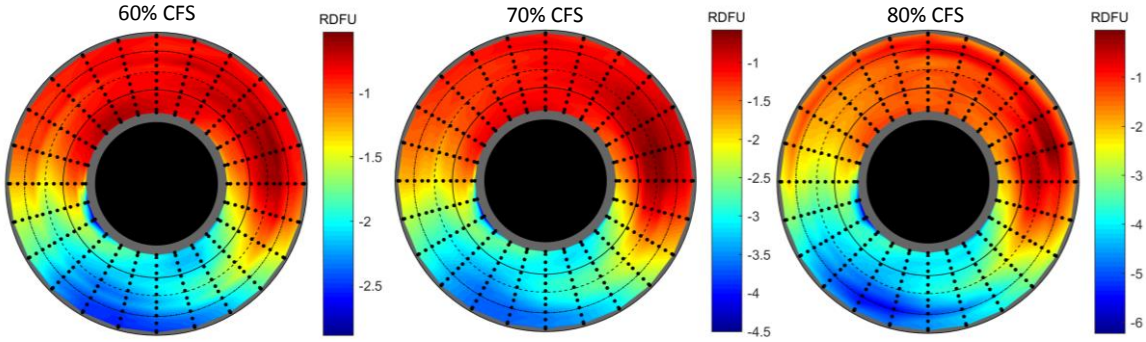

Figure G.3. Relative Station 4 static pressure from undistorted for all fan speeds investigated.

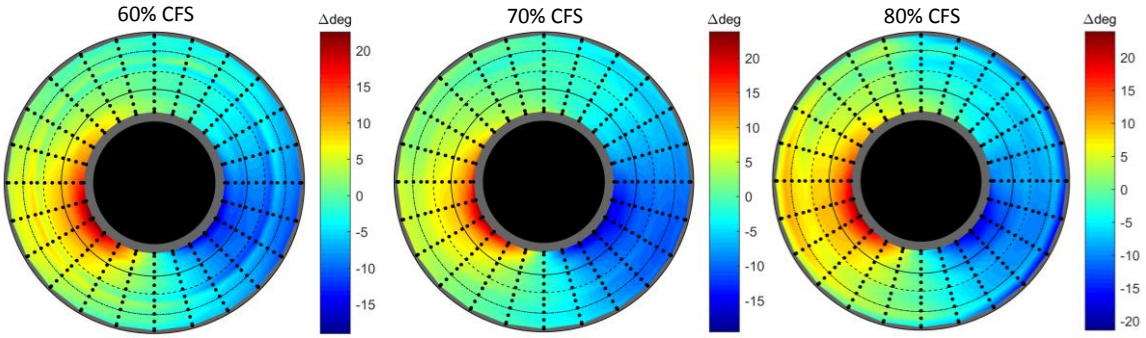

Figure G.4. Station 4 tangential flow angle difference from undistorted for all fan speeds investigated.

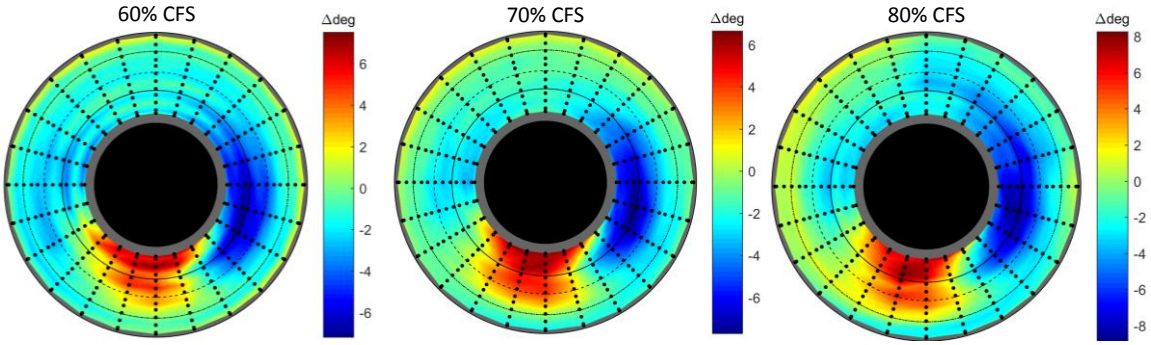

Figure G.5. Station 4 radial flow angle difference from undistorted for all fan speeds investigated.

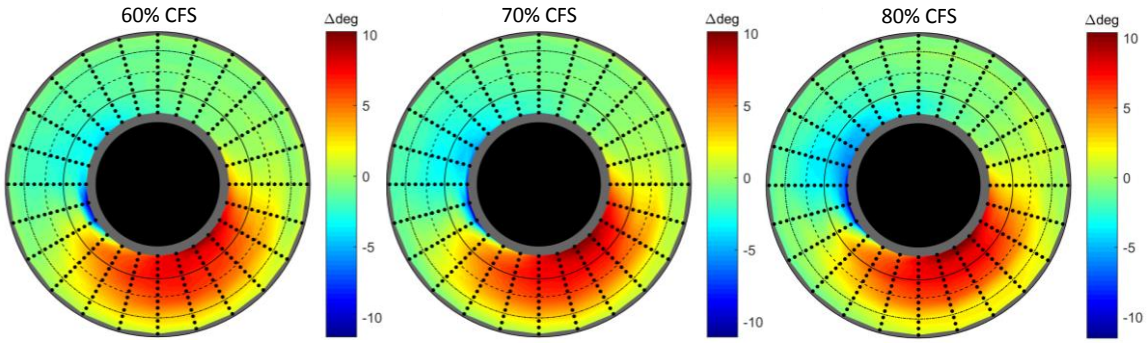

Figure G.6. Station 4 incidence angle difference from undistorted for all fan speeds investigated.

G.3 Station 5

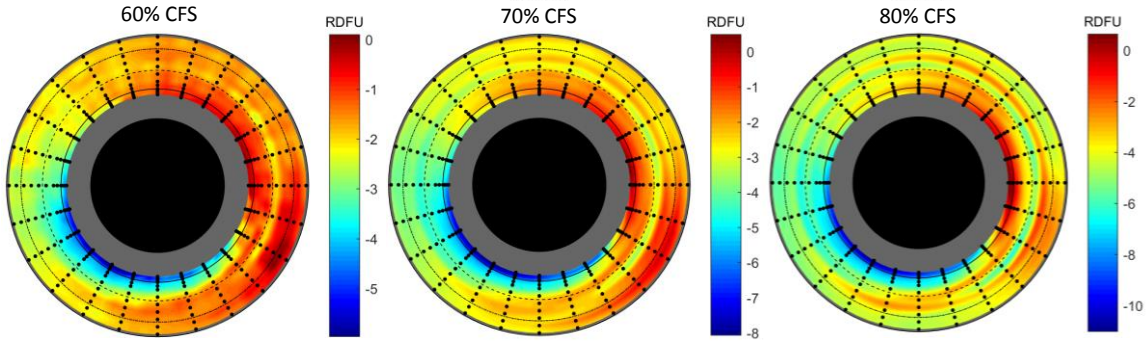

Figure G.7. Relative Station 5 total pressure from undistorted for all fan speeds investigated.

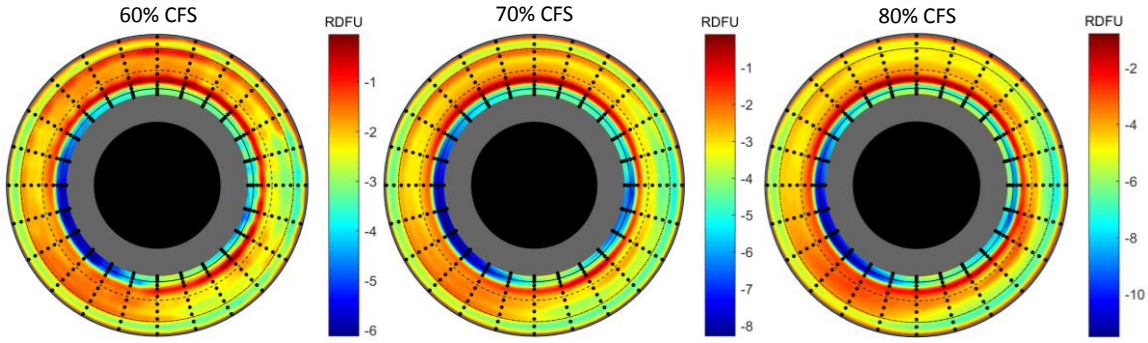

Figure G.8. Relative Station 5 static pressure from undistorted for all fan speeds investigated.

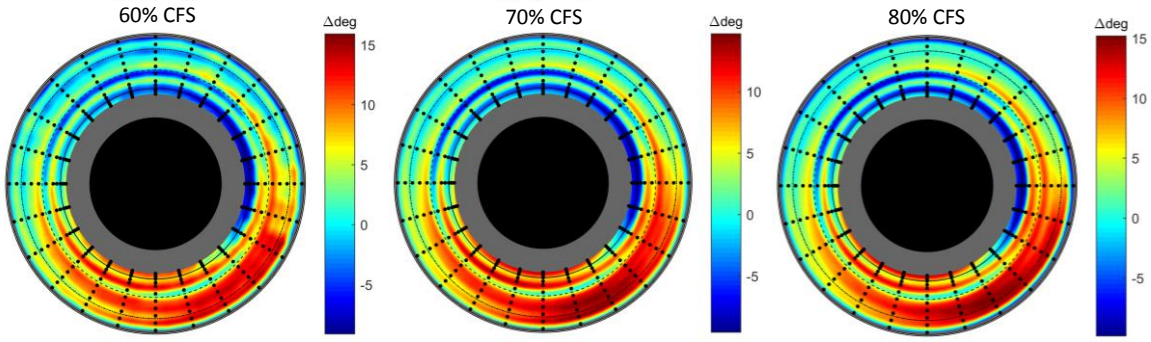

Figure G.9. Station 5 tangential flow angle difference from undistorted for all fan speeds investigated.

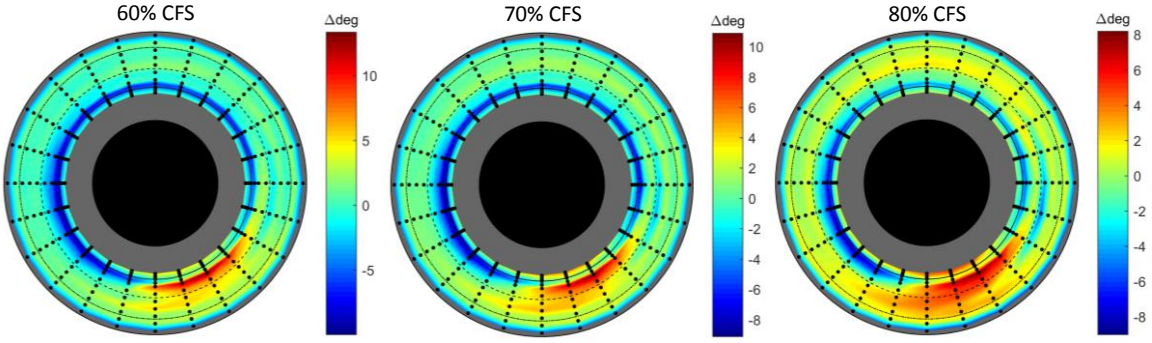

Figure G.10. Station 5 radial flow angle difference from undistorted for all fan speeds investigated.

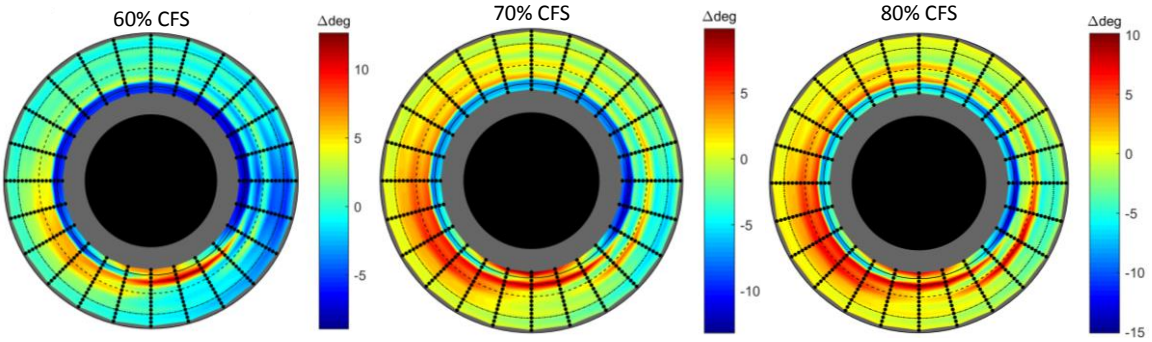

Figure G.11. Station 5 deviation angle difference from undistorted for all fan speeds investigated.

G.4 Fan Performance

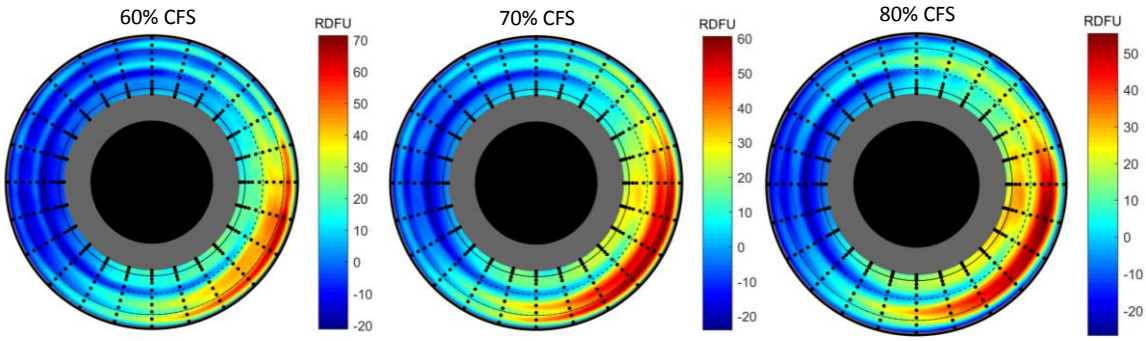

Figure G.12. Relative blade loading difference from undistorted for all fan speeds investigated.

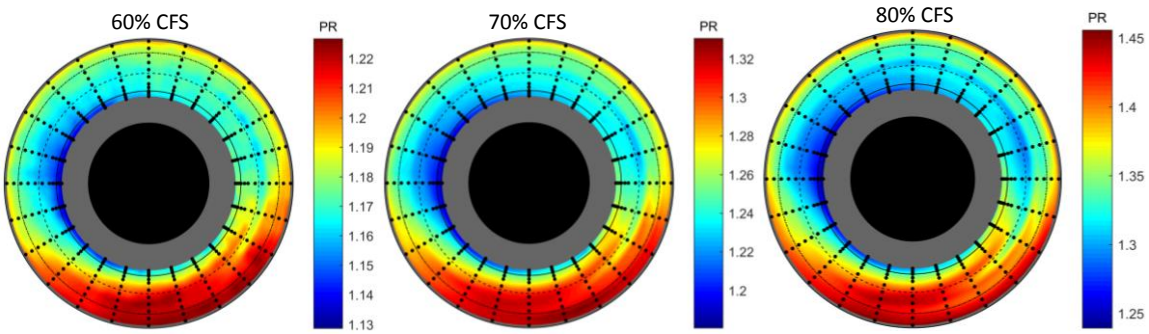

Figure G.13. Pressure rise for all fan speeds investigated.

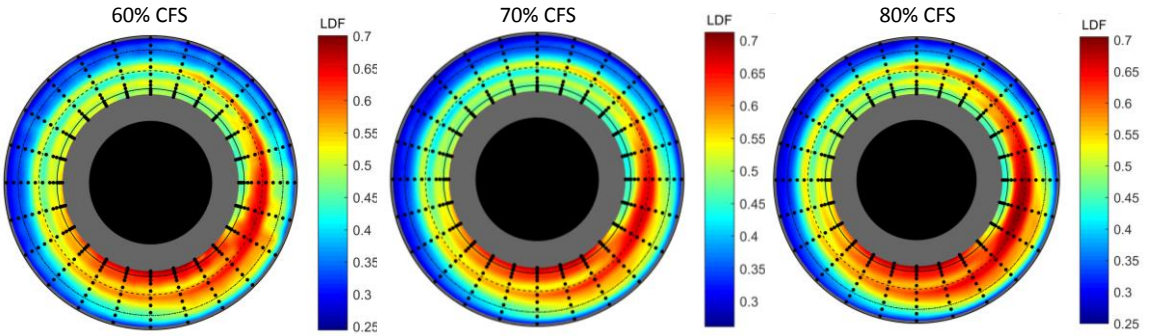

Figure G.14. Lieblein diffusion factor for all fan speeds investigated.

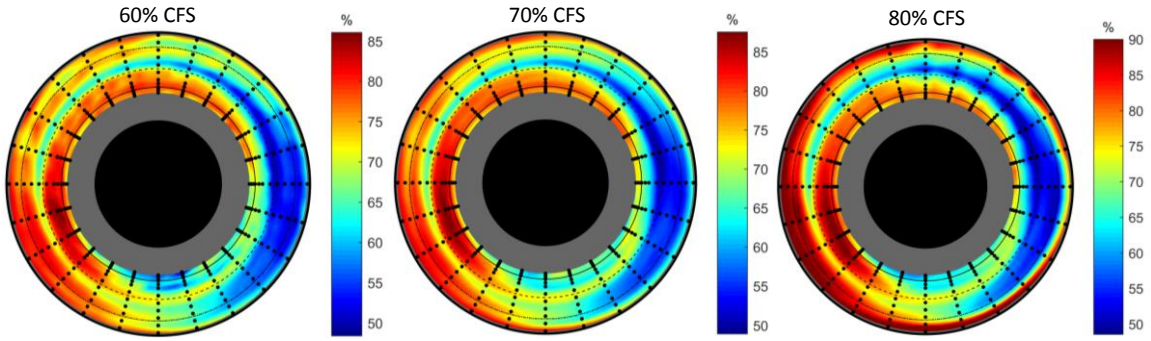

Figure G.15. Efficiency for all fan speeds investigated.